Title
Biomechanics of Optic Nerve Tethering in Adduction

Author
Park, Joseph

Publication Date
2022

Peer reviewed|Thesis/dissertation

UNIVERSITY OF CALIFORNIA

Los Angeles

Biomechanics of Optic Nerve Tethering in Adduction

A dissertation submitted in partial satisfaction

of the requirements for the degree Doctor of Philosophy in Bioengineering

by

Joseph Park

2022

ABSTRACT OF THE DISSERTATION

Biomechanics of Optic Nerve Tethering in Adduction

by

Joseph Park

Doctor of Philosophy in Bioengineering

University of California, Los Angeles, 2022

Professor Joseph L. Demer, Co-Chair

Professor Tzung Hsiai, Co-Chair

A novel hypothesis of optic nerve tethering, which represents a possible cause of primary open-angle glaucoma with normal intraocular pressure, has been motivated by magnetic resonance imaging studies performed in multiple eccentric gaze positions. To evaluate the hypothesis, this thesis reviews the basic anatomical structures of the eye, explores the biomechanical characteristics of ocular tissues, and observes and simulates the phenomenon of optic nerve tethering during adducting eye rotation. While there are many different secondary forms of

glaucoma, this thesis mainly considers a pressure-independent contribution to primary open-angle glaucoma.

Chapter 1 explains the current state of the glaucoma population, which is steadily increasing every year, and points out what may be a systematic narrowness in thinking in ophthalmology, which emphasizes intraocular pressure as the only known treatment of primary open-angle glaucoma.

In Chapter 2, the function, principle, and structure of the ocular globe and optic nerve are briefly reviewed, and the mechanical characteristics of the bilayered optic nerve sheath are explored in depth.

In Chapter 3, the mechanical properties of human ocular tissues, which are essential for understanding the biomechanical behavior of the ocular globe, are characterized through uniaxial micro-tensile testing. As an extended study, tensile experiments with and without preconditioning are performed on human ocular tissues to test the necessity for this preconditioning. In addition to the tensile testing, an opto-mechanical correlation between birefringence and tangent modulus of the ocular tissue is discussed as a possible non-invasive method of characterizing tissue.

Chapter 4 introduces the hypothesis of optic nerve tethering and summarizes observations from related previous imaging studies. The finite element analysis used in this paper predicts deformation of the optic nerve head and surrounding tissues due to traction by the optic nerve during adduction. After demonstrating the simulation of optic nerve tethering, the thesis explains the pathological connection between optic nerve tethering and normal tension glaucoma.

Lastly, chapter 5 concludes and suggests possible treatments for optic nerve tethering in adduction that might be applied if and when the hypothesis is confirmed in the future.

This dissertation of Joseph Park is approved.

Holden H. Wu

Vijay Gupta

Tzung Hsiai, Committee Co-Chair

Joseph L. Demer, Committee Co-Chair

University of California, Los Angeles

2022

THE DEDICATIONS:

To my parents, Park Jongman and Kim Shin-seon,
who have taught and guided me the right way with endless love.

To my parents-in-law, Lee Seung-mok and Oh Kyung-ran,
who always prayed and waited in faith.

To my beloved wife, Hanna Lee,
who is always with me in every journey through life.

To my soon-to-be-born son, Byulkom,
who will reflect the entirety of my life.

To those who donated their eyes,
whose loss will give birth to a brighter life.

And to Almighty God,
who has been here right from the beginning.

TABLE OF CONTENTS

LIST OF FIGURES

3.2.1. Opto-Mechanical Characterization of Sclera by Polarization Sensitive Optical Coherence Tomography

4.2.1. Scanning Laser Ophthalmoscopy Demonstrates Lower Peripapillary Strain in Older than Younger People During Adduction Tethering

4.3.1. Finite Element Analysis of Adduction Tethering of the Human Optic Nerve: Effects of Tissue Property Variation

LIST OF TABLES

2.3.2. Bilaminar Mechanics of the Human Optic Nerve Sheath

3.1.1. Material Properties and Effect of Preconditioning of Human Sclera, Optic Nerve, and Optic Nerve Sheath

3.2.1. Opto-Mechanical Characterization of Sclera by Polarization Sensitive Optical Coherence Tomography

ACKNOWLEDGEMENTS

Foremost, I would like to express my gratitude to my advisor, Joseph L. Demer, who has guided me throughout my 7 years of graduate studies. Dr. Demer has given me tremendous guidance for my research and writing. As a student entering the research field, I was able to learn from him how to formulate hypotheses, design and conduct experiments, analyze data, and interpret results. He not only provided the best guidance as an advisor but assisted me when I was having difficulties during my preliminary examination for graduate school. His patience and understanding allowed me to continue my studies. Without his support, I would have been frustrated at many major crossroads in my life.

Throughout my graduate school years, I would like to acknowledge current and past laboratory members who have supported me in many ways. Without these members, all our work would not have made it to fruition. I would like to express my tremendous appreciation to Andrew Shin and Soh Youn Suh. Andrew Shin, my very first laboratory mentor, helped me to adapt to the working environment and guided me on how to approach research. Soh Youn Suh, a senior researcher and clinician, also provided me with a plethora of medical knowledge and answered any of my questions. During my studies, there were some difficult times. Besides academics, I could always confide in Andrew and Soh Youn and they were always willing to lend their support. In addition, I would like to extend my appreciation to Nicolasa DeSalles, Somaye Jafari, Dave Burgess, Alan Le, Vadims Poukens, and Yolanda McNair for their assistance with my research, and say thank you to the new members of the Demer lab, Seongjin Lim, Dooseop Song, Immi Lee, and Andrew Tran, who gave me a memorable last year.

Lastly, I would like to express my everlasting gratitude to my beloved wife, Hanna Lee, who has always devoted herself to her husband that always returned home late from work. The lunch and dinner boxes you pack are always warm and delicious. Thank you and I love you, Hanna.

VITA

EDUCATION

2014	B.S., Mechanical & Aerospace Engineering Hanyang University, Seoul, South Korea
2016	M.S., Mechanical Engineering University of California - Los Angeles, Los Angeles, CA

RESEARCH EXPERIENCE

2012 – 2013	Senior Research in Welding & Printed Electronic Laboratory Hanyang University, Seoul, South Korea
2015 – 2022	Research Assistant in Ocular Motility Laboratory University of California - Los Angeles, Los Angeles, CA

HONOR & AWARDS

2016	Hot Topic, Association for Research in Vision and Ophthalmology (ARVO) Annual Meeting
2017 – 2021	T32: Ruth L. Kirschstein Institutional National Research Service Award, National Eye Institute
2017	Bioengineering Departmental Fellowship, UCLA Bioengineering
2017	Graduate Student Fellowship, UCLA Graduate Division
2018	Knights Templar Eye Foundation (US) Travel Grant, Association for Research in Vision and Ophthalmology (ARVO) Annual Meeting
2019	Graduate Student Fellowship, UCLA Graduate Division
2019	Excellence in Research Award, UCLA Department of Ophthalmology

PUBLICATIONS

1. Chang MY, Shin A, **Park J**, Nagiel A, Lalane RA, Schwartz SD, Demer JL. Deformation of optic nerve head and peripapillary tissues by horizontal duction. *Am J Ophthalmol* 2017;174:85-94.

2. Shin A, Yoo L, **Park J**, Demer JL. Finite element biomechanics of optic nerve sheath traction in adduction. *J Biomech Eng* 2017;139.

3. Suh SY, Le A, Shin A, **Park J**, Demer JL. Progressive deformation of the optic nerve head and peripapillary structures by graded horizontal duction. *Invest Ophthalmol Vis Sci* 2017;58:5015-21.

4. Shin A, **Park J**, Demer JL. Opto-mechanical characterization of sclera by polarization sensitive optical coherence tomography. *J Biomech* 2018;72:173-

5. Ugradar S, Karlin J, Le A, **Park J**, Goldberg RA. Photochemical collagen cross-linking reverses elastase-induced mechanical degradation of upper eyelid tarsus. *Ophthalmic Plast Reconstr Surg* 2020;36:562-5.

6. Le A, Shin A, **Park J**, Poukens V, Demer JL. Bilaminar structure of the human optic nerve sheath. *Curr Eye Res* 2020;45:864-72.

7. Shin A, **Park J**, Le A, Poukens V, Demer JL. Bilaminar mechanics of the human optic nerve sheath. *Curr Eye Res* 2020;45:854-63.

8. Jafari S, Lu Y, **Park J**, Demer JL. Finite element model of ocular adduction by active extraocular muscle contraction. *Invest Ophthalmol Vis Sci* 2021;62:1-.

9. **Park J**, Shin A, Jafari S, Demer JL. Material properties and effect of preconditioning of human sclera, optic nerve, and optic nerve sheath. *Biomech Model Mechanobiol* 2021;20:1-1.

PATENTS

1. Yeo SJ, Shim JH, **Park J**, Rhee S. (2014) Method or Evaluating Welding Quality of Spot Welding and Record Media Recorded Program Implement thereof. (S. Korea/Seoul, Patent No. 10-1445955). Korean Intellectual Property Office. www.kipo.go.kr

CHAPTER 1. INTRODUCTION

1.1. Current Status of Glaucoma

Millions of people worldwide suffer from an irreversible eye disease called glaucoma, and the number of patients is growing every year[1, 2]. Bright Focus Foundation (Clarksburg, MD) estimated the glaucoma population in 2020 worldwide as 80 million and predicted to increase by 2040 to 111 million[3]. The definition of glaucoma, the second leading cause of blindness, has been evolving over the decades, and even criteria for defining some specific forms of glaucoma have shifted. Optic disc, visual field, and intraocular pressure (IOP) are the popular criteria that have been used to define and diagnose glaucoma[4-10]. In particular, elevated IOP was considered the major defining feature of glaucoma in many past studies. However, recent studies report elevated IOP as a risk factor but not a defining characteristic of glaucoma[4-6]. The current defining feature of glaucoma is not limited to one statistically elevated IOP but changes in one or several anatomic and functional features[4-6].

1.2. Glaucoma Classification

Glaucoma is a progressive disease that is accompanied by structural damage to the optic nerve (ON) head and functional damage to the patient's vision[11]. This disease can be classified into more than 10 types depending on the cause, but primary open-angle and angle-closure glaucoma are two general categories. Primary open-angle glaucoma is the commonest, comprising

most North American glaucoma cases[3] in which the drainage angle formed by the cornea and iris remains open but the ON damage nevertheless develops. Angle-closure glaucoma, a secondary form that is the second most common type of glaucoma[12], occurs when the iris moves forward towards the cornea and thus narrows or blocks the drainage angle so it impedes the flow of aqueous humor and increases IOP acutely. Angle-closure glaucoma is clearly a type of glaucoma caused by high IOP, as are multiple other relatively uncommon secondary forms, but some patients with primary open-angle glaucoma experience ON damage even when the IOP is low or normal. (It is also the case that many patients with statistically elevated IOP do not develop ON damage.) In particular, in East Asian countries, there are far more patients with vision loss due to primary open-angle glaucoma with low than abnormally elevated IOP[13-19]. This type of primary open-angle glaucoma with normal or low IOP is commonly referred to as "normal tension glaucoma" (NTG).

1.3. Normal Tension Glaucoma

Normal tension glaucoma is currently diagnosed when there exist glaucomatous disc changes in the setting of constantly normal or low IOP (below 21 mmHg) measured on multiple occasions. Speculations have been made of multiple possible vascular causes such as chronic low ON perfusion, Raynaud's phenomenon with vasospasm, migraine, and nocturnal systemic hypotension[20-22], but the exact pathology of NTG has remained mysterious for several decades, and investigations into glaucoma pathogenesis is largely overshadowed by IOP-related studies. Lowering IOP remains the only available treatment for NTG[23-28]. As a primary solution for NTG, clinicians regularly prescribe eye drops such as prostaglandin analogs, beta-blockers, and alpha agonists to lower the normal to subnormal IOP even lower[23-28]. On the other hand, some recent

studies question the importance of IOP in NTG[29-32]. Mozaffarieh *et al.* have suggested non-IOP-dependent risk factors including ocular blood flow and oxidative stress[29]. Killer and Pircher have suggested that NTG might be the possible consequence of a toxic cerebrospinal fluid environment bathing the retrolaminar ON[30]. Demer *et al.* have suggested a novel biomechanical hypothesis based on ON tethering resulting in traction on the ON during adduction eye movement[31-33].

References

1. Quigley HA, Broman AT. The number of people with glaucoma worldwide in 2010 and 2020. *Br J Ophthalmol* 2006;90:262-7.
2. Tham YC, Li X, Wong TY, Quigley HA, Aung T, Cheng CY. Global prevalence of glaucoma and projections of glaucoma burden through 2040: A systematic review and meta-analysis. *Ophthalmology* 2014;121:2081-90.
3. Bright Focus Foundation G. Glaucoma: Facts& figures. https://www.brightfocus.org: Bright Focus Foundation; 2022.
4. Bathija R, Gupta N, Zangwill L, Weinreb RN. Changing definition of glaucoma. *J Glaucoma* 1998;7:165-9.
5. Liu SA, Zhao ZN, Sun NN, Han Y, Chen J, Fan ZG. Transitions of the understanding and definition of primary glaucoma. *Chin Med J (Engl)* 2018;131:2852-59.
6. Casson RJ, Chidlow G, Wood JP, Crowston JG, Goldberg I. Definition of glaucoma: Clinical and experimental concepts. *Clin Exp Ophthalmol* 2012;40:341-9.
7. Zangwill LM, Bowd C. Retinal nerve fiber layer analysis in the diagnosis of glaucoma. *Curr Opin Ophthalmol* 2006;17:120-31.
8. Chen TC. Spectral domain optical coherence tomography in glaucoma: Qualitative and quantitative analysis of the optic nerve head and retinal nerve fiber layer (an aos thesis). *Trans Am Ophthalmol Soc* 2009;107:254-81.
9. Raza AS, Cho J, de Moraes CG, et al. Retinal ganglion cell layer thickness and local visual field sensitivity in glaucoma. *Arch Ophthalmol* 2011;129:1529-36.

10. Scuderi G, Fragiotta S, Scuderi L, Iodice CM, Perdicchi A. Ganglion cell complex analysis in glaucoma patients: What can it tell us? *Eye Brain* 2020;12:33-44.
11. Foster PJ, Buhrmann R, Quigley HA, Johnson GJ. The definition and classification of glaucoma in prevalence surveys. *Br J Ophthalmol* 2002;86:238-42.
12. Ou Y. Primary angle-closure glaucoma: What to know. https://www.brightfocus.org: Bright Focus Foundation; 2022.
13. Cho HK, Kee C. Population-based glaucoma prevalence studies in asians. *Surv Ophthalmol* 2014;59:434-47.
14. Zhao J, Solano MM, Oldenburg CE, et al. Prevalence of normal-tension glaucoma in the chinese population: A systematic review and meta-analysis. *Am J Ophthalmol* 2019;199:101-10.
15. Kim JH, Kang SY, Kim NR, et al. Prevalence and characteristics of glaucoma among korean adults. *Korean J Ophthalmol* 2011;25:110-5.
16. Kim CS, Seong GJ, Lee NH, Song KC, Namil Study Group KGS. Prevalence of primary open-angle glaucoma in central south korea the namil study. *Ophthalmology* 2011;118:1024-30.
17. Iwase A, Suzuki Y, Araie M, et al. The prevalence of primary open-angle glaucoma in japanese: The tajimi study. *Ophthalmology* 2004;111:1641-8.
18. Iwase A, Araie M, Tomidokoro A, et al. Prevalence and causes of low vision and blindness in a japanese adult population: The tajimi study. *Ophthalmology* 2006;113:1354-62.
19. Yamada M, Hiratsuka Y, Roberts CB, et al. Prevalence of visual impairment in the adult japanese population by cause and severity and future projections. *Ophthalmic Epidemiol* 2010;17:50-7.
20. Mallick J, Devi L, Malik PK, Mallick J. Update on normal tension glaucoma. *J Ophthalmic Vis Res* 2016;11:204-8.
21. Collaborative Normal-Tension Glaucoma Study G. The effectiveness of intraocular pressure reduction in the treatment of normal-tension glaucoma. Collaborative normal-tension glaucoma study group. *Am J Ophthalmol* 1998;126:498-505.
22. Heijl A, Leske MC, Bengtsson B, et al. Reduction of intraocular pressure and glaucoma progression: Results from the early manifest glaucoma trial. *Arch Ophthalmol* 2002;120:1268-79.

23. Stein JD. Diagnosis and treatment of normal-tension glaucoma. In: Scott IUF, S. (ed). aao.org: American Academy of Ophthalmology; 2007.
24. Gross L. How to handle normal-tension glaucoma. Review of Ophthalmology: https://www.reviewofophthalmology.com/; 2021.
25. Anderson DR, Normal Tension Glaucoma S. Collaborative normal tension glaucoma study. *Curr Opin Ophthalmol* 2003;14:86-90.
26. Radhakrishnan S. Normal-tension glaucoma: Questions and answers. https://www.glaucoma.org/: Glaucoma Research Foundation; 2020.
27. Ikeda Y, Mori K, Tada K, Ueno M, Kinoshita S, Sotozono C. Comparison study of intraocular pressure reduction efficacy and safety between latanoprost and tafluprost in japanese with normal-tension glaucoma. *Clin Ophthalmol* 2016;10:1633-7.
28. Tamada Y, Taniguchi T, Murase H, Yamamoto T, Kitazawa Y. Intraocular pressure-lowering efficacy of latanoprost in patients with normal-tension glaucoma or primary open-angle glaucoma. *J Ocul Pharmacol Ther* 2001;17:19-25.
29. Mozaffarieh M, Flammer J. New insights in the pathogenesis and treatment of normal tension glaucoma. *Curr Opin Pharmacol* 2013;13:43-9.
30. Killer HE, Pircher A. Normal tension glaucoma: Review of current understanding and mechanisms of the pathogenesis. *Eye (Lond)* 2018;32:924-30.
31. Demer JL. Optic nerve sheath as a novel mechanical load on the globe in ocular duction. *Invest Ophthalmol Vis Sci* 2016;57:1826-38.
32. Demer JL, Clark RA, Suh SY, et al. Magnetic resonance imaging of optic nerve traction during adduction in primary open-angle glaucoma with normal intraocular pressure. *Invest Ophthalmol Vis Sci* 2017;58:4114-25.
33. Demer JL, Clark RA, Suh SY, et al. Optic nerve traction during adduction in open angle glaucoma with normal versus elevated intraocular pressure. *Curr Eye Res* 2020;45:199-210.

CHAPTER 2. THE EYE

2.1. Eye Globe

Of the five special sense organs including smell, hearing, touch, and taste, the eye is responsible for sight. The eye allows humans to perceive many features, including shape, color, depth, and movement using its delicate optical system. In a nutshell, this is how the optical system works: as light is refracted by the transparent cornea, the iris adjusts the size of the pupil aperture to control the amount of light incident on the retina. Next, the lens collects and further focuses light on the surface of the retina, which contains light-sensitive photoreceptor cells called cones and rods. The retinal layer of the eye converts light signals into electrical signals that are transmitted to the brain via the ON, and after further processing are interpreted as vision.

The globe can be anatomically divided into two segments. The anterior segment of the globe consists of the cornea, iris, aqueous humor, and lens, and the posterior segment includes the sclera, vitreous humor, retina, and choroid. The outer shell is continuous from the transparent cornea and extends posteriorly to the sclera. The sclera forms the rounded shape of the posterior eye and provides resistance to internal pressure and external forces[1]. It also features six extraocular muscle attachments to the eye that implement eye rotation. The IOP is maintained by the aqueous humor that fills the anterior and posterior chambers, and the vitreous humor that is a clear gel that fills the major posterior cavity of the globe. At the very back of the vitreous cavity is the ON head, anterior termination of the ON, where all nerve fibers from the retina converge into a bundle. The

nerve fibers, their ganglion cells, and the inner retina get oxygen from the retinal arterial circulation, while the photoreceptors of the outer retina receive oxygen and nutrients from the highly vascular choroid layer. The "optic disc" is synonymous with "ON head" because of its disc shape as examined using optical instruments from outside the eye.

2.2. Optic Nerve

The ON is a cranial nerve that transmits electrical impulses that encode features such as edges, brightness, color, motion, and contrast from the retina to the brain. The ON is composed of retinal ganglion cell axons, glial cells, connective tissues, and blood vessels. The nerve fibers of the ON are delicate and therefore susceptible to external forces, and have little or no regenerative capability. Damage to the ON may lead to partial or complete blindness. The ON originates at its optic disc where all ganglion cell axons exit the eye, and is on average about 1.5 mm in diameter. The ON continues through the eye socket[a] with its orbital fat. The ON exits the apex of the orbit posteriorly via the optic canal until it merges in the anatomical midline with the ON of the fellow eye at the optic chiasm in the skull base. The optic disc is located about 2.5 disc diameters[2] nasal to the visual axis, corresponding to approximately 17° of visual direction, so the ON creates asymmetric loading on the eye during horizontal eye rotation. During eye rotation, the anterior ON slides around orbital fat lobules like a rope, but its posterior end is completely constrained at the orbital apex where the ON exits the orbit via the bony optic canal[3]. The ON sheath is a thick, tough tissue that surrounds the entire ON to protect the vulnerable nerve fibers. The space between the

[a] By analogy with astronomy the ON is anatomically designated the "orbit" since it contains the moving ocular "globe".

ON and its sheath is called the subarachnoid space and is filled with cerebrospinal fluid (CSF) that is subject to a range of hydrostatic pressures[4]. This CSF is the same fluid that bathes the entire brain and spinal cord, so both for this reason, and because of the composition of the myelin insulating cells surrounding ON axons, the ON actually represents a specialized tract of the brain, unlike all other peripheral nerves. Connective tissues including arachnoid trabeculae, pillars, and septa support the shape of the subarachnoid space[5].

References

1. Kolb H. Gross anatomy of the eye. In: Kolb H, Fernandez E, Nelson R (eds), *Webvision: The organization of the retina and visual system.* Salt Lake City (UT); 1995.
2. Kolb H. Simple anatomy of the retina. In: Kolb H, Fernandez E, Nelson R (eds), *Webvision: The organization of the retina and visual system.* Salt Lake City (UT); 1995.
3. Demer JL, Clark RA, Suh SY, et al. Magnetic resonance imaging of optic nerve traction during adduction in primary open-angle glaucoma with normal intraocular pressure. *Invest Ophthalmol Vis Sci* 2017;58:4114-25.
4. Mukherjee N, El-Dairi, MA, Tariq Bhatti, M. Optic nerve sheath fenestration-indications and techniques. *US Ophthalmic Review* 2013;6:125-31.
5. Killer HE, Laeng HR, Flammer J, Groscurth P. Architecture of arachnoid trabeculae, pillars, and septa in the subarachnoid space of the human optic nerve: Anatomy and clinical considerations. *Br J Ophthalmol* 2003;87:777-81.

2.3. Optic Nerve Sheath

Compared to other ocular tissues, the ON sheath has been poorly studied. Most studies regard the ON sheath as an extension of the dura mater, which is correct to a point but fails to capture the unique anatomical and mechanical environment of the ON. The following study expands understanding of the ON sheath by clearly examining mechanical properties. This study was published in *Current Eye Research* along with the anatomical study of ON sheath conducted by Le as a paired study[1]. In the study, Le et al. showed two distinct layers of human ON sheath having significantly higher density on the inner sheath than outer using a microscope[1].

References

1. Le A, Shin A, Park J, Poukens V, Demer JL. Bilaminar structure of the human optic nerve sheath. *Curr Eye Res* 2020;45:864-72.

Publications included in this chapter:

2.3.1. Shin A, **Park J**, Le A, Poukens V, Demer JL. Bilaminar mechanics of the human optic nerve sheath. *Curr Eye Res* 2020;45:854-63.

Contributions to the study: Joseph Park contributed as the person who discovered and discussed the bilayer of the ON sheath while he prepared the specimen for the micro-tensile experiment of the human ocular tissue. He also dissected and prepared human eye specimens used for histological and characterization studies, and performed uniaxial tensile testing.

2.3.1. Bilaminar Mechanics of Human Optic Nerve Sheath

Andrew Shin [1, 2], **Joseph Park** [1, 3], Alan Le [1, 3], Vadims Poukens [1], and Joseph L. Demer [1 ,4 ,5, 6]

[1] Department of Ophthalmology, Jules Stein Eye Institute, Los Angeles, CA, USA.
[2] Wellman Center for Photomedicine, Harvard Medical School & Massachusetts General Hospital, Boston, MA, USA.
[3] Department of Bioengineering, University of California, Los Angeles, CA, USA.
[4] Biomedical Engineering Interdepartmental Program, University of California, Los Angeles, CA, USA.
[5] Neuroscience Interdepartmental Program, University of California, Los Angeles, CA, USA.
[6] Department of Neurology, University of California, Los Angeles, CA, USA.

Abstract

Purpose: The adult human optic nerve (ON) sheath has recently been recognized to be bilaminar, consisting of the inner layer (IL) and outer layer (OL). Since the ON and sheath exert tension on the globe in large angle adduction as these structures transmit reaction force of the medial rectus muscle to the globe, this study investigated the laminar biomechanics of the human ON sheath.

Methods: Biomechanical characterization was performed in ON sheath specimens from 12 pairs of fresh, post-mortem adult eyes. Some ON sheath specimens were tested completely, while others were separated into IL and OL. Uniaxial tensile loading under physiological temperature and humidity was used to characterize a linear approximation as Young's modulus, and hyperelastic non-linear behavior using the formulation of Ogden. Micro-indentation was performed by imposing small compressive deformations with small, hard spheres. Specimens of the same sheaths were paraffin embedded, sectioned at 10 micron thickness, and stained with van Gieson's stain for anatomical correlation.

Results: Mean (± standard error of the mean, SEM) tensile Young's modulus of the inner sheath at 19.8 ± 1.6 MPa significantly exceeded that for OL at 9.7 ± 1.2 MPa; the whole sheath showed intermediate modulus of 15.4 ± 1.1 MPa. Under compression, the inner sheath was stiffer (7.9 ± 0.5 vs 5.2 ± 0.5 kPa) and more viscous (150.8 ± 10.6 vs 75.6 ± 6 kPa s) than outer sheath. The inner sheath had denser elastin fibers than outer sheath, correlating with greater stiffness.

Conclusions: We conclude that maximum tensile stiffness occurs in the elastin-rich ON sheath IL that inserts near the lamina cribrosa where tension in the sheath exerted during adduction tethering may be concentrated adjacent to the ON head.

Introduction

Although previously neglected as a mechanical factor, it has recently been recognized that the optic nerve (ON) and its sheath contribute to mechanical loading on both extraocular muscles and the ocular globe.[1] We recently demonstrated by magnetic resonance imaging (MRI) that ON length is insufficient to avoid tethering the globe when, for normal subjects, adduction exceeds about 26°.[2] Further adduction approaching the much greater limit of the oculomotor range requires strains in the orbital tissues, including translation of the whole globe. This translation in adduction is mainly in the nasal direction in healthy people, but the globe retracts posteriorly in primary open-angle glaucoma.[3] While medial rectus (MR) muscle force acts across a broad tendon insertion[4], reaction force to it is concentrated on the smaller ON canal and peripapillary sclera. Optical coherence tomography (OCT) shows that deformations of the ON head and Bruch's membrane produced by adduction exceed many-fold those resulting from extreme intraocular pressure (IOP) elevation,[5] or IOP-related deformations recently proposed as pathological to retina.[6] Sibony *et al*. used OCT to show in patients with elevated intracranial pressure that adduction induces folds extending from the optic disc to the retinal macula.[7]

Eye movements occur as often as several times per second[8] during wakefulness,[9] but persist even during sleep.[10] Rapid eye movements called saccades that change gaze direction by 25-45° frequently occur when the head and body are both free to move naturally.[11] Typical gaze shifts that occur during everyday head movement include eye movements averaging about 30°.[12,13] This means that the optic disc and peripapillary retina and sclera experience relentless, transient mechanical loadings by the ON. It has even been proposed that many cases of primary open-angle glaucoma may represent repetitive stress injury to the optic disc induced by a tractional

force exerted as the ON and its sheath become tethered during large adduction movements.[3] Finite element modeling (FEM) based upon bovine tissue properties suggests that reaction force to MR contraction is concentrated in the temporal peripapillary region and lamina cribrosa, sites of early damage in glaucoma.[14] It is evident from such modeling that the mechanical consequences of adduction tethering depend to a large extent on the local mechanical properties of the ON, its enclosing dural sheath, and the posterior sclera. The term "ON sheath" is widely used in the clinical and surgical literature for this mobile connective tissue structure, where it is preferred to the anatomically synonymous term "optic nerve dura mater," probably because all other dura mater is tightly constrained by anchoring bone or intervertebral discs.[15]

While biomechanical characterization has been performed of the lamina cribrosa,[16,17] and sclera, especially peripapillary sclera,[18,19] the ON and its enclosing sheath have been comparatively neglected. Consequently, prominent FEMs have either omitted the sheath entirely,[20] or parameterized the human ON sheath as identical to the dura mater of brain.[21] The biomechanical properties of the ON sheath have recently been characterized in mammals such as cow[14] and pig.[22,23] Based on measured mechanical properties of ocular tissues, FEM has been performed to predict stress and strain distribution around ONH due to eye movement.[14,22] Although the foregoing studies have consistently suggested that the stress and strain are induced near the ONH by eye movement, the accuracy of such FEM simulations is questionable since mechanical properties of the non-human ON sheath were employed. Biomechanical measurement of the human ON sheath is clearly warranted to make accurate inferences about the role of eye movements in human ON sheath biomechanics. Moreover, it has recently been found that the adult human ON sheath consists of distinct inner layer (IL) and outer layer (OL), with the IL containing denser collagen and abundant elastin, and the OL containing

less of each of these important structural proteins.[24] The differing composition of the two ON sheath layers leads to the obvious supposition that they might have differing intrinsic mechanical properties. Therefore, the current study aimed to investigate the laminar mechanical properties of the human ON sheath by employing some standard biomechanical characterization methods compared with histological evaluation of connective tissue composition in the same specimens.

Methods

Twelve pairs of whole human globes with long attached ONs were obtained in conformity with legal requirements from eye banks within three days of natural death, having been donated for research purposes. Specimens of cadaveric tissue, which were anonymous as received by our laboratory, are not further subject to ethical oversight since they are not defined under United States of America federal law as "living human subjects." Attached ONs with enclosing sheaths were 10 to 20 mm long as supplied by the eye banks. The anterior 3 mm of the tissue closest to the globe-ON junction was discarded because of thickness variation in transition to sclera, so tested specimens were obtained posterior to that in the region of apparently uniform sheath dimensions. The average donor age was 66 ± 15 (standard deviation, SD) years, and gender was equally balanced. Due to variations in technique by eye bank tissue harvesters, lengths of ON specimens varied so that it was impossible to perform every experimental test on each specimen. In the laboratory, the whole ON sheath was dissected from the ON, and then where possible the sheath was carefully separated into IL and OL using fine forceps, as illustrated in Figure 1. When grossly distinct, only mild dissecting force was necessary to separate two layers because in suitable cases there was a weak boundary or spontaneous separation between the layers. Physical separation of

the IL from OL was generally easiest in the most elderly specimens. In younger specimens where the two layers were strongly adherent, laminar separation was impossible. An industrial OCT scanner (OCS1300SS, Thorlabs Inc., Newton, NJ) was used to measure the cross-sectional areas of specimens that averaged 0.67 ± 0.08, 0.49 ± 0.04, and 0.92 ± 0.14 mm^2, respectively, for IL, OL, and whole sheath specimens.

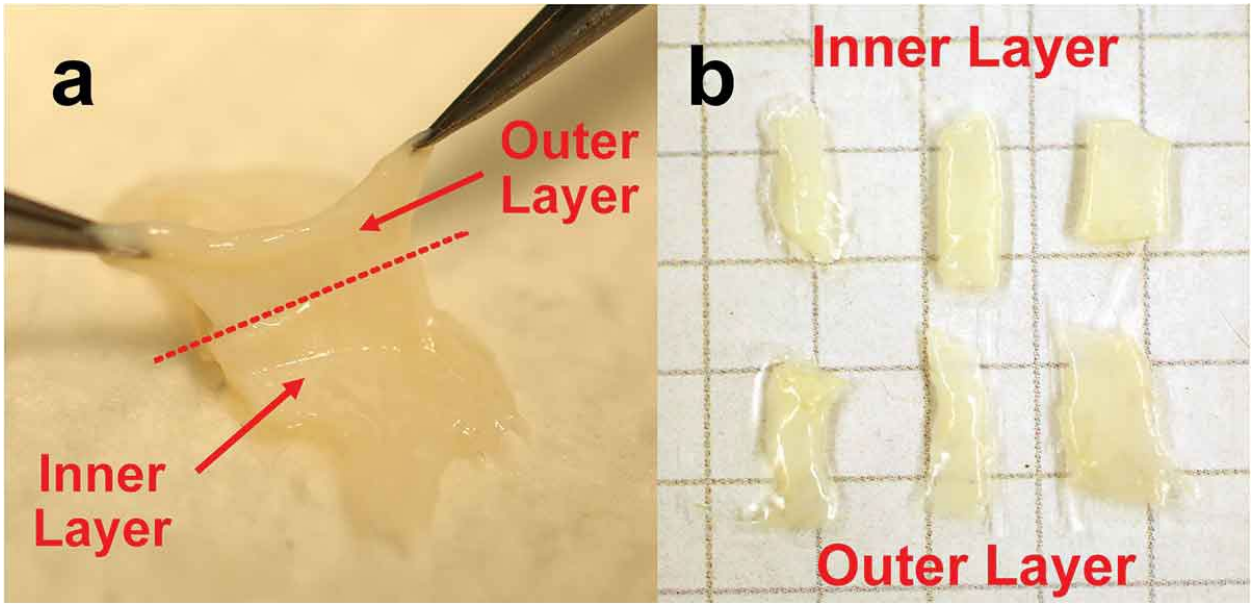

Figure 1. Laminar separation of optic nerve (ON) sheath for tensile testing. Prior to this photo, the cylindrical sheath was incised longitudinally to form a flat sheet. (a). ON sheath was separated into inner layer (IL) and outer layer (OL) via forceps distraction when the boundary between the two layers was weak. (b). Three pairs of IL and OL from whole ON sheath prepared for tensile experiments. 1 cm calibration grid.

Specimen dimensions were constrained by lengths of ONs obtainable by the eye banks even when harvesters were instructed to maximize specimen length. Each ON sheath was cut into 2 × 6 mm (width x length) rectangular shape for tensile testing including 1 mm clamping margin from each end; thus, aspect ratio was maintained at 2:1 to avoid experimental artifact due to aspect ratio variation.[25] Specimens were oriented in the longitudinal or circumferential directions for

testing in separate orientations. Cross-sectional dimensions of specimens were measured by OCT immediately after applying pre-loading for each tensile test. For micro-indentation, the whole sheath was trimmed to approximately 6–7 mm square shape for indentation at 4–5 widely-spaced locations.

A horizontal tensile loads cell was constructed, incorporating a linear motor (Ibex Engineering, Newbury Park, CA) having 100 mm/s maximum speed, a quadrature optical position encoder having 1 nm resolution, and a sensitive force sensor (LSB200, FUTEK, Irvine, CA) having 5 mN resolution. Via a frictionless air bearing, the linear motor shaft was coupled to an environmental chamber maintaining the tested specimens in approximately physiological temperature and humidity. Details of the load cell are published elsewhere.[26] Specimens were glued using cyanoacrylate between 5 mm long layers of thin cardboard that was anchored in serrated clamps to prevent slip. Pre-loading of 0.05 N, which is just above the noise level of force measurements, was applied by fine incremental elongation to avoid slackness, after which a constant elongation rate (0.01 mm/s) was imposed until failure as tensile force was recorded to characterize stress-strain behavior. Preliminary experiments were conducted with specimens preconditioned by cyclic loading up to 5% strain, but since tensile data obtained after this preconditioning did not differ significantly from data without preconditioning[14], preconditioning was thereafter omitted as unnecessary. Specimens were loaded to failure, although of course with failure often at nonphysiologic strains. Full data sets with loading to failure are nevertheless presented with this understanding. In order to examine the possible anisotropic mechanical behavior, tensile loading in orthogonal longitudinal and circumferential loading directions was performed in separate specimens. Three different types of specimens were tested as available from

each donated eye: 1) IL only; 2) OL only; 3) the whole ON sheath consisting of both layers. Numbers of each type of specimen are reported in Results Section 3.

While it is recognized that the relationship between stress and strain in most biological materials is non-linear, much of the existing literature and many published simulations of ocular biomechanics have approximated tensile properties using Young's modulus (YM), a linear relationship between stress and strain. For convenient comparison with the literature, we identified in every tensile stress-strain curve for each of the three ON sheath specimen types a linear region midway between the low strain "toe" and the failure region whose slope was considered to be YM. The reporting of YM values below should not be interpreted as a claim for linear behavior of the ON sheath, nor as a contradiction to our additional reporting of better-fitting non-linear material laws. In addition to the computation of YM, we also performed non-linear fitting to the Ogden hyperelastic model that gives excellent agreement with experimental data for brain and fat tissues[27], and that fit the current data better than alternative hyperelastic models. The hyperelastic model of Ogden[28] (N = 3) was employed having the strain energy potential form:

$$W = \sum_{i=1}^{N} \frac{2\mu_i}{\alpha_i{}^2}\left(\bar{\lambda}_1^{\alpha_i} + \bar{\lambda}_2^{\alpha_i} + \bar{\lambda}_3^{\alpha_i} - 3\right) + \sum_{i=1}^{N} \frac{1}{D_i}(J^{el} - 1)^{2i} \qquad (1)$$

where $\bar{\lambda}_j (j = 1, 2, 3)$ are the deviatoric principal stretches, J^{el} is the elastic volume ratio, μ_i (MPa) and α_i are material constants, and N is the number of terms in the material parameter descriptions of each layer determined by curve fitting to the tensile data under the assumption of near-incompressibility. D_i determines specimen compressibility.

Micro-indentation is a method of locally indenting the surface of a material with a probe of known shape to a depth that is small in relation to overall specimen thickness. Provided that the specimen is relatively thick in comparison to the indentation depth, the result of micro-indentation

is independent of total specimen thickness, and of whatever material may lie on the material's opposite side. Thus, for example, with a sufficiently small indenter, the IL or OL of the ON sheath could be tested by indentation of each respective surface without separating the two layers. A displacement-controlled indentation load cell (Figure 2a) was constructed by synchronizing a linear stepper motor (LNR50 Series, Thorlabs, Newton, NJ) and analytical balance (ML54, Mettler-Toledo, Columbus, OH).[29] Specimens were immersed in Ringer's lactate solution in a Petri dish placed on the pan of the analytical balance. The apparatus is sufficiently sensitive to detect the changing weight due to the evaporation of water from the Petri dish. In order to minimize changes in load, the load cell was surrounded by a glass chamber closed on all sides except for a small slit through which passed the indenter shaft. Downward indentation was created by a linear motor displacement having 100 nm precision, as force measurement was performed by analytical balance with 100 μg-force resolution, so loading could be recorded in a time series. The position of the balance pan was maintained by a servo within the balance, so that the indenter position was equal to indenter depth. A 1 mm in diameter stainless steel sphere was used to indent samples to 50 μm depth. Because indentation depth was small relative to layer thickness, this method thus permitted local measurement of the properties of only the layer in direct with the indenter. In most cases, the whole ON sheath specimen was simply placed in a Petri dish on the balance pan with the OL upward facing the indenter probe sphere to test the OL, or the specimen was inverted to test the IL. It was not possible to interpret micro-indentation of the whole ON sheath, because the technique only evaluates the one surface layer contacting the indenter.

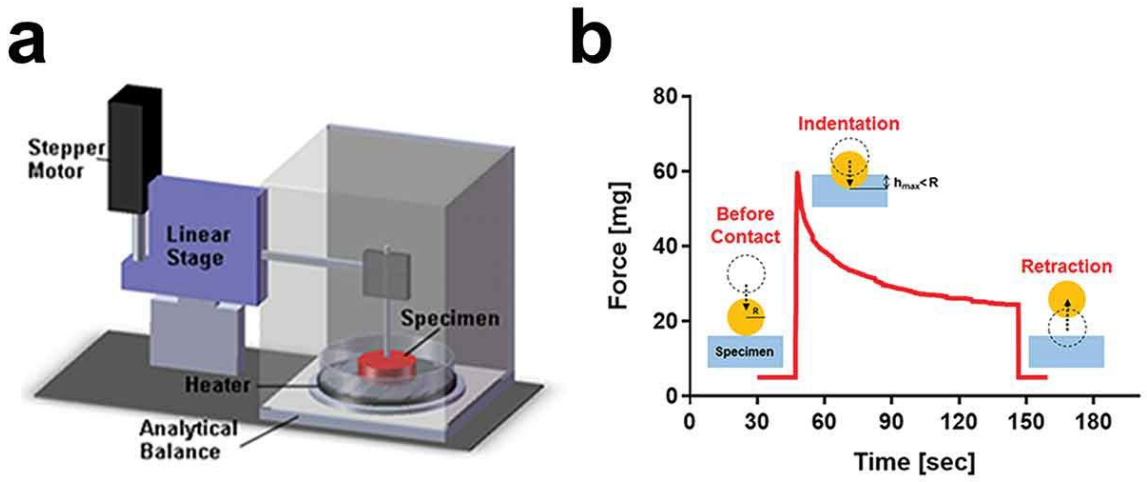

Figure 2. Micro-indentation compressive load cell. (a) 100 nm precision stepper motor was synchronized with a digital analytical balance whose pan was maintained in constant position by electromechanical feedback. (b). Typical relaxation data by micro-indentation. After the spherical tip contacts the specimen surface, force rapidly increases due to the indentation that is smaller than the indenter radius. Force relaxation occurs during maintained deformation, after which then the indenter was lifted from the specimen.

For each indentation, the surface tension of the liquid layer on the specimen transiently created tractional (negative) force upon initial probe contact. Further incremental indentation was then applied to generate about 100 ~ 200 μg compressive (positive) force, indicating onset of contact with the specimen itself. Following contact, the probe was accelerated at 0.5 mm/s^2 to a speed of 1 mm/s until 50 μm indentation was achieved, after which the indenter was maintained in that fixed position as the specimen relaxed for approximately 80 seconds during applied force measurement. Figure 2b illustrates the stress relaxation testing procedure.

The Hertzian linear viscoelastic model was chosen for micro-indentation data analysis since a spherical-tip micro-indenter was used, a previous study successfully characterized bovine ocular tissues using this model[29], and insufficient data could be collected to characterize a nonlinear model in these tissues. The full derivation of the model is included in the Appendix.

We show in a companion paper that the ON sheath contains collagen and abundant embedded elastin fibers.[24] A general rule of mixture provides a reasonable estimate of the YM of a composite material composed of parallel fibers of uniform direction embedded in a matrix.[30] There are two extreme cases: the upper-bound modulus corresponding to loading parallel to the fibers, and lower-bound corresponding to loading transverse to the embedded fibers. The rule of mixture was applied to the two layers of the ON sheath as follows:

$$E_{w,upper} = fE_i + (1-f)E_o \qquad (2)$$

$$E_{w,lower} = \left(\frac{f}{E_i} + \frac{1-f}{E_o}\right)^{-1} \qquad (3)$$

where E_i, E_o, and E_w are YM's for IL, OL, and whole ON sheath, respectively, and f is the volume fraction of the IL in proportion to the whole ON sheath. The rule of mixtures was used to make an inference about isotropy based upon the comparison of whole ON sheath YM, and corresponding individual values for the IL and OL.

The companion paper provides detailed anatomical data on multiple ON sheath specimens that were subjected to histological examination, but for which overall ON dimensions were insufficient for both anatomical and biomechanical study in the same eye. Histological analysis is reported here for two globes with long enough ONs that they could also be utilized for biomechanical study in the same eye. The donors had no known histories of glaucoma. In both cases, ONs were sufficiently long that a histological specimen of retrobulbar ON and its enclosing ON sheath of approximately 2–3 mm length could be excised just anterior to a specimen sufficiently long for biomechanical testing. Histological specimens were processed as described elsewhere.[24] Briefly, specimens were fixed in 10% neutral buffered formalin, dehydrated in graded alcohol solutions, embedded in paraffin, and sectioned at 10 μm thickness before staining with van

Gieson's elastin stain. Elastin density, defined as the number of pixels in an image occupied by black elastin fibers divided by the total number of pixels occupied by the ON sheath[24] in each IL and OL was determined for comparison with tensile and micro-indentation data in the same specimens.

To account for possible interocular correlation between the two eyes of each subject, statistical analysis was performed using generalized estimating equations (GEE) implemented in SPSS software (Version 24.0. Armonk, New York, USA: IBM Corporation). This was considered more rigorous than parametric statistical approaches such as analysis of variance that might be confounded by intrasubject correlations.

Results

Specimens were loaded to failure, which occurred above 30% strain. While this extremely high ultimate strain is nonphysiologic, complete stress-strain curves are illustrated in Figure 3 for completeness. As a measure of approximate linear behavior and for convenient comparison to the literature, YM was determined in the range of 10 – 15% strain for all specimen types (Table 1). The YM of the IL was about twice that of the OL ($P < 0.001$, GEE), with the whole sheath YM intermediate between the two but not significantly different from the IL ($P > 0.2$) but greater than the OL ($P < 0.001$, GEE).

Table 1. Linear elastic properties of optic nerve sheath

Tensile		Inner Layer	Outer Layer	Whole
Number of Subjects		6	5	6
Number of Specimens		13	6	37
Young's Modulus (MPa)	Mean	19.8	9.7*	15.4
	SEM	1.6	1.2	1.1
Compressive		**Inner Layer**	**Outer Layer**	
Number of Subjects		10	10	
Number of Specimens		58	44	
Stiffness (kPa)	Mean	7.9	5.2*	
	SEM	0.5	0.5	
Viscosity (kPa s)	Mean	150.8	75.6*	
	SEM	10.6	6.0	
Time Constant (Sec)	Mean	19.4	14.6*	
	SEM	0.7	0.9	

Multiple specimens were extracted from the same eyes where possible. SEM: Standard error of the mean. * – Outer layer different at $P < 0.001$ by generalized estimating equations.

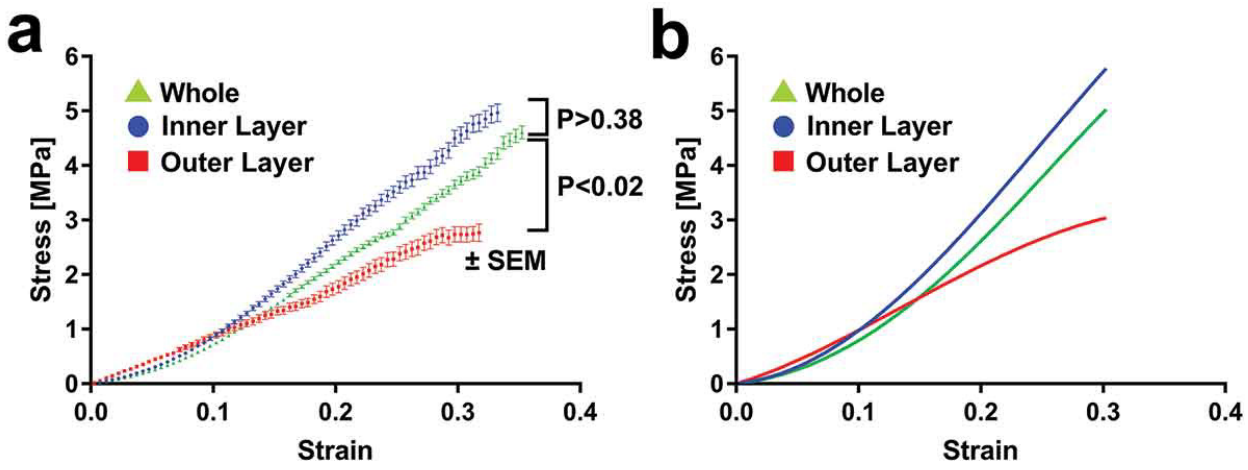

Figure 3. Nonlinear mechanical behavior of the human optic nerve sheath. (a). Mean uniaxial tensile data. Behavior of the inner layer did not differ significantly from the whole sheath ($P > .38$), but significantly differed from the outer layer. ($P < 0.02$) The number of specimens and globes is indicated in Table 1. (b). Three-parameter Ogden hyperelastic model closely fits the data in A.

To investigate possible anisotropy, whole ON sheath specimens were elongated in longitudinal (N = 16) vs. circumferential (N = 15) directions, for which YM values were

15.2 ± 1.2 MPa and 15.1 ± 2.1 MPa, respectively ($P > 0.94$, GEE). This similarity indicates that the sheath may be regarded as approximately isotropic with respect to the longitudinal and circumferential directions.

In order to obtain nonlinear characterizations, mean stress values at each corresponding strain were plotted for both layers, and for the whole ON sheath. Mean stress-strain plots averaging data for all specimens in Table 1 are shown in Figure 3a. Whole ON sheath behavior was similar to the IL ($P > 0.38$) but different from the OL ($P < 0.02$), consistent with YM behavior in the linear region. Nonlinear curve fitting was performed for each layer, achieving an excellent match to the data (Figure 3).

The resulting parameters are illustrated in Table 2. Ogden functions with three strain energy terms (N = 3) adequately described each layer's mechanical behavior within the entire strain range, including both the physiological lower part and the extremely high part approaching failure, thus providing quantitative descriptors that can be directly implemented in FEM.

Table 2. Mean Ogden hyperelastic parameters for optic nerve (ON) sheath

	μ_1 (MPa)	μ_2 (MPa)	μ_3 (MPa)	α_1	α_2	α_3
Inner Layer	445.65	-188.30	-256.60	3.09	4.12	1.92
Whole ON Sheath	40.65	-19.60	-20.21	6.01	7.81	1.07
Outer Layer	45.52	-19.10	-24.20	1.89	3.91	-2.10

The rule of mixtures was used to estimate theoretically the combined properties of the whole ON sheath based upon measured YM for each layer, by this comparison to make an inference about the predominant orientation of connective tissue fibers embedded in the sheath. In Eqs. 2 and 3, the mean f was calculated as 0.57 from OCT cross-sectional measurements

assuming constant thickness throughout the specimen length. By employing measured YM (E_i = 19.8 MPa for IL, and E_o = 9.7 MPa for OL), the rule of mixture predicts for whole sheath YM an upper bound of 15.5 MPa for parallel fiber loading and a lower bound of 13.7 MPa for transverse fiber loading, nicely matching the measured whole sheath YM of 15.4 MPa that corresponds to parallel loading.

For every indentation, stress relaxation data were fitted to the Hertzian linear viscoelastic formulation (averaged in Figure 4), from which instantaneous stiffness (analogous to YM), viscosity, and time constants were calculated. Table 1 shows averaged results for the IL and OL. Results showed the IL to be stiffer than the OL, and the IL about twice as viscous with about a 30% longer time constant ($P < 0.001$, GEE for all three comparisons).

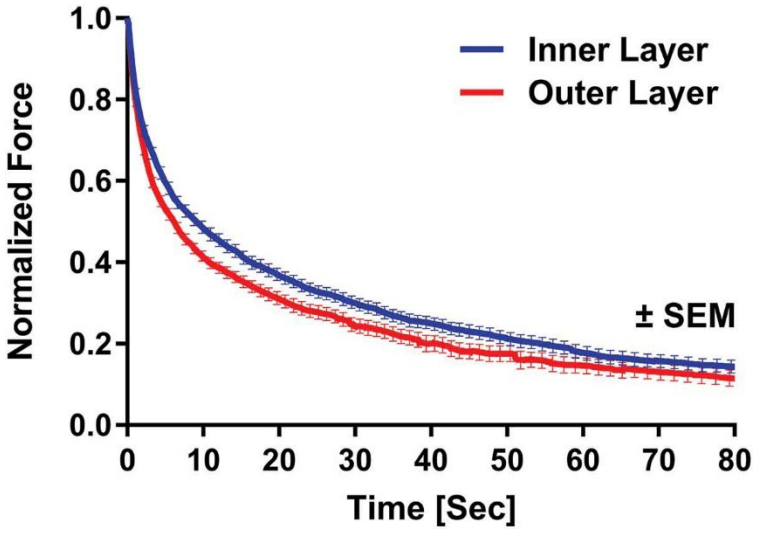

Figure 4. Mean relaxation behavior of inner layer (IL, 58 samples from 10 subjects) and outer layer (OL, 44 samples from 10 subjects) of the optic nerve sheath. The IL exhibited longer time constant (τ_{inner} = 19.4 s) than the OL (τ_{outer} = 14.6 s) corresponding to greater IL viscosity.

Two globes with very long attached ONs were used to explore a possible relationship between mechanical properties and histology suggested by differences in laminar anatomical characteristics of the ON sheath. It was seldom possible to perform both anatomical and biomechanical analyses in the same sheaths since both types of tests are destructive and only occasionally was overall ON length sufficient to provide samples for both analyses. For one such long specimen, a micro-indentation was performed to obtain local stiffness and viscosity of the two ON sheath layers. For this specimen (66-year-old female), the IL was about 30% stiffer (12.6 vs 8.9 kPa) and about three-fold more viscous (296 vs 109 kPa s) than the OL. This may be compared with about 40% higher elastin density in the IL than OL (9.8 vs 7.2%) of this same sheath. Uniaxial tensile loading was performed for the second specimen (26-year-old female). The IL exhibited about five-fold greater YM (8.1 vs 2.9 MPa) and about 60% greater elastin density (8.8 vs 5.5%) than the OL in this specimen, as illustrated in Figure 5.

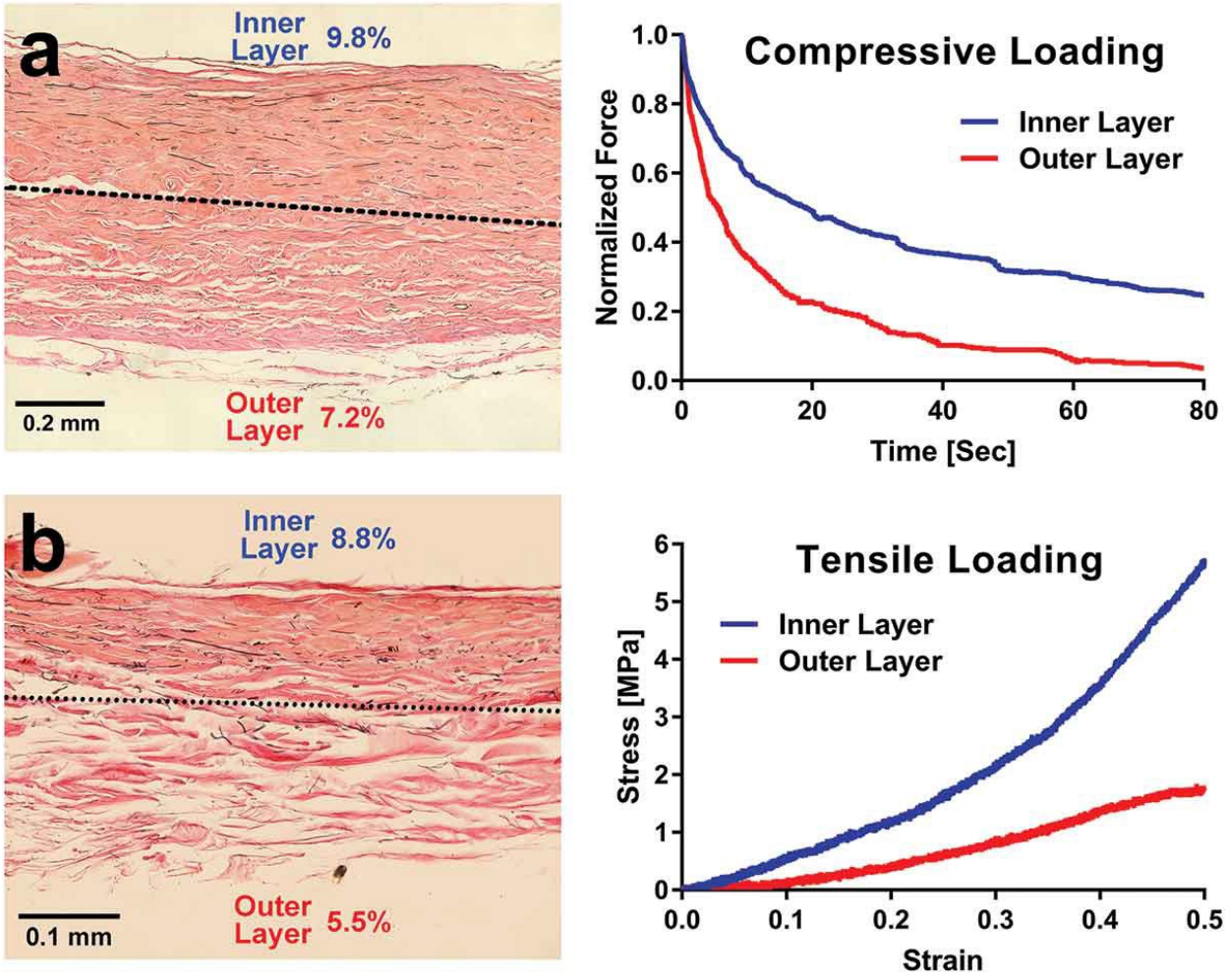

Figure 5. Mechanical properties of the ON sheath compared with elastin density in the same specimens. (a). Compressive testing in one specimen aged 66 years. The inner layer (IL) had higher elastin density (9.8%) than the outer layer (OL, 7.2%), corresponding greater stiffness (12.6 vs 8.9 kPa) and viscosity (296 vs 109 kPa s). (b). Tensile testing of a different specimen aged 26 years. Young's modulus was 8.1 MPa for the IL and 2.9 MPa for the OL, which may be compared with 8.8 and 5.5% elastin density in the two layers, respectively.

Discussion

The current study demonstrated that IL and OL of the adult human ON sheath, comprising the dural investiture of the ON, have distinct tensile and compressive mechanical properties. In both tension and compression, the IL is stiffer, and its tensile modulus dominates the behavior of

the sheath as a whole. Local micro-indentation demonstrated that ON sheath IL is significantly stiffer and more viscous than the OL.

The ON sheath exhibited similar mechanical behavior under both longitudinal and circumferential tensile loading, and this similarity is supported by the application of the rules of mixtures to compare the YM of the whole sheath with YM values of each of its layers that are readily-separable in older specimens. Therefore, it is reasonable to regard the ON sheath as a transverse isotropic material (Figure 6), a special case of orthotropic material, that is symmetric about an axis normal to the plane of isotropy,[31] along the radial axis of the ON and sheath. Transverse isotropy is common in geophysics and biological membranes, wherein the properties in the plane of the membrane differ from those perpendicular to it.

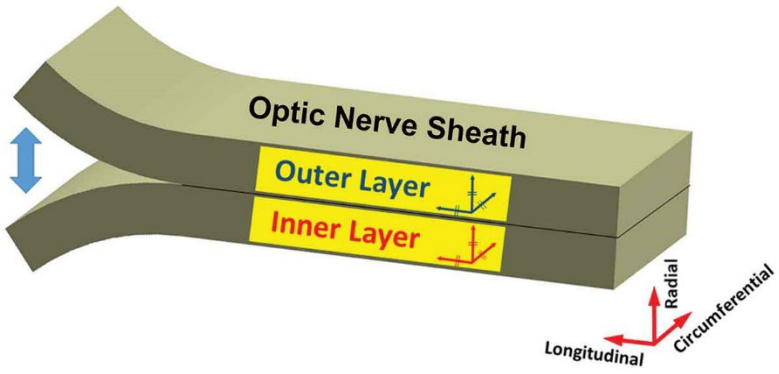

Figure 6. Transverse isotropy of optic nerve (ON) sheath that consists of inner and outer layers weakly attached along the radial boundary, so that the whole sheath has isotropic properties in the longitudinal and circumferential directions.

Examination of mechanical and anatomical characteristics in two of the same specimens suggests that the IL might be stiffer, at least in part, because it has denser elastin. Elastin is a

protein with reversible extensibility preventing dynamic tissue creep and permitting tissues to resume their shapes after loading.[32] Elastin is abundant in an artery, lung, elastic ligament, cartilage, and skin,[33,34] as well as in the lamina cribrosa,[35-37] the peripapillary scleral ring,[36] and the connective pulley tissue system of the orbit at sites of concentrated mechanical stress.[38] Elastin resists tissue deformation and has a memory permitting it to return to its undeformed shape after low-stress loading.[32,39] Elastin and collagen fibers comprise parallel mechanical elements when tissue undergoes strain: at low strain, collagen fibers extend easily with most of the load borne by elastic fibers, but at high strain, collagen fibers become limiting.[40] For example, in rat aorta, collagen digestion has little effect on stress levels at up to about 30% strain, implicating a major role for elastin in this loading regime[41] that is most relevant to the strains used in the current paper. We describe in detail elsewhere the laminar differences in elastin abundance and fiber orientation in the human ON sheath.[24] Cross-linking and absence of elastin turnover with age leads to tissue stiffening.[40] The higher elastin density in the ON sheath IL is consistent with its stiffer mechanical properties than the OL.

The biomechanical properties of the human ON sheath are important to understanding of the mechanical loads on the ON and its critical juncture with the globe at the elastic fiber ring that borders the lamina cribrosa (LC).[42] Finite element models of this mechanical behavior were first developed to clarify the effects of IOP and intracranial pressure on the LC and surrounding ocular tissues,[43,44] but have recently been expanded to include effects of eye movements.[14,22,45] Since MRI demonstrates that the ON and sheath exhaust their redundancy and tether the globe against the MR muscle in adduction exceeding about 26°[1] in a manner that correlates with OCT evidence of peripapillary deformation,[22,46,47] ON sheath mechanical behavior has become of particular interest. It has recently been proposed that eye movement, particularly adduction, may produce repetitive

strain injury to the ON and thus constitute an IOP-independent mechanism of optic neuropathy in glaucoma.[3,22] This has been proposed to be a major contributor to so-called "normal tension glaucoma" that now represents the most prevalent form of primary open-angle glaucoma worldwide.[3]

A FEM of the mechanical effects of adduction tethering of the ON has been developed based on the local material properties of bovine tissues.[14] This FEM incorporates human anatomical dimensions and predicts effects of 6° incremental adduction past the first point at which ON path redundancy is exhausted at a typical 26° adduction angle.[2] Although predicted effects vary depending on the use of linear elastic or hyperelastic material properties, the FEM suggests that the temporal ON sheath posterior to the scleral may experience 3-7% strain during adduction tethering to an angle 6° beyond the exhaustion of ON path redundancy. A more recent FEM sensitivity analysis employing hyperelastic characterization of human ocular tissues suggests that maximum strains in the ON sheath could be in the range of 5–8% for this incremental adduction.[48] It should be recognized that the physiologic limit of adduction exceeds 45°, but the ON becomes tethered for all adduction angles exceeding about 26°. Thus, strains in the ON sheath are likely to exceed 10% during larger physiological adductions. It is notable from Figure 3 that below about 10% strain, the stress in the OL exceeds that in the IL, but this relationship is reversed for greater strains. The stress-strain relationship for the OL is nearly linear up to about 30% strain for the OL but has a nonlinearly increasing slope for the IL (Figure 3). Thus, the tangent stiffness of the IL is lower than that of OL at less than 10% strain but exceeds it for more than 10% strain. The differential behavior of the two layers would tend to shift stress from the OL to the IL during larger adductions exceeding about 32°. The current data probably represent reasonable characterizations of ON sheath behavior in vivo.

We have elsewhere reported the anatomical finding that the adult (although not child) human ON sheath is distinctly bilaminar. While elastin fibers do not bridge the junction between the two layers, collagen or some other material does so in younger specimens; this interlaminar bridging appears to degenerate with advancing age, allowing the two layers to become more readily separable and presumably more mechanically independent. The present findings that the ON sheath is transversely isotropic with a stiffer and more viscous IL, have important implications for understanding the role of the ON sheath in glaucoma. No prior finite element model has represented the bilaminar nature of the ON sheath, even though the IL inserts closest to the LC and scleral canal through which the ON axons traverse into the eye. There are published data on the biomechanical properties of the ON sheath only for pigs, whose sheath is much thinner than that of humans.[23] In the absence of measured data on the human ON sheath, commonly published FEMs have assumed that it is identical to the ON sheath of the cow at 45 MPa[14] (three-fold greater than measured here for human), or fitted a Yeoh model to porcine data resulting in an approximate YM of about 4 MPa[23] (about one fourth that than measured here for humans). It is obvious that neither of the foregoing values of YM accurately represents human ON sheath, determined here to be about 15 MPa overall, but 19 MPa in the relatively critical IL, about twice that of 10 MPa in the less critical OL. It is possible that the relatively-low 2:1 specimen aspect ratio employed in the current experiments out of anatomical necessity might have caused a modest under-estimation of YM. It is known that aspect ratio is positively correlated with tensile stiffness so as a specimen aspect ratio increases from 1 to 5, stiffness increases by 36%.[25] While aspect ratio might account for as much as 30% differences in YM, it seems unlikely to account for the three- to four-fold differences between the current values for humans, and those published for pigs.

No prior model has considered ON sheath viscosity, which should eventually be considered to account for human eye saccadic eye movements typically reaching hundreds of deg/s[9] and occur about 180,000 times daily.[8] Greater IL stiffness might concentrate the stress generated by ON sheath tethering in adduction into the critical ONH area.[1] Further FEM incorporating all these aspects would provide more precise predictions of the mechanical behavior of the posterior eye, both as influenced by IOP and by eye movement.

Due to the limited length of ON tissues attached to the donated globes, it was not possible to determine if the mechanical properties of the ON sheath might vary according to distance along its entire length in the orbit. However, specimens avoided the sheath region immediately adjacent to the sclera and were from a region of the sheath in which thickness appeared uniform on inspection. In general, younger people may have more compliant peripapillary tissues than older people because of age-related stiffening in sclera[49-51] and Bruch's membrane.[52] Elastosis of the LC progresses with age,[53-56] particularly people who have open-angle glaucoma.[40,57,58] Scanning laser ophthalmoscopy demonstrates that optic disc and peripapillary tissue deformation during adduction tethering is less in older than younger healthy subjects.[59] Elastin density in the human ON sheath increases significantly with age.[24] Although specimens in the current study lacked sufficient age variation to address this question, it would of course be important to determine the relative laminar effects of age-related elastosis on the ON sheath, as sheath elastosis with advancing has been proposed as a likely etiologic factor in primary open-angle glaucoma without elevated IOP.[3] The current study had a paucity of specimens available for concurrent biomechanical and anatomical study, limiting the quantitative interpretation of anatomic-mechanical correlations. Future studies would benefit from performing such correlative studies in

additional specimens with sufficiently long ONs, and preferably in donors both affected and unaffected by glaucoma.

Conclusions

Under tensile loading, the stiffness of the IL of the human ON sheath exceeds that of the OL, with the sheath as a whole exhibiting an overall stiffness intermediate between the two layers. Under compression, the IL of the human ON sheath is stiffer and more viscous than OL. The IL contains denser elastin than the outer sheath. The greater stiffness and viscosity of the elastin-rich IL of the ON sheath may be important in concentrating mechanical stress near the LC when the sheath is under tension during eye movement.

References

1. Demer JL. Optic nerve sheath as a novel mechanical load on the globe in ocular duction. Invest Ophthalmol Vis Sci. 2016;57:1826–38. doi:10.1167/iovs.15-18718.
2. Suh SY, Le A, Shin A, Park J, Demer JL. Progressive deformation of the optic nerve head and peripapillary structures by graded horizontal duction. Invest Ophthalmol Vis Sci. 2017;58:5015–21. doi:10.1167/iovs.17-22596.
3. Demer JL, Clark RA, Suh SY, Giaconi JA, Nouri-Mahdavi K, Law SK, Bonelli L, Coleman AL, Caprioli J. Magnetic resonance imaging of optic nerve traction during adduction in primary open-angle glaucoma with normal intraocular pressure. Invest Ophthalmol Vis Sci. 2017;58:4114–25. doi:10.1167/iovs.17-22093.

4. Apt L. An anatomical reevaluation of rectus muscle insertions. Trans Am Ophthalmol Soc. 1980;78:365–75.
5. Wang YX, Jiang R, Wang NL, Xu L, Jonas JB. Acute peripapillary retinal pigment epithelium changes associated with acute intraocular pressure elevation. Ophthalmology. 2015;122:2022–28. doi:10.1016/j.ophtha.2015.06.005.
6. Fortune B. Pulling and tugging on the retina: mechanical impact of glaucoma beyond the optic nerve head. Inv Ophtalmol Vis Sci. 2019;60:26–35. doi:10.1167/iovs.18-25837.
7. Sibony PA, Hou W. Adduction-Induced deformations evoke peripapillary folds in papilledema. Ophthalmology. 2019;126:912–14. doi:10.1016/j.ophtha.2018.12.043.
8. Robinson DA. Control of eye movements. In: Brooks VB editor. The nervous system, handbook of physiology. Vol. II. Baltimore (MD): Williams & Wilkins; 1981. p. 1275–320.
9. Wu CC, Kowler E. Timing of saccadic eye movements during visual search for multiple targets. J Vis. 2013;3:13.
10. Leclair-Visonneau L, Oudiette D, Gaymard B, Leu-Semenescu S, Arnulf I. Do the eyes scan dream images during rapid eye movement sleep? Evidence from the rapid eye movement sleep behaviour disorder model. Brain. 2010;133:1737–46. doi:10.1093/brain/awq110.
11. Anastasopoulos D, Ziavra N, Hollands M, Bronstein A. Gaze displacement and inter-segmental coordination during large whole body voluntary rotations. Exp Brain Res. 2009;193:323–36. doi:10.1007/s00221-008-1627-y.
12. Tomlinson RD, Bahra PS. Combined eye-head gaze shifts in the primate. II. Interaction between saccades and the vestibuloocular reflex. J Neurophysiol. 1986;56:1558–70. doi:10.1152/jn.1986.56.6.1558.
13. Tomlinson RD, Bahra PS. Combined eye-head gaze shifts in the primate. I Metrics J Neurophysiol. 1986;56:1542–57. doi:10.1152/jn.1986.56.6.1542.
14. Shin A, Yoo L, Park J, Demer JL. Finite element biomechanics of optic nerve sheath traction in adduction. J Biomech Eng. 2017;139(10).
15. Garrity JA. What is the current status of optic nerve sheath fenestration? J Neuroophthalmol. 2016;36:231–34. doi:10.1097/WNO.0000000000000438.

16. Elkington AR, Inman CB, Steart PV, Weller RO. The structure of the lamina cribrosa of the human eye: an immunocytochemical and electron microscopical study. Eye (Lond). 1990;4(Pt 1):42–57. doi:10.1038/eye.1990.5.
17. Spoerl E, Boehm AG, Pillunat LE. The influence of various substances on the biomechanical behavior of lamina cribrosa and peripapillary sclera. Invest Ophthalmol Vis Sci. 2005;46:1286–90. doi:10.1167/iovs.04-0978.
18. Downs JC, Suh JK, Thomas KA, Bellezza AJ, Burgoyne CF, Hart RT. Viscoelastic characterization of peripapillary sclera: material properties by quadrant in rabbit and monkey eyes. J Biomech Eng. 2003;125:124–31. doi:10.1115/1.1536930.
19. Downs JC, Suh JK, Thomas KA, Bellezza AJ, Hart RT, Burgoyne CF. Viscoelastic material properties of the peripapillary sclera in normal and early-glaucoma monkey eyes. Invest Ophthalmol Vis Sci. 2005;46:540–46. doi:10.1167/iovs.04-0114.
20. Sigal IA, Flanagan JG, Ethier CR. Factors influencing optic nerve head biomechanics. Invest Ophthalmol Vis Sci. 2005;46:4189–99. doi:10.1167/iovs.05-0541.
21. Feola AJ, Myers JG, Raykin J, Mulugeta L, Nelson ES, Samuels BC, Ethier CR. Finite element modeling of factors influencing optic nerve head deformation due to intracranial pressure. Invest Ophthalmol Vis Sci. 2016;57:1901–11. doi:10.1167/iovs.15-17573.
22. Wang X, Rumpel H, Lim WE, Baskaran M, Perera SA, Nongpiur ME, Aung T, Milea D, Girard MJ. Finite element analysis predicts large optic nerve strains heads during horizontal eye movements. Invest Ophthalmol Vis Sci. 2016;57:2452–62. doi:10.1167/iovs.15-18986.
23. Raykin J, Forte TE, Wang R, Feola A, Samuels BC, Myers JG, Mulugeta L, Nelson ES, Gleason RL, Ethier CR. Characterization of the mechanical behavior of the optic nerve sheath and its role in spaceflight-induced ophthalmic changes. Biomech Model Mechanobiol. 2017;16:33–43. doi:10.1007/s10237-016-0800-7.
24. Le A, Baig A, Shin A, Poukens V, Demer JL. 2017. Bilaminar structure of the human optic nerve sheath. Curr Eye Res.
25. Carew EO, Patel J, Garg A, Houghtaling P, Blackstone E, Vesely I. Effect of specimen size and aspect ratio on the tensile properties of porcine aortic valve tissues. Ann Biomed Eng. 2003;31:526–35. doi:10.1114/1.1568116.

26. Shin A, Yoo L, Demer JL. Independent active contraction of extraocular muscle compartments. Inv Ophtalmol Vis Sci. 2015;56:199–206. doi:10.1167/iovs.14-15968.
27. Mihai LA, Chin L, Janmey PA, Goriely A. A comparison of hyperelastic constitutive models applicable to brain and fat tissues. J R Soc Interface. 2015;12:0486. doi:10.1098/rsif.2015.0486.
28. Ogden RW Large deformation isotropic elasticity - Correlation of theory and experiment for incompressible rubberlike solids. Proc. Royal Soc. London Series A – Mathematical and Physical Sciences. 1972;326:565.
29. Yoo L, Reed J, Shin A, Kung J, Gimzewski JK, Poukens V, Goldberg RA, Mancini R, Ta ban M, Moy R, et al. Characterization of ocular tissues using microindentation and hertzian viscoelastic models. Invest Ophthalmol Vis Sci. 2011;52:3475–82. doi:10.1167/iovs.10-6867.
30. Askeland DR, Fulay PP, Wright WJ. The Science and Engineering of Materials. 6 ed. Boston, MA: Cengage Learning; 2010.
31. Thomsen L. Weak Elastic-Anisotropy. Geophysics. 1986;51:1954–66. doi:10.1190/1.1442051.
32. Patel A, Fine B, Sandig M, Mequanint K. Elastin biosynthesis: the missing link in tissue-engineered blood vessels. Cardiovasc Res. 2006;71:40–49. doi:10.1016/j.cardiores.2006.02.021.
33. Debelle L, Alix AJ. The structures of elastins and their function. Biochimie. 1999;81:981–94. doi:10.1016/S0300-9084(99)00221-7.
34. Daamen WF, Veerkamp JH, van Hest JC, van Kuppevelt TH. Elastin as a biomaterial for tissue engineering. Biomaterials. 2007;28:4378–98. doi:10.1016/j.biomaterials.2007.06.025.
35. Quigley HA, Dorman-Pease ME, Brown AE. Quantitative study of collagen and elastin of the optic nerve head and sclera in human and experimental monkey glaucoma. Curr Eye Res. 1991;10:877–88. doi:10.3109/02713689109013884.
36. Quigley HA, Brown A, Dorman-Pease ME. Alterations in elastin of the optic nerve head in human and experimental glaucoma. Br J Ophthalmol. 1991;75:552–57. doi:10.1136/bjo.75.9.552.

37. Oyama T, Abe H, Ushiki T. The connective tissue and glial framework in the optic nerve head of the normal human eye: light and scanning electron microscopic studies. Arch Histol Cytol. 2006;69:341–56. doi:10.1679/aohc.69.341.
38. Kono R, Poukens V, Demer JL. Quantitative analysis of the structure of the human extraocular muscle pulley system. Invest Ophthalmol Vis Sci. 2002;43:2923–32.
39. Oxlund H, Manschot J, Viidik A. The role of elastin in the mechanical properties of skin. J Biomech. 1988;21:213–18. doi:10.1016/0021-9290(88)90172-8.
40. Hernandez MR. Ultrastructural immunocytochemical analysis of elastin in the human lamina cribrosa. Changes in elastic fibers in primary open-angle glaucoma. Invest Ophthalmol Vis Sci. 1992;33:2891–903.
41. Oxlund H, Andreassen TT. The roles of hyaluronic acid, collagen and elastin in the mechanical properties of connective tissues. J Anat. 1980;131:611–20.
42. Tektas OY, Lutjen-Drecoll E, Scholz M. Qualitative and quantitative morphologic changes in the vasculature and extracellular matrix of the prelaminar optic nerve head in eyes with POAG. Invest Ophthalmol Vis Sci. 2010;51:5083–91. doi:10.1167/iovs.09-5101.
43. Burgoyne CF, Downs JC, Bellezza AJ, Suh JK, Hart RT. The optic nerve head as a biomechanical structure: a new paradigm for understanding the role of IOP-related stress and strain in the pathophysiology of glaucomatous optic nerve head damage. Prog Retin Eye Res. 2005;24:39–73. doi:10.1016/j.preteyeres.2004.06.001.
44. Sigal IA, Ethier CR. Biomechanics of the optic nerve head. Exp Eye Res. 2009;88:799–807. doi:10.1016/j.exer.2009.02.003.
45. Wang X, Fisher LK, Milea D, Jonas JB, Girard MJ. Predictions of optic nerve traction forces and peripapillary tissue stresses following horizontal eye movements. Invest Ophthalmol Vis Sci. 2017;58:2044–53. doi:10.1167/iovs.16-21319.
46. Chang MY, Shin A, Park J, Nagiel A, Lalane RA, Schwartz SD, Demer JL. Deformation of optic nerve head and peripapillary tissues by horizontal duction. Am J Ophthalmol. 2017;174:85–94. doi:10.1016/j.ajo.2016.10.001.
47. Sibony PA. Gaze-evoked deformations of the peripapillary retina and papilledema and ischemic optic neuropathy. Inv Ophtalmol Vis Sci. 2016;57:4979–87. doi:10.1167/iovs.16-19931.

48. Park J, Giaconi JA, Nouri-
Mahdavi K, Law SL, Bonelli L, Coleman AL, Caprioli J, Demer JL. Finite element analysis (FEA) of anatomical factors exaggerating optic nerve (ON) strain during adduction tethering in primary open-angle glaucoma (POAG) without elevated intraocular pressure (IOP). ARVO Abstracts. 2019. 6172.

49. Geraghty B, Jones SW, Rama P, Akhtar R, Elsheikh A. Age-related variations in the biomechanical properties of human sclera. J Mech Behav Biomed Mater. 2012;16:181–91. doi:10.1016/j.jmbbm.2012.10.011.

50. Coudrillier B, Tian J, Alexander S, Myers KM, Quigley HA, Nguyen TD. Biomechanics of the human posterior sclera: age- and glaucoma-related changes measured using inflation testing. Invest Ophthalmol Vis Sci. 2012;53:1714–28. doi:10.1167/iovs.11-8009.

51. Avetisov ES, Savitskaya NF, Vinetskaya MI, Iomdina EN. A study of biochemical and biomechanical qualities of normal and myopic eye sclera in humans of different age groups. Metab Pediatr Syst Ophthalmol. 1983;7:183–88.

52. Booij JC, Baas DC, Beisekeeva J, Gorgels TG, Bergen AA. The dynamic nature of Bruch's membrane. Prog Retin Eye Res. 2010;29:1–18. doi:10.1016/j.preteyeres.2009.08.003.

53. Albon J, Karwatowski WS, Easty DL, Sims TJ, Duance VC. Age related changes in the non-collagenous components of the extracellular matrix of the human lamina cribrosa. Br J Ophthalmol. 2000;84:311–17. doi:10.1136/bjo.84.3.311.

54. Albon J, Karwatowski WS, Avery N, Easty DL, Duance VC. Changes in the collagenous matrix of the aging human lamina cribrosa. Br J Ophthalmol. 1995;79:368–75. doi:10.1136/bjo.79.4.368.

55. Albon J, Purslow PP, Karwatowski WS, Easty DL. Age related compliance of the lamina cribrosa in human eyes. Br J Ophthalmol. 2000;84:318–23. doi:10.1136/bjo.84.3.318.

56. Leung LK, Ko MW, Lam DC. Effect of age-stiffening tissues and intraocular pressure on optic nerve damages. Mol Cell Biomech. 2012;9:157–73.

57. Pena JD, Netland PA, Vidal I, Dorr DA, Rasky A, Hernandez MR. Elastosis of the lamina cribrosa in glaucomatous optic neuropathy. Exp Eye Res. 1998;67:517–24. doi:10.1006/exer.1998.0539.

58. Netland PA, Ye H, Streeten BW, Hernandez MR. Elastosis of the lamina cribrosa in pseudoexfoliation syndrome with glaucoma. Ophthalmology. 1995;102:878–86. doi:10.1016/S0161-6420(95)30939-6.

59. Le A, Chen J, Lesgart M, Gawargious BA, Suh SY, Demer JL. Age-dependent deformation of the optic nerve head and peripapillary retina by horizontal duction. Am J Ophthalmol. 2019. doi:10.1016/j.ajo.2019.08.017.

60. Lee EH, Radok JRM. The contact problem for viscoelastic bodies. J Appl Mech. 1960;27:438–44. doi:10.1115/1.3644020.

61. Mattice J, Lau A, Oyem M, Kent R. Spherical indentation load-relaxation of soft biological tissues. J Mater Res. 2006;21:2003–10. doi:10.1557/jmr.2006.0243.

62. Johnson KL. Contact Mechanics. Cambridge (UK): Cambridge University Press; 1985.

63. Oyen ML. Sopherical indentation creep following ramp loading. J Mater Res. 2005;20:2094–100. doi:10.1557/JMR.2005.0259.

64. Roylance D. Engineering Viscoelasticity. Cambridge: Department of Materials Science and Engineering - Massachusetts Institute of Technology; 2001.

Chapter 3. Ocular Tissue Characterization

The finite element model (FEM) is an efficient and non-destructive numerical method to predict the biomechanical behavior of biological tissue, but there are many requirements that need to be fulfilled. One of the most important requirements is a specification of material properties reflected in the constitutive equations of the model components. When an external stimulus is applied, the constitutive equation tells us how a solid deforms in response; the assumptions about the constitutive equation influence the details of the mechanical response. Therefore, understanding of the material property of any ocular tissue is the first step to understanding its biomechanical behavior in the eye when we investigate possible biomechanical causes of eye diseases.

Since 1972, many characterizations have been conducted for ocular tissues using various test methods such as pressure[1, 2], compression[3], uniaxial[4-6], and biaxial tensile loading[7]. Corneal and scleral experiments were extensively performed in animal eye experiments. The ultimate goal of most studies was to demonstrate the effect of high IOP in inducing ON damage. For these studies, material properties of the ocular globe were required to estimate the mechanical response to high IOP, but not in tissues in the orbit posterior to the globe. Although some FEMs included the anterior part of the ON and its sheath, due to the lack of empirical studies, the material properties were roughly borrowed from animal or non-ocular human tissues data, and a highly simplified anatomic structure

was assumed. For the better understanding of ocular behavior to the high IOP and the other stimuli such as ON tethering, this thesis explored the material properties of human ocular tissues including globe, ON, and ON sheath.

References

1. Coudrillier B, Tian J, Alexander S, Myers KM, Quigley HA, Nguyen TD. Biomechanics of the human posterior sclera: Age- and glaucoma-related changes measured using inflation testing. *Invest Ophthalmol Vis Sci* 2012;53:1714-1728.
2. Woo SL, Kobayashi AS, Schlegel WA, Lawrence C. Nonlinear material properties of intact cornea and sclera. *Exp Eye Res* 1972;14:29-39.
3. Friberg TR, Lace JW. A comparison of the elastic properties of human choroid and sclera. *Exp Eye Res* 1988;47:429-436.
4. Elsheikh A, Geraghty B, Alhasso D, Knappett J, Campanelli M, Rama P. Regional variation in the biomechanical properties of the human sclera. *Exp Eye Res* 2010;90:624-633.
5. Wollensak G, Spoerl E. Collagen crosslinking of human and porcine sclera. *J Cataract Refract Surg* 2004;30:689-695.
6. Downs JC, Suh JK, Thomas KA, Bellezza AJ, Hart RT, Burgoyne CF. Viscoelastic material properties of the peripapillary sclera in normal and early-glaucoma monkey eyes. *Invest Ophthalmol Vis Sci* 2005;46:540-546.
7. Eilaghi A, Flanagan JG, Tertinegg I, Simmons CA, Wayne Brodland G, Ross Ethier C. Biaxial mechanical testing of human sclera. *J Biomech* 2010;43:1696-1701.

3.1. Uniaxial Micro-Tensile Experiment

The following study performed biomechanical characterization of human sclera, ON, and ON sheath using a custom-built micro-tensile machine to further extend

characterizations of human sclera, and investigate previously-undefined material properties of ON and its sheath. In addition, the study investigated the effect of preconditioning in tensile testing, reporting results both with and without preconditioning. The following characterization study was reported in *Biomechanics and Modeling in Mechanobiology*. This extensive ocular characterization took more than 5 years of effort to reach publication. Even though it is basic characterization research, the submission was challenged due to the research groups that emphasize the role of IOP and dismiss the hypothesis of ON tethering. We suspect that this opposition is attributable to an extensive FEM literature by these groups using assumed or extrapolated animal tissue material properties that differ by orders of magnitude from the properties we report for human tissue.

Publications included in this chapter:

3.1.1. **Park J**, Shin A, Jafari S, Demer JL. Material properties and effect of preconditioning of human sclera, optic nerve, and optic nerve sheath. *Biomech Model Mechanobiol* 2021;20:1-11.

Contributions to the study: Joseph Park contributed as the first author of this study and Joseph Demer supervised the study as a corresponding author. All authors, including Park (70%), Shin (25%), and Jafari (5%), dissected the eye, prepared specimens, and performed uniaxial tensile experiments for the characterization of the human ocular tissues. Park analyzed the data, drew graphs and drawings, and wrote multiple versions of the manuscript for publication.

3.1.1. Material Properties and Effect of Preconditioning of Human Sclera, Optic Nerve, and Optic Nerve Sheath

Joseph Park[1, 2], Andrew Shin[5], Somaye Jafari[1] and Joseph L. Demer[1 ,3 ,4]

[1] Department of Ophthalmology, Jules Stein Eye Institute, Los Angeles, CA, USA.
[2] Department of Bioengineering, University of California, Los Angeles, CA, USA.
[3] Biomedical Engineering Interdepartmental Program, University of California, Los Angeles, CA, USA.
[4] Neuroscience Interdepartmental Program, University of California, Los Angeles, CA, USA.
[5] Intelon Optics Inc., Lexington, MA, USA.

Abstract

The optic nerve (ON) is a recently recognized tractional load on the eye during larger horizontal eye rotations. In order to understand the mechanical behavior of the eye during adduction, it is necessary to characterize material properties of the sclera, ON, and in particular its sheath. We performed tensile loading of specimens taken from fresh post-mortem human eyes to characterize the range of variation in their biomechanical properties and determine the effect of preconditioning. We fitted reduced polynomial hyperelastic models to represent the nonlinear tensile behavior of the anterior, equatorial, posterior, and peripapillary sclera, as well as the ON and its sheath. For comparison, we analyzed tangent moduli in low and high strain regions to represent stiffness.

Scleral stiffness generally decreased from anterior to posterior ocular regions. The ON had the lowest tangent modulus but was surrounded by a much stiffer sheath. The low-strain hyperelastic behaviors of adjacent anatomical regions of the ON, ON sheath, and posterior sclera were similar as appropriate to avoid discontinuities at their boundaries. Regional stiffnesses within individual eyes were moderately correlated, implying that mechanical properties in one region of an eye do not reliably reflect properties of another region of that eye and that potentially pathological combinations could occur in an eye if regional properties are discrepant. Preconditioning modestly stiffened ocular tissues, except peripapillary sclera that softened.

The nonlinear mechanical behavior of posterior ocular tissues permits their stresses to match closely at low strains, although progressively increasing strain causes particularly great stress in the peripapillary region.

Introduction

The eye is a pressurized mechanical structure that is set in nearly constant rotational and translational motion within its orbital gimbal suspension by the actions of multiple extraocular muscles [1]. Moreover, the optic nerve (ON) that conveys visual signals from the eye to the brain also acts as a deforming [2-4] mechanical load on the moving eye [5], and is surrounded by a sheath of cerebrospinal fluid internally loaded by communication with intracranial pressure (ICP) [6-9]. Excessive intraocular pressure (IOP) is implicated in progressive damage to visual function in glaucoma [10]. Repetitive strain injury to the eye caused by eye movements has been proposed both to be involved in ON damage in glaucoma [7, 11-13], and progressive, damaging elongation and distortion of globe shape in axial myopia [14]. The ON is also susceptible to visually-threatening damage from pathologically elevated ICP [6, 7], and may also be damaged during distention of its sheath by fluid shifts that occur in microgravity during space flight [9, 15].

A critical consideration in each of the foregoing disorders is the biomechanical behavior of the ocular and orbital tissues. Classical uniaxial tensile loading has been the most popular experimental method of characterizing ocular biomechanics [16-18], but some investigators have characterized sclera using biaxial tensile loading and whole-globe inflation [19, 20]. The sclera has even been characterized by optomechanical birefringence [21]. While there have been extensive investigations of anterior ocular tissues such as cornea [22-24], sclera [17, 19, 25-28], and the lamina cribrosa (LC) of the optic disc [29-33], the biomechanical properties of tissues posterior to the globe have been comparatively neglected. Biomechanical properties of the bovine ON have been reported [7], but human ON data are currently lacking, despite the presence of abundant connective tissue around and within the human ON that distinguishes it from other neural tissue such as brain

[34]. The mechanical behavior of porcine ON sheath has been explored using inflation and axial loading [9], but porcine anatomy differs substantially from the bilaminar human sheath [35] in a manner likely to alter its mechanical properties [36]. It is vital to understand quantitatively the biomechanical behavior of human posterior ocular tissues such as the orbital ON and ON sheath, since these are both essential links in transmission of the sense of sight to the brain, mechanically load the globes they interact with the oculorotary muscles [5], and may influence scleral remodeling and ocular elongation as may contribute to development and progression of myopia [14].

Preconditioning is the classical process of releasing residual stress that remains in an unloaded organ [37, 38], and has generally been presumed important in the characterization of biomaterials. However, the effect of preconditioning depends on the protocol and the type of tissue and may vary among tissue types [39]. Since most studies have included preconditioning as a matter of routine before any tensile loading [37, 39-41], the significance of preconditioning for ocular tissues is currently unknown.

The current study therefore aimed in human tissue to characterize nonlinear, uniaxial tensile behavior in multiple scleral regions, in the ON, and its sheath, as well as the range of inter-individual and intraocular variation in these properties, and the degree to which properties in one region of a given eye might predict properties elsewhere in that eye. Since there have been no reported investigations of the effects of preconditioning on human ocular tissues, this study also compared tensile results with and without preconditioning in nearly identical adjacent specimens from multiple ocular regions to characterize the effects of preconditioning.

Methods

Specimen Sources. We studied 38 pairs of fresh, unfixed human eyes, with ONs attached, collected within 3 days post-mortem from four eye banks (Lions Gift of Sight, Saint Paul, MN, San Diego Eye Bank, San Diego, CA, SightLife, Seattle, WA, and OneLegacy, Los Angeles, CA). Mean donor age was 71±14 (range 26 – 101) years, with equal numbers of males and females, all free of known ocular diseases. Eyes were obtained in conformity with the Declaration of Helsinki.

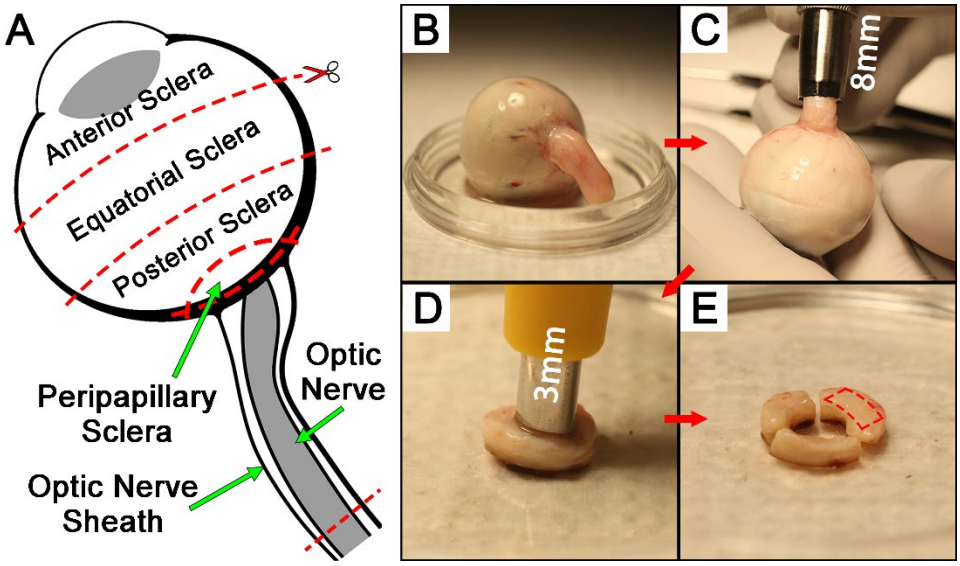

Figure 1. Specimen dissection. (A) Ocular tissue was divided into anterior, equatorial, posterior, and peripapillary sclera, and optic nerve and its sheath. (B) Muscles and connective tissues were excised. (C) Posterior tissues were isolated using an 8 mm inside diameter trephine. (D) The optic nerve head was removed with a 3 mm trephine. (E) The annular peripapillary sclera was divided into thirds and trimmed into rectangular shapes along the circumferential direction only due to the limited size.

Specimen Preparation. Specimens were stored in iced lactated Ringer's solution during preparation and were dissected into six types: anterior, equatorial, posterior, and peripapillary sclera; ON, and ON sheath (Figure 1A). A representative specimen is illustrated in Figure 1B. The method of extraction of peripapillary sclera with a punch is illustrated in Figs. 1C – E. All except

the cylindrical ON were trimmed into a rectangular shape. Peripapillary scleral specimens were oriented with long dimensions circumferentially around the optic disc, and all other scleral tissues were taken equally oriented with long dimensions meridionally and circumferentially. Specimens of the ON sheath were oriented in both circumferential and longitudinal in equal numbers because our earlier study indicated that tensile properties of the ON sheath are similar in both orientations [36]. The ends of the ON and its sheath were glued with cyanoacrylate to thin cardboard to prevent slippage (Figure 2). Mean specimen dimensions (length × width ± standard deviation, SD) measured by digital caliper were 4.0±0.6 mm × 0.8±0.2 mm for anterior sclera, 4.1±0.6 mm × 0.9±0.2 mm for equatorial sclera, 4.0±0.7 mm × 0.9±0.2 mm for posterior sclera, 2.7±0.8 mm × 0.8±0.1 mm for peripapillary sclera, and 4.5±1.3 mm × 0.8±0.2 mm for ON sheath. Mean aspect ratios were 4.9, 4.7, 4.6, 3.5, and 5.6, respectively. The entire available length of the ON was untrimmed to minimize potential experimental artifact due to the thick cylindrical ends. Mean ON specimen length was 5.7±2.4 mm.

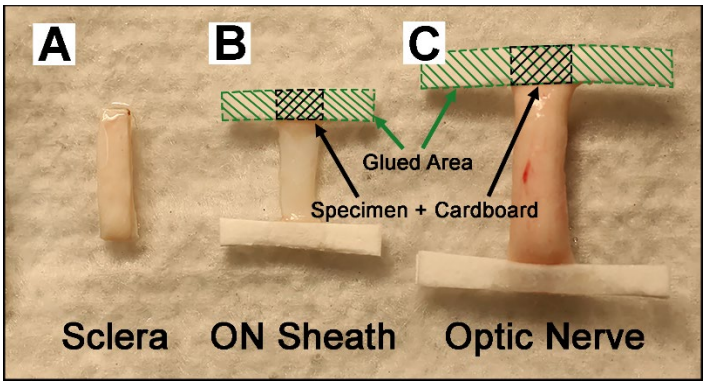

Figure 2. Specimen preparation. (A) The thickness of scleral tissue was enough to securely clamp on each end. (B & C) The cardboard was glued with cyanoacrylate to the ends of the thin ON sheath and rounded ON to avoid slippage in the clamps.

Tensile Testing. Tissues were loaded uniaxially using a previously described apparatus [7, 42] in an environmental chamber maintained by a heated water bath at 37°C temperature and approaching 100% humidity. The initial sample length was measured using a digital caliper (Mitutoyo Co., Kawasaki, Japan). The cross-sectional area was measured using optical coherence tomography (OCT; Thorlabs Inc., Newton, NJ) after applying 0.05 N preload to eliminate slack. Loading was continuously applied at a constant rate of 0.1 mm/sec. The strain was measured based on the distance from clamp to clamp in the load cell.

Preconditioning. Specimens were treated in two fashions: approximately half of the specimens from 17 eyes underwent preconditioning and other half did not. In 21 other eyes, no preconditioning was performed. For preconditioned specimens, we applied five cycles of tensile loading to 5% maximum strain. Figure 3 illustrates that the stress-strain curves converged to consistent responses after 2 - 3 loading cycles, verifying that the 5 cycles uniformly applied were sufficient to achieve stable pre-conditioning. The decreasing area underneath of stress-strain curves indicates release residual stress, and negative stress after the first preconditioning cycle is typical of preconditioning studies [43-45].

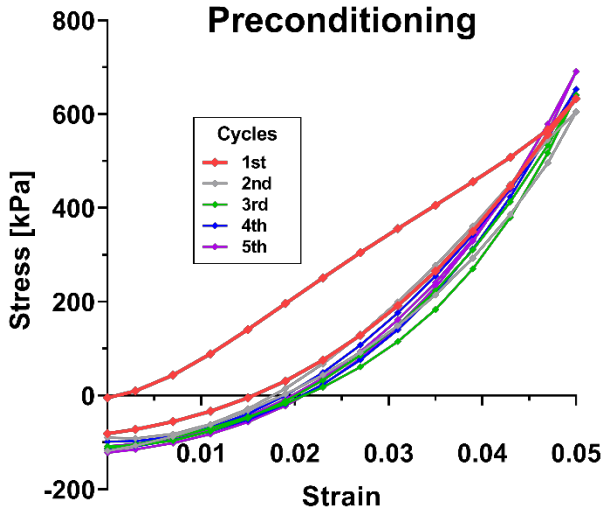

Figure 3. Preconditioning of posterior sclera. Stress-strain curves converged after 2 to 3 cycles of 5% cyclic loading.

Material Property Analysis. Force-displacement curves were converted into Cauchy stress-strain curves, to which the reduced polynomial hyperelastic models were fit using a material evaluation tool in ABAQUS 2020 (Dassault Systèmes SIMULIA Corp., Johnston, RI). This evaluation tool limits its outputs to functions that are stable in the ABAQUS numerical simulation environment for the specific empirical stress-strain curve provided. Where multiple functions were stable for a tissue, we chose the function that fits best. The strain energy density function U of the reduced polynomial model is expressed by

$$U = \sum_{i=1}^{N} C_{i0} (\bar{I}_1 - 3)^i + \sum_{i=1}^{N} \frac{1}{D_i} (J_{el} - 1)^{2i} \qquad \text{Eqn. 1}$$

where $\bar{I}_1$ is the first strain invariant, C_{i0} and D_i are material constants, J_{el} determines the elastic volume ratio. Depending on the stability and quality of fitting, we employed either fourth or sixth order reduced polynomial hyperelastic models for each tissue. For simplicity, the tissues were

assumed to be isotropic and nearly incompressible (Poisson's ratio = 0.49) to avoid singularity in computations.

Results

Hyperelastic Properties of Preconditioned Tissue. Although all tissues exhibited hyperelastic behavior as described below, it is also informative to compare tangent moduli at 3% low ($E_{3\%}$) and 7% high strain ($E_{7\%}$). Data are illustrated in Figure 4 for specimens subjected to preconditioning. The tangent modulus at 3% strain (mean ± standard deviation, SD) of the anterior sclera was 30.8±13.1 MPa, roughly twice that of equatorial and posterior sclera at 17.7±8.7 MPa, and 13.3±5.3 MPa, respectively. Peripapillary sclera near the ON junction, which was loaded circumferentially, had the lowest tangent modulus among all scleral tissues of 3.5±1.4 MPa at 3% strain. However, because of its nonlinearity, peripapillary sclera exhibited a gradual increase in tangent modulus, reaching 27.7 MPa at 30% strain. Furthermore, 8 out of 11 peripapillary scleral specimens tested had ultimate strain exceeding 34%, which is not apparent from the graph in Figure 4 that was truncated to 20% strain for comparison with the other tissues. The tangent modulus of ON sheath at 3% strain was 10.0±5.8 MPa, slightly lower than that of posterior sclera at 13.3±5.4 MPa. The ON, which was loaded longitudinally, was the most compliant with 3.4±2.2 MPa modulus at 3% strain.

Relative to 3% strain, the moduli at 7% strain of the anterior, equatorial, posterior, and peripapillary sclera were greater by 69% ($E_{7\%}$ = 52.0±15.5 MPa, $P < 0.002$), 50% ($E_{7\%}$ = 26.6±12.3 MPa, $P = 0.044$), 53% ($E_{7\%}$ = 20.4±6.8 MPa, $P = 0.018$), and 146% ($E_{7\%}$ = 8.6±4.0 MPa, $P < 0.001$), respectively (Figure 4). At the higher strain, the ON sheath was significantly stiffer by 138% ($E_{7\%}$

= 23.8±15.0 MPa, P = 0.010), and ON tangent modulus increased insignificantly by 85% ($E_{7\%}$ = 6.3±3.3 MPa, P=0.077).

The variability of data from individual specimens was quantified as the coefficient of variation (CV), the quotient of the SD divided by the mean value for that computed modulus. For 3% strain, the CV values were 0.43, 0.49, 0.40, and 0.40 for anterior, equatorial, posterior, and peripapillary sclera, respectively.

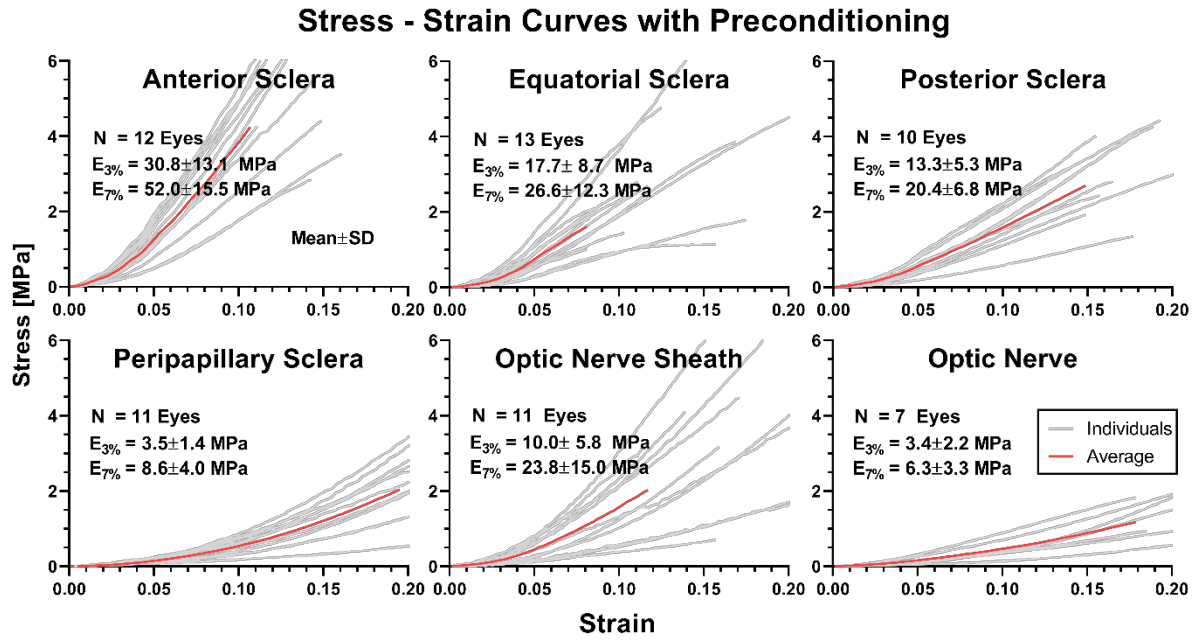

Figure 4. Tensile stress-strain relationships of ocular tissues with preconditioning. The $E_{3\%}$ and $E_{7\%}$ represent tangent moduli at low (3%) and high (7%) strain, respectively. Red solid curves indicate mean behaviors, and light grey lines represent individual specimens. Data are truncated to 0.20 strain for graphical clarity, although ultimate strain for peripapillary sclera was greater. N - Number of eyes.

The forgoing data illustrate obvious nonlinear stress-strain behavior for all of the ocular tissues and regions evaluated. This nonlinearity permits tangent modulus to match between and

among anatomically contiguous regions in a lower range of strains, yet be disparate outside this range. For example, Figure 5A shows that peripapillary sclera and ON behaved nearly identical to one another up to 7% tensile strain (95% confidence intervals of polynomial and exponential fits overlapped), above which peripapillary sclera became stiffer (95% confidence intervals for linear fits differed widely). In contrast, posterior sclera and ON sheath exhibited tensile behavior similar to one another throughout the entire range of strains (95% confidence intervals of polynomial fits overlapped, Figure 5B).

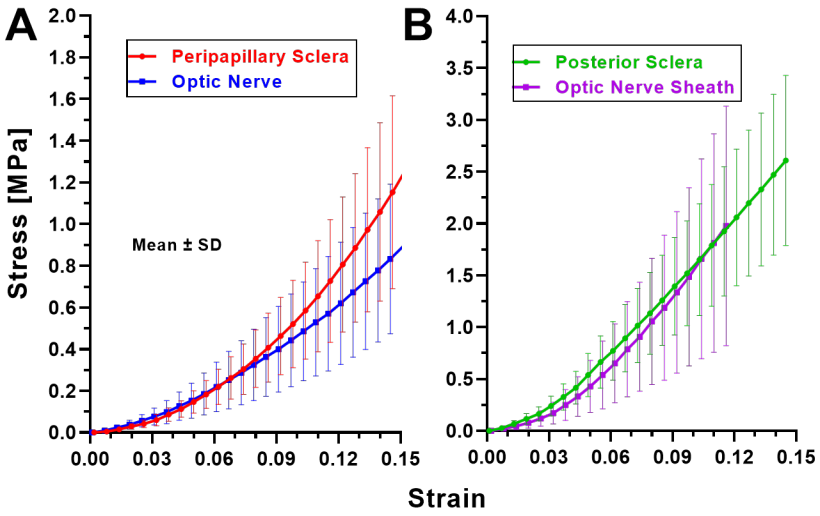

Figure 5. Stress-strain curves in anatomically contiguous tissues. (A) Up to about 7% strain, curves for the optic nerve and peripapillary sclera were nearly identical, but peripapillary sclera stiffened for larger strains. (B) Curves for optic nerve sheath and posterior sclera were similar throughout all strains.

Hyperelastic Model Parameters. Since the stress-strain curves with preconditioning were clearly non-linear, we applied reduced polynomial hyperelastic models that fit the averaged data well (Eqn. 1), using the parameters shown in Table 1. Polynomial order ranged from 4 to 6, as

suitable for input into ABAQUS. Coefficients of determination (R^2) for all six tissue regions exceeded 0.99.

Table 1. Reduced Polynomial Hyperelastic Model Parameters

Tissues		N	D_1	C_{10}	C_{20}	C_{30}	C_{40}	C_{50}	C_{60}
Sclera	Anterior	6	0.044	0.926	512	-42.6×10^3	226×10^4	-593×10^5	594×10^6
	Equatorial	4	0.104	0.390	252	-11.2×10^3	219×10^3	-	-
	Posterior	6	0.064	0.633	144	-6.08×10^3	153×10^3	-193×10^4	955×10^4
	Peripapillary	6	0.238	0.170	44.0	-1.43×10^3	27.6×10^3	-250×10^3	845×10^3
Optic Nerve Sheath		4	0.083	0.492	91.1	-1.78×10^3	16.3×10^3	-	-
Optic Nerve		6	0.000	0.268	16.0	-143	715	-1.73×10^3	1.59×10^3

N - polynomial degree, D_1 - [m^2/MN], C_{i0} - [MN/m^2]

Hyperelastic Properties Without Preconditioning. Tensile data for tissues that were not pre-conditioned are shown in Figure 6. These specimens were obtained from different eyes from those that underwent preconditioning. For most scleral regions and for the ON sheath, tangent modulus was significantly greater at 7% strain than at 3% strain ($P < 0.001$). Tangent modulus of anterior scleral modulus increased from 15.8±6.0 MPa at 3% stain to 32.6±11.8 MPa at 7% strain, equatorial scleral modulus increased from 8.6±4.8 MPa at 3% strain to 16.7±8.2 MP at 7% strain, and posterior scleral modulus increased from 5.4±3.1 MPa at 3% strain to 10.3±5.4 MPa at 7% strain. The tangent modulus of peripapillary sclera, however, was 4.4±5.5 MPa at 3% strain,

statistically similar to 8.0±7.5 MPa at 7% strain (P = 0.237). The tangent modulus of the ON sheath was 4.8±2.2 MPa at 3% strain and significantly a greater 11.5±5.8 MPa at 7% strain (P < 0.001). The tangent modulus of the ON was 1.7±0.9 MPa at 3% strain and 2.8±1.8 MPa at 7% strain (P = 0.016).

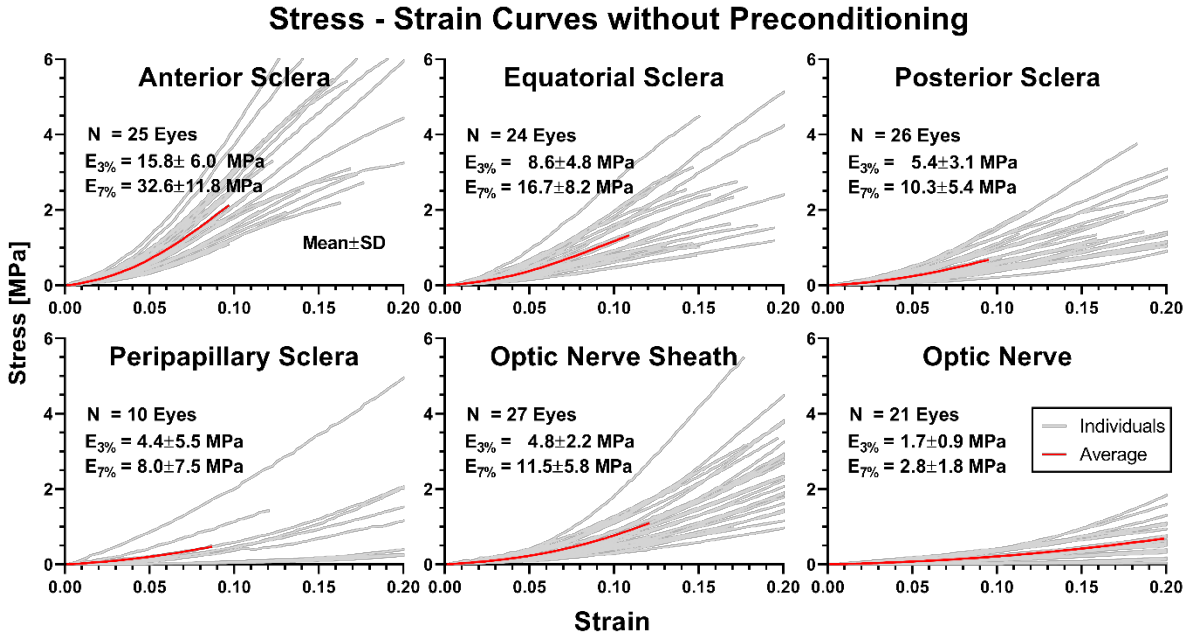

Figure 6. Tensile stress-strain relationships of ocular tissues without preconditioning. Conventions as in Figure 3.

Paired Specimen Comparison for Preconditioning. To avoid confounding by inter-eye variations, we collected multiple pairs of adjacent parallel specimens from each region of the eye; these pairs are as nearly identical as possible, except that only one of each pair was preconditioned. A special case was the ON, for which maximal length specimens from the left and right eyes of the same donor were used to secure an adequate aspect ratio for this comparison. Specimens were tested sequentially. Tensile results for specimen pairs are shown in Figure 7. Up to 2% strain, stress-strain curves with and without preconditioning were nearly identical, except for

peripapillary sclera. Above 2% strain, all tissue regions except peripapillary sclera were modestly stiffer after preconditioning, but the range of variation overlapped substantially. In contrast, peripapillary sclera did not stiffen, being insignificantly less stiff with preconditioning.

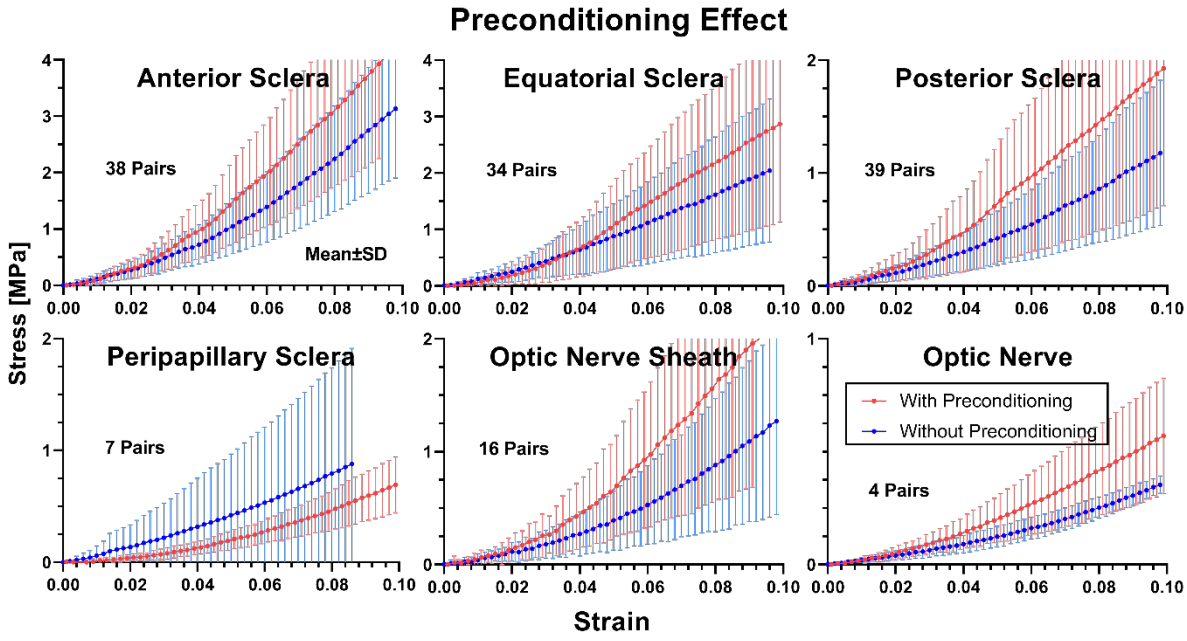

Figure 7. Effect of preconditioning on adjacent, nearly-identical samples collected as pairs. Specimens from10 eyes were used. Error bars show data ranges, and red and blue dotted curves indicate averages.

Tangent moduli at 3% and 7% strains were computed for paired specimens with and without preconditioning and subjected to paired t-testing as shown in Table 2. For anterior sclera, posterior sclera, and ON sheath, tangent moduli with preconditioning were significantly greater than without preconditioning. For peripapillary sclera and ON, these moduli were statistically similar with and without preconditioning. As shown in Figure 7, the stress-strain curves for equatorial sclera overlap up to 4.2% strain, but diverge for greater strain. Likewise, the tangent moduli of equatorial sclera at 3% strain with and without preconditioning did not significantly

differ (P = 0.059) but was significantly greater at 7% strain (P = 0.014). It should be noted, however, that the small number ON specimens available for paired testing reduced power to detect significant differences that might exist.

In Table 3 are also indicated CVs for tangent moduli of the paired tissues tested both with and without preconditioning, In general, these CV values were in the range of 0.3 – 0.7 for all tissues, and were not appreciably influenced by preconditioning. Papillary sclera was one exception, for which CV for tangent modulus at 3% strain decreased from 1.27 without to 0.42 with preconditioning, and at 7% strain from 1.08 without to 0.40 with preconditioning. The second exception was the ON, for which CV for tangent modulus at 7% strain increased from 0.07 without to 0.45 with preconditioning.

Table 2. Preconditioning Effect on Tangent Modulus of Paired Specimens

		Preconditioning	Tangent Modulus at 3% Strain [MPa]					Tangent Modulus at 7% Strain [MPa]				
			N	Mean	SD	CV	T-Test	N	Mean	SD	CV	T-Test
Sclera	Anterior	With	38	36.0	18.4	0.51	<0.001	37	57.1	23.7	0.42	<0.001
		Without		23.2	10.6	0.46			42.6	17.0	0.40	
	Equatorial	With	34	25.2	18.4	0.73	0.059	33	36.5	22.4	0.61	0.014
		Without		18.8	12.6	0.67			25.6	15.9	0.62	
	Posterior	With	39	16.6	12.8	0.77	0.003	39	24.2	15.4	0.64	0.002
		Without		9.4	5.7	0.61			15.6	8.5	0.54	
	Peripapillary	With	7	4.5	1.9	0.42	0.323	7	9.3	3.7	0.40	0.451
		Without		9.0	11.4	1.27			13.0	14.0	1.08	
Optic Nerve Sheath		With	16	15.3	10.2	0.67	0.005	16	31.3	21.0	0.67	0.011
		Without		8.3	5.4	0.65			17.4	11.5	0.66	
Optic Nerve		With	4	4.4	2.3	0.52	0.127	4	7.5	3.4	0.45	0.188
		Without		2.5	0.9	0.36			4.6	0.3	0.07	

Paired T-tests compare values with and without preconditioning.
CV – coefficient of variation. N – number of samples. SD – standard deviation.

Regional Correlations. It was of interest to determine the degree to which mechanical behavior in one region of an individual eye is reflective of behavior elsewhere in that eye. We explored this question by computing the linear correlations for 3% tangent modulus with preconditioning among all pairs of regions for all eyes. The diagonally symmetric matrix of these Pearson's r correlations has values ranging from zero (no correlation) to one (perfect correlation, as occurs on the diagonal, Figure 8). The correlation between ON sheath and anterior sclera was highest at 0.77, while ON sheath and ON had the smallest correlation at 0.12. Pairwise cross correlations among scleral regions were at least 0.58, except that correlation between peripapillary and equatorial sclera was lower at 0.32.

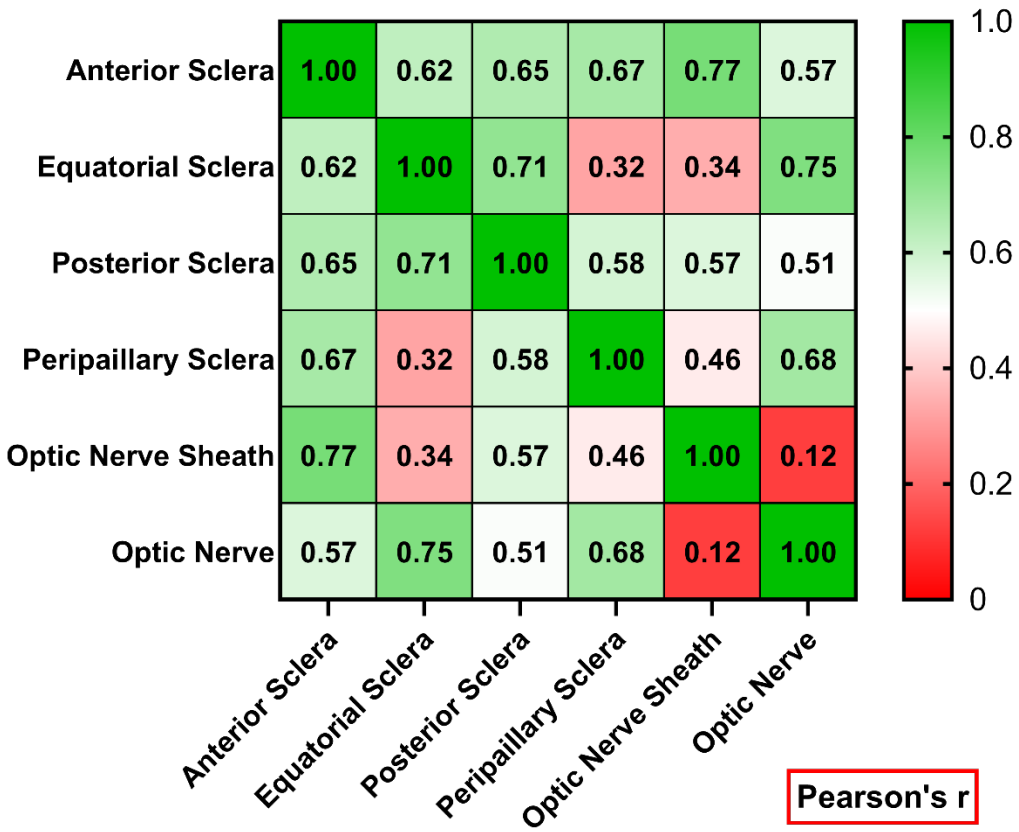

Figure 8. Regional cross correlation of tangent modulus among six ocular tissue regions at 3% strain.

Discussion

The present experimental study is consistent with prior tensile characterizations of local regions of human sclera [17, 46-49], and extends by novel reduced polynomial hyperelastic models the human scleral characterizations to additionally include the ON and its sheath. This study also quantified the effect of preconditioning on these ocular tissues and demonstrates that local variation in mechanical properties by region may differ in individual eyes such that properties in one region of a given eye do not strongly reflect properties in a different region of the same eye.

Tissue Properties. Anterior sclera must be sufficiently rigid to stabilize the eye's optics to support stable vision [50], and the present study confirms previous findings that the anterior sclera is appropriately stiffest of all scleral regions [16, 18, 46]. In any given eye, scleral stiffness tended to decrease progressively in more posterior regions, so the peripapillary sclera was the most compliant. For peripapillary sclera tested here without preconditioning, the range of stress-strain curves (Figure 4) is comparable to curves published to Spoerl *et al.* for this human tissue using similar conditions [49]. The data of Spoerl *et al.* indicated CVs for tangent modulus at 20% strain in peripapillary sclera in the range of 0.62 ~ 0.76 [49], while CVs of peripapillary sclera without preconditioning from this study were 1.08 and 1.27 at 3% and 7% strains, respectively. With preconditioning, these CVs decreased to 0.42 and 0.40, at these two strains, respectively. Variability of tangent moduli in the current study is in a comparable range to the data of Spoerl *et al.*

The human peripapillary sclera consists of an annulus of predominantly circumferentially oriented fibers encircling the optic disc, as has been implemented in computational studies [26, 28, 51-53]. The current study directly evaluated tensile properties of peripapillary sclera in the

circumferential direction. Although tangent modulus of peripapillary sclera in the 3% strain region was low, the nonlinear stiffness increased markedly with increasing strain, indicating that peripapillary sclera can absorb considerable deformational energy without failure. This high resistance to failure seems functionally appropriate because peripapillary sclera functions as a reinforcing ring protecting the sensitive and compliant ON and LC [26, 28, 51-53] against ON traction during eye movement [5, 11, 54, 55]. It is notable that preconditioning of peripapillary sclera decreased the CV of its tangent modulus appreciably, from 1.27 to 0.42 at 3% strain, and from 1.08 to 0.40 at 7% strain. The only other comparable study of human peripapillary sclera did not employ preconditioning [49].

The present study obtained novel tensile data on the human ON and its sheath. The data are comparable to measurement in bovine tissue [7]: the tangent modulus at 7% strain of human ON (6.3±3.3 MPa) was similar to that of bovine ON (5.2±0.4 MPa) although human ON sheath (23.8±15.0 MPa) was about half as stiff as bovine ON sheath (44.6±5.6 MPa). The tensile behavior of the human ON tested here was nearly identical to peripapillary sclera in the low strain region (Figure 5). It would appear advantageous for material properties at the junction of ON and peripapillary sclera to be similar to minimize stress concentration at their border. Similarly, the low strain tensile behavior of the ON sheath and posterior sclera were similar to one another, which would again minimize stress concentration at their critical juncture.

Like the mesh-like LC that constitutes the anterior terminus of the ON [56], the intraorbital ON also consists of a matrix of stiff intrinsic connective tissue supporting its compliant axonal components [34]. Although the neural tissue presumably has very low tensile strength, the embedded connective tissue makes the ON a composite structure much stronger than its axons. Shin *et al.* have modeled the interwoven structure of neural and connective tissue of the bovine ON for finite

element modeling using the rule of mixtures [7]. The tangent modulus of the ON sheath ($E_{3\%}$ = 10.0±5.8 MPa) is about 3-fold that of the ON ($E_{3\%}$ = 3.4±2.2 MPa). The stiff ON sheath seems well suited to function as a protective element for the visually critical ON.

Preconditioning. Preconditioning is believed to release residual stress in an unloaded organ [41, 57]. There have been prior studies evaluating the effects of preconditioning of bovine and porcine sclera [39] and cornea [39 58], but there has been little evaluation of the effect of preconditioning on human ocular tissues [39, 58]. As shown in Figure 3, preconditioning both shifted the stress-strain curve downward and increased its slope, the latter representing stiffening. Most of the stress-strain curves converged after two or three cycles of cyclic loading, indicating that the preconditioning protocol employed here achieved a steady state. The tangent moduli of all ocular tissues except peripapillary sclera increased modestly after preconditioning. Preconditioning of peripapillary sclera did not significantly change the tangent modulus. It may be that the anisotropic fiber orientation of peripapillary sclera [26 59-61] or its constant deformation during eye movements [62, 63] might underlie the absence of preconditioning effect.

In the human ocular tissues studied here, the chosen preconditioning protocol did not systematically reduce variability in tensile behavior but did increase tangent moduli modestly for all tissues except for peripapillary sclera, where there was no significant change. Biological tissues might behave differently depending on conditions of preconditioning [39, 64]. While it is recognized that other preconditioning protocols (e.g., different strain levels, number of loading cycles, etc.) might have produced different results, the scarcity of fresh post mortem human ocular tissues made it impractical to systematically vary preconditioning conditions in this study.

Regional Correlation. Recognizing that linear tangent moduli incompletely represent the hyperelasticity of these tissues, we nevertheless found these linear measures of stiffness useful for statistical correlations among our many measurements in a large number of human eyes. The correlation matrix in Figure 8 demonstrates that there is at the most modest correlation in elastic properties among the various regions of individual eyes. The strongest regional correlation of 0.77 was between anterior sclera and ON sheath, which indicates only 59% of the variation in ON sheath tangent modulus is statistically attributable to variation in anterior scleral modulus. This implies that a potentially available in vivo stiffness measurement of the clinically accessible anterior sclera might on average reflect about 60% of the variation in ON sheath stiffness. Correlations of tangent moduli between other regional pairs were much lower, indicating that significant regional disparities in tissue properties variously occur in individual eyes. In general, it is not possible to accurately estimate the elastic behavior of one ocular region from the value measured in another region of the same eye. Conversely, finite element modeling studies of the biomechanical effects of phenomena such as adduction traction on the ON may reasonably presume that all possible extreme values of local stiffnesses might potentially occur in any given eye.

Limitations. Tissue characterization was limited to uniaxial tensile behavior, only presenting computations of linearly elastic tangent moduli, at arbitrary low and high strain regions, for the reader's convenience in statistical comparisons and comparison to published studies [19, 28]. This presentation should not imply that we believe the mechanical properties actually to be linear. Further characterization and modeling of viscoelastic properties [27] is expected to be helpful to understand other biomechanical phenomena such as IOP and ON traction.

References

1. Demer JL, Clark RA. Translation and eccentric rotation in ocular motor modeling. *Prog Brain Res* 2019;248:117-126.
2. Chen JY, Le A, De Andrade LM, Goseki T, Demer JL. Compression of the choroid by horizontal duction. *Invest Ophthalmol Vis Sci* 2019;60:4285-4291.
3. Suh SY, Clark RA, Demer JL. Optic nerve sheath tethering in adduction occurs in esotropia and hypertropia, but not in exotropia. *Invest Ophthalmol Vis Sci* 2018;59:2899-2904.
4. Chang MY, Shin A, Park J, et al. Deformation of optic nerve head and peripapillary tissues by horizontal duction. *Am J Ophthalmol* 2017;174:85-94.
5. Demer JL. Optic nerve sheath as a novel mechanical load on the globe in ocular duction. *Invest Ophthalmol Vis Sci* 2016;57:1826-1838.
6. Quigley HA, Addicks EM, Green WR. Optic nerve damage in human glaucoma. Iii. Quantitative correlation of nerve fiber loss and visual field defect in glaucoma, ischemic neuropathy, papilledema, and toxic neuropathy. *Arch Ophthalmol* 1982;100:135-146.
7. Shin A, Yoo L, Park J, Demer JL. Finite element biomechanics of optic nerve sheath traction in adduction. *J Biomech Eng* 2017;139.
8. Lee C, Rohr J, Sass A, et al. In vivo estimation of optic nerve sheath stiffness using noninvasive mri measurements and finite element modeling. *J Mech Behav Biomed Mater* 2020;110:103924.
9. Raykin J, Forte TE, Wang R, et al. Characterization of the mechanical behavior of the optic nerve sheath and its role in spaceflight-induced ophthalmic changes. *Biomech Model Mechanobiol* 2017;16:33-43.
10. Grzybowski A, Sak J. The historical development of the concept of glaucoma. *Acta Ophthalmol* 2012;90:e494-496.
11. Demer JL, Clark RA, Suh SY, et al. Magnetic resonance imaging of optic nerve traction during adduction in primary open-angle glaucoma with normal intraocular pressure. *Invest Ophthalmol Vis Sci* 2017;58:4114-4125.
12. Wang X, Rumpel H, Lim WE, et al. Finite element analysis predicts large optic nerve head strains during horizontal eye movements. *Invest Ophthalmol Vis Sci* 2016;57:2452-2462.

13. Sibony PA. Gaze evoked deformations of the peripapillary retina in papilledema and ischemic optic neuropathy. *Invest Ophthalmol Vis Sci* 2016;57:4979-4987.
14. Li Y, Wei Q, Le A, Gawargious BA, Demer JL. Rectus extraocular muscle paths and staphylomata in high myopia. *Am J Ophthalmol* 2019;201:37-45.
15. Lee AG, Mader TH, Gibson CR, Tarver W. Space flight-associated neuro-ocular syndrome. *JAMA Ophthalmol* 2017;135:992-994.
16. Friberg TR, Lace JW. A comparison of the elastic properties of human choroid and sclera. *Exp Eye Res* 1988;47:429-436.
17. Wollensak G, Spoerl E. Collagen crosslinking of human and porcine sclera. *J Cataract Refract Surg* 2004;30:689-695.
18. Elsheikh A, Geraghty B, Alhasso D, Knappett J, Campanelli M, Rama P. Regional variation in the biomechanical properties of the human sclera. *Exp Eye Res* 2010;90:624-633.
19. Eilaghi A, Flanagan JG, Tertinegg I, Simmons CA, Wayne Brodland G, Ross Ethier C. Biaxial mechanical testing of human sclera. *J Biomech* 2010;43:1696-1701.
20. Coudrillier B, Tian J, Alexander S, Myers KM, Quigley HA, Nguyen TD. Biomechanics of the human posterior sclera: Age- and glaucoma-related changes measured using inflation testing. *Invest Ophthalmol Vis Sci* 2012;53:1714-1728.
21. Shin A, Park J, Demer JL. Opto-mechanical characterization of sclera by polarization sensitive optical coherence tomography. *J Biomech* 2018;72:173-179.
22. Carnell PH, Vito RP. A model for estimating corneal stiffness using an indenter. *J Biomech Eng* 1992;114:549-552.
23. Liu J, He X. Corneal stiffness affects iop elevation during rapid volume change in the eye. *Invest Ophthalmol Vis Sci* 2009;50:2224-2229.
24. Rahman N, O'Neill E, Irnaten M, Wallace D, O'Brien C. Corneal stiffness and collagen cross-linking proteins in glaucoma: Potential for novel therapeutic strategy. *J Ocul Pharmacol Ther* 2020.
25. Elsheikh A, Geraghty B, Rama P, Campanelli M, Meek KM. Characterization of age-related variation in corneal biomechanical properties. *J R Soc Interface* 2010;7:1475-1485.

26. Coudrillier B, Boote C, Quigley HA, Nguyen TD. Scleral anisotropy and its effects on the mechanical response of the optic nerve head. *Biomech Model Mechanobiol* 2013;12:941-963.
27. Downs JC, Suh JK, Thomas KA, Bellezza AJ, Hart RT, Burgoyne CF. Viscoelastic material properties of the peripapillary sclera in normal and early-glaucoma monkey eyes. *Invest Ophthalmol Vis Sci* 2005;46:540-546.
28. Pijanka JK, Coudrillier B, Ziegler K, et al. Quantitative mapping of collagen fiber orientation in non-glaucoma and glaucoma posterior human sclerae. *Invest Ophthalmol Vis Sci* 2012;53:5258-5270.
29. Brazile BL, Hua Y, Jan NJ, Wallace J, Gogola A, Sigal IA. Thin lamina cribrosa beams have different collagen microstructure than thick beams. *Invest Ophthalmol Vis Sci* 2018;59:4653-4661.
30. Sigal IA, Wang B, Strouthidis NG, Akagi T, Girard MJ. Recent advances in oct imaging of the lamina cribrosa. *Br J Ophthalmol* 2014;98 Suppl 2:ii34-39.
31. Midgett DE, Jefferys JL, Quigley HA, Nguyen TD. The inflation response of the human lamina cribrosa and sclera: Analysis of deformation and interaction. *Acta Biomater* 2020;106:225-241.
32. Feola AJ, Coudrillier B, Mulvihill J, et al. Deformation of the lamina cribrosa and optic nerve due to changes in cerebrospinal fluid pressure. *Invest Ophthalmol Vis Sci* 2017;58:2070-2078.
33. Coudrillier B, Campbell IC, Read AT, et al. Effects of peripapillary scleral stiffening on the deformation of the lamina cribrosa. *Invest Ophthalmol Vis Sci* 2016;57:2666-2677.
34. Karim S, Clark RA, Poukens V, Demer JL. Demonstration of systematic variation in human intraorbital optic nerve size by quantitative magnetic resonance imaging and histology. *Invest Ophthalmol Vis Sci* 2004;45:1047-1051.
35. Le A, Shin A, Park J, Poukens V, Demer JL. Bilaminar structure of the human optic nerve sheath. *Curr Eye Res* 2020;45:864-872.
36. Shin A, Park J, Le A, Poukens V, Demer JL. Bilaminar mechanics of the human optic nerve sheath. *Curr Eye Res* 2020;45:854-863.
37. Lanir Y. Mechanisms of residual stress in soft tissues. *J Biomech Eng* 2009;131:044506.

38. Lanir Y, Fung YC. Two-dimensional mechanical properties of rabbit skin. Ii. Experimental results. *J Biomech* 1974;7:171-182.
39. Tonge TK, Murienne BJ, Coudrillier B, Alexander S, Rothkopf W, Nguyen TD. Minimal preconditioning effects observed for inflation tests of planar tissues. *J Biomech Eng* 2013;135:114502.
40. Girard MJ, Downs JC, Bottlang M, Burgoyne CF, Suh JK. Peripapillary and posterior scleral mechanics--part ii: Experimental and inverse finite element characterization. *J Biomech Eng* 2009;131:051012.
41. Cheng S, Clarke EC, Bilston LE. The effects of preconditioning strain on measured tissue properties. *J Biomech* 2009;42:1360-1362.
42. Shin A, Yoo L, Demer JL. Biomechanics of superior oblique z-tenotomy. *J AAPOS* 2013;17:612-617.
43. Venkatasubramanian RT, Grassl ED, Barocas VH, Lafontaine D, Bischof JC. Effects of freezing and cryopreservation on the mechanical properties of arteries. *Ann Biomed Eng* 2006;34:823-832.
44. Ajalloueian F, Lemon G, Hilborn J, Chronakis IS, Fossum M. Bladder biomechanics and the use of scaffolds for regenerative medicine in the urinary bladder. *Nat Rev Urol* 2018;15:155-174.
45. Carew EO, Barber JE, Vesely I. Role of preconditioning and recovery time in repeated testing of aortic valve tissues: Validation through quasilinear viscoelastic theory. *Ann Biomed Eng* 2000;28:1093-1100.
46. Geraghty B, Jones SW, Rama P, Akhtar R, Elsheikh A. Age-related variations in the biomechanical properties of human sclera. *J Mech Behav Biomed Mater* 2012;16:181-191.
47. Chen K, Rowley AP, Weiland JD, Humayun MS. Elastic properties of human posterior eye. *J Biomed Mater Res A* 2014;102:2001-2007.
48. Woo SL, Kobayashi AS, Schlegel WA, Lawrence C. Nonlinear material properties of intact cornea and sclera. *Exp Eye Res* 1972;14:29-39.
49. Spoerl E, Boehm AG, Pillunat LE. The influence of various substances on the biomechanical behavior of lamina cribrosa and peripapillary sclera. *Invest Ophthalmol Vis Sci* 2005;46:1286-1290.

50. Curtin BJ. Physiopathologic aspects of scleral stress-strain. *Trans Am Ophthalmol Soc* 1969;67:417-461.
51. Campbell IC, Coudrillier B, Ross Ethier C. Biomechanics of the posterior eye: A critical role in health and disease. *J Biomech Eng* 2014;136:021005.
52. Zhang L, Albon J, Jones H, et al. Collagen microstructural factors influencing optic nerve head biomechanics. *Invest Ophthalmol Vis Sci* 2015;56:2031-2042.
53. Jones HJ, Girard MJ, White N, et al. Quantitative analysis of three-dimensional fibrillar collagen microstructure within the normal, aged and glaucomatous human optic nerve head. *J R Soc Interface* 2015;12.
54. Clark RA, Suh SY, Caprioli J, et al. Adduction-induced strain on the optic nerve in primary open-angle glaucoma at normal intraocular pressure. *Curr Eye Res* 2020;1-11.
55. Demer JL, Clark RA, Suh SY, et al. Optic nerve traction during adduction in open angle glaucoma with normal versus elevated intraocular pressure. *Curr Eye Res* 2020;45:199-210.
56. Campbell IC, Coudrillier B, Mensah J, Abel RL, Ethier CR. Automated segmentation of the lamina cribrosa using frangi's filter: A novel approach for rapid identification of tissue volume fraction and beam orientation in a trabeculated structure in the eye. *J R Soc Interface* 2015;12:20141009.
57. Eshel H, Lanir Y. Effects of strain level and proteoglycan depletion on preconditioning and viscoelastic responses of rat dorsal skin. *Ann Biomed Eng* 2001;29:164-172.
58. Boyce BL, Jones RE, Nguyen TD, Grazier JM. Stress-controlled viscoelastic tensile response of bovine cornea. *J Biomech* 2007;40:2367-2376.
59. Gogola A, Jan NJ, Lathrop KL, Sigal IA. Radial and circumferential collagen fibers are a feature of the peripapillary sclera of human, monkey, pig, cow, goat, and sheep. *Invest Ophthalmol Vis Sci* 2018;59:4763-4774.
60. Jan NJ, Lathrop K, Sigal IA. Collagen architecture of the posterior pole: High-resolution wide field of view visualization and analysis using polarized light microscopy. *Invest Ophthalmol Vis Sci* 2017;58:735-744.
61. Pijanka JK, Spang MT, Sorensen T, et al. Depth-dependent changes in collagen organization in the human peripapillary sclera. *PLoS One* 2015;10:e0118648.

62. Le A, Chen J, Lesgart M, Gawargious BA, Suh SY, Demer JL. Age-dependent deformation of the optic nerve head and peripapillary retina by horizontal duction. *Am J Ophthalmol* 2020;209:107-116.
63. Suh SY, Le A, Shin A, Park J, Demer JL. Progressive deformation of the optic nerve head and peripapillary structures by graded horizontal duction. *Invest Ophthalmol Vis Sci* 2017;58:5015-5021.
64. Kim W, Argento A, Rozsa FW, Mallett K. Constitutive behavior of ocular tissues over a range of strain rates. *J Biomech Eng* 2012;134:061002.

3.2. Opto-mechanical Characterization

The ultimate goal of human tissue characterization is to determine the tissue material property *in vivo* without destroying its shape and state. Numerous studies of *in vivo* non-destructive methods of characterization have been made using various approaches. The following study discusses a possible non-destructive characterization method using polarization sensitive-optical coherence tomography (PS-OCT) measuring the birefringence of each ocular tissue and investigates the correlation between birefringence and the material properties for each tissue. This study was published in the *Journal of Biomechanics*.

Publications included in this chapter:

3.2.1. Shin A, **Park J**, Demer JL. Opto-mechanical characterization of sclera by polarization sensitive optical coherence tomography. *J Biomech* 2018;72:173-9.

Contributions to the study: Joseph Park prepared specimens by dissecting the eye and performed uniaxial tensile experiments while measuring birefringence using polarization-sensitive optical coherence tomography. He also analyzed the data to find a correlation between stiffness and birefringence of the human ocular tissue. He made graphs and figures for the manuscript.

3.2.1. Opto-Mechanical Characterization of Sclera by Polarization Sensitive Optical Coherence Tomography

Andrew Shin[1,6], **Joseph Park**[1, 2], and Joseph L. Demer[1 ,3 ,4, 5]

[1] Department of Ophthalmology, Jules Stein Eye Institute, Los Angeles, CA, USA.
[2] Department of Bioengineering, University of California, Los Angeles, CA, USA.
[3] Biomedical Engineering Interdepartmental Program, University of California, Los Angeles, CA, USA.
[4] Neuroscience Interdepartmental Program, University of California, Los Angeles, CA, USA.
[5] Department of Neurology, University of California, Los Angeles, USA.
[6] Wellman Center for Photomedicine, Harvard Medical School & Massachusetts General Hospital, Boston, MA, USA.

Abstract

Polarization sensitive optical coherence tomography (PSOCT) is an interferometric technique sensitive to birefringence. Since mechanical loading alters the orientation of birefringent collagen fibrils, we asked if PSOCT can be used to measure local mechanical properties of sclera.

Infrared (1300 nm) PSOCT was performed during uniaxial tensile loading of fresh scleral specimens of rabbits, cows, and humans from limbal, equatorial, and peripapillary regions. Specimens from 8 human eyes were obtained. Specimens were stretched to failure at 0.01 mm/s constant rate under physiological conditions of temperature and humidity while birefringence was computed every 117 ms from cross-sectional PSOCT. Birefringence modulus (BM) was defined as the rate of birefringence change with strain, and tensile modulus (TM) as the rate of stress change between 0 and 9% strain.

In cow and rabbit, BM and TM were positively correlated with slopes of 0.17 and 0.10 GPa, and with correlation coefficients 0.63 and 0.64 ($P < 0.05$), respectively, following stress-optic coefficients 4.69, and 4.20 GPa^{-1}. In the human sclera, BM and TM were also positively correlated with slopes of 0.24 GPa for the limbal, 0.26 GPa for the equatorial, and 0.31 GPa for the peripapillary regions. Pearson correlation coefficients were significant at 0.51, 0.58, and 0.69 for each region, respectively (<0.001). Mean BM decreased proportionately to TM from the limbal to equatorial to peripapillary regions, as stress-optic coefficients were estimated as 2.19, 2.42, and 4.59 GPa^{-1}, respectively.

Since birefringence and tensile elastic moduli correlate differently in cow, rabbit, and various regions of human sclera, it might be possible to mechanically characterize the sclera *in vivo* using PSOCT.

Introduction

Biomechanical properties of various ocular tissues have been reported, including extraocular muscles (EOM)[1-3], orbital connective tissue and fat [4-6], cornea [7], and sclera [8], with sclera most widely investigated because of its putative role in myopia [9] and glaucoma [10]. Myopic scleras exhibit abnormally low stiffness and increased creep [11, 12], related to structural changes in collagen fiber bundles including lamellar arrangement and fibril diameter [13], associated with extracellular matrix remodeling [11, 14]. Expanded experimental studies have been performed using human sclera collagen cross-linking for myopia treatment [15, 16]. Several studies have reported the nonlinear viscoelastic characterization of peripapillary sclera in normal and glaucomatous eyes [17, 18] and biomechanical effect of intraocular pressure (IOP) variations had been investigated both experimentally [19-21] and by simulation [22, 23]. However, the foregoing experiments have required post-mortem methods.

Elastography is a noninvasive imaging method mapping the elastic properties of soft tissues *in vivo* [24], and can be used for diagnosing pathological changes such as edema, fibrosis, or calcification [25]. Ultrasound and magnetic resonance imaging (MRI) are widely used for imaging strain in nearly entire organs [26]. However, imaging resolution is limited to 30-70 μm for ultrasound [27] and 120 μm for MRI [28]. An alternative method, optical coherence tomography (OCT), has a superior spatial resolution of only a few microns, enabling precision OCT elastography to measure the stiffness change after corneal cross-linking [29], and map optic nerve head strain under IOP loading [30].

Polarization sensitive OCT (PSOCT) extends conventional OCT by adding polarimetry to provide birefringence information [31]. Birefringence is an optical property of anisotropic material

whereby its refractive index depends on the polarization and propagation direction of light [32]. Since most biological tissues contain birefringent constituents such as collagen, birefringence imaging has been investigated in ophthalmology [33], dermatology [34], and cardiology [35]. In ophthalmology, anterior [36] and posterior [37] ocular imaging has been widely performed to monitor pathological birefringence. PSOCT has been used to measure birefringence and validated to examine collagen organization changes in ex vivo human tissues [38-40]. It is also possible to perform PSOCT elastography, correlating birefringence with mechanical properties [41]. Correlation has been demonstrated in porcine sclera between birefringence and elastic parameters [42, 43], but this has not been studied in human. Birefringence of human sclera has been correlated with IOP *in vivo* [44], but a direct correlation with mechanical stiffness remains necessary. Therefore, the current study aimed to investigate opto-mechanical correlation in human and another mammalian sclera by capturing concurrent birefringence images during uniaxial tensile loading.

Methods

Specimen Preparation. Bovine eyes, aged 20–30 months, were obtained from local abattoir (Manning Beef LLC, Pico Rivera, CA), and New Zealand adult white rabbit (3-4 kg) eyes were obtained by tissue sharing from local research laboratories. Scleral specimens of both cow and rabbit were prepared from the globe equatorial region. Eight human globes of average age 67 ± 16 (standard deviation, SD) years, were obtained from eye banks within three days of death. Globes were wrapped in saline-soaked gauze during overnight shipment to the laboratory. Human specimens were obtained from limbal, equatorial, and peripapillary regions to examine regional differences. Each specimen was trimmed by a scalpel to a rectangular shape in random orientation

(6 x 2 mm including clamping portion) as measured using a digital caliper. An industrial OCT scanner (OCS1300SS, Thorlabs, Inc., Newton, NJ) was used to measure the cross-sectional dimensions of scleral specimens. The specimen aspect ratio was 2:1 to avoid artifact [45].

Uniaxial tensile testing with concurrent birefringence measurement. A horizontally mounted micro-tensile load cell was constructed using heavy metallic hardware, a high-speed linear motor (Ibex Engineering, Newberry Park, CA), and strain gauge permitting specimen testing in a physiological environment as described elsewhere (Figure 1) [46]. Specimens were anchored in a custom milled clamp having serrated surfaces to prevent slip. Specimens were immersed in Ringer's lactate solution before clamping and continuously kept moisturized in the tensile chamber by high humidity water vapor at a physiological temperature under feedback control by a thermocouple adjacent the specimen. Specimens were pre-loaded by 0.05N to avoid slack, and elongated at a constant rate of 0.01mm/s until failure, as tensile force was recorded by a strain gauge (LSB200, FUTEK Advanced Sensor Technology, Inc., Irvine). Specimens in each region were assumed isotropic. During tensile testing, birefringence was imaged in cross-sections using a polarization-sensitive OCT scanner (PSOCT-1300SS, Thorlabs Inc., Newton, NJ). This system incorporates fiber-based Michelson interferometry with polarized beam splitters to calculate birefringence images at 1300 nm with 12 μm axial and 25 μm transverse resolution. Images can be obtained over a 10 mm field at up to 3 mm depth, as limited by light attenuation. The imaging probe was mounted above the specimen (Figure 1) so that time-sequential, two-dimensional phase retardation images could be obtained every 117 ms as strain was progressively imposed in the tensile load cell. Control experiments were performed with internal sclera surface facing upwards toward the OCT scanner, and vice versa, but no significant difference was found. Since imaging

penetration was 3 mm to encompass entire specimen thickness, birefringence measurement was uniform over the entire specimen. Images were processed in spatial domain having a signal to noise ratio >5 dB, and temporal domain using a 1.17 s moving average filter. An additional speckle noise reduction algorithm was applied (MATLAB R2016a, The MathWorks, Inc., Natick, MA). Filtered phase retardation values were converted to birefringence Δn using the equation [32]:

$$\Delta n = \frac{\lambda_0}{2\pi L} \cdot \Gamma \qquad \text{Eq. 1}$$

where, λ_0 is vacuum wavelength of light source, L is pixel resolution, and, Γ is phase retardation, respectively. Birefringence was measured in range of 0 - 9 % strain regarded as physiological for these ocular tissues [15, 16, 47], consistent with present findings that many specimens fail at 20% strain or even less. Accordingly, tensile modulus (TM) was calculated as mean slope of the stress-strain curve from 0 - 9 % strain.

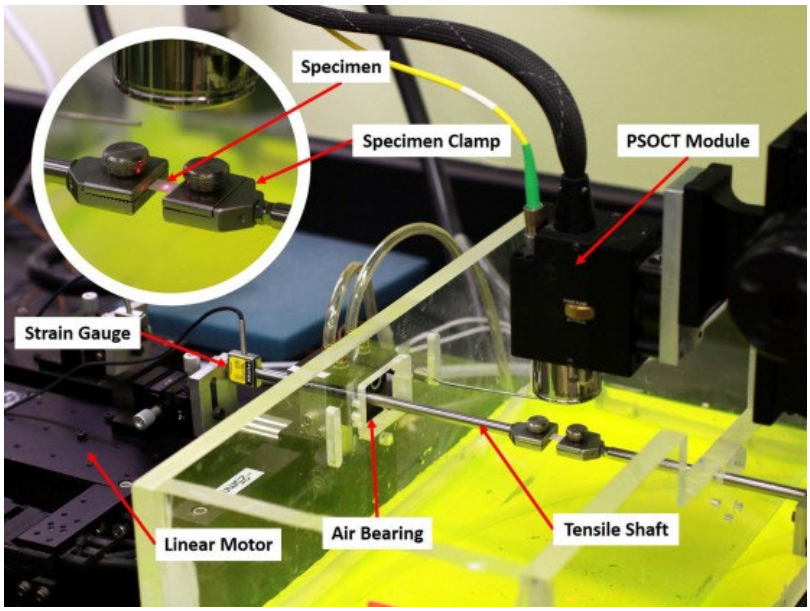

Figure 1. Tensile load cell equipped for PSOCT. A linear motor at left connected to a strain gauge transmitted tensile force through a cylindrical shaft supported by frictionless air bearing to the moveable specimen clamp. The other specimen clamp at right was anchored at right. The chamber surrounding the specimen was maintained at a physiologic temperature and saturated humidity by heated water (dyed yellow for visibility). The infrared PSOCT camera mounted above the specimen was aimed using a visible red guide laser here illuminating a paper target for illustrative purposes (inset). Actual specimen dimensions were 4 × 2 mm between the clamps. (For interpretation of the references to color in this figure legend, the reader is referred to the web version of this article.)

Avoiding cancellation by opposite local initial phase. In each cross-sectional image pixel, retardation varies from 0 to π depending on initial birefringence state caused by varying alignment of collagen fibers. Since phase retardation increases or decreases with strain in sinusoidal fashion from 0 to π radians, the direction of change in local phase retardation depends upon local starting phase (Figure 2), although physiological strain would never be great enough to demonstrate sinusoidal periodicity over multiple cycles of retardation. Over small angles, the rate of birefringence change with strain would be approximately linear. Therefore, change in birefringence cannot be determined by averaging the total value over the entire specimen cross-section, because phase cancellation would occur due to variations in local starting phase. A practical approach is to confine analysis to regions having similar starting phase retardation values.

In this study, images were divided into 16 small regions to avoid the cancellation artifact. Since entire sclera specimen was clamped and tension was applied through the whole cross-section area, we assumed uniform strain distribution within it and within any subregions.

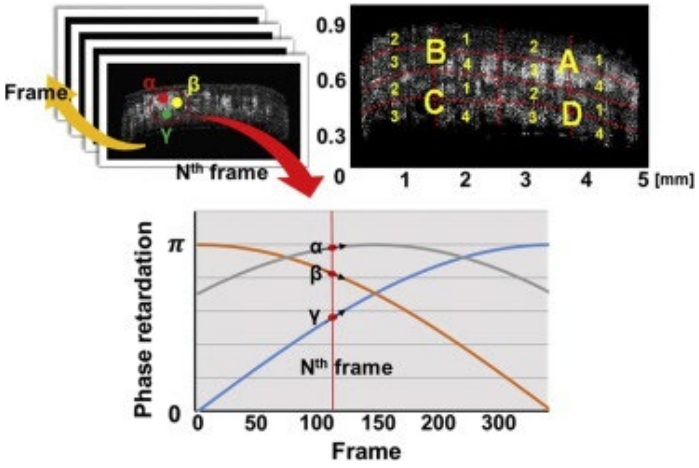

Figure 2. Avoiding cancellation due to variations in initial phase retardation. Sequential two-dimensional phase retardation images were obtained at N^{th} frame. Local regions α, β and γ have different directions of changes in birefringence causing cancellation if their birefringence moduli (BM) are simply summed through the entire specimen cross section. To minimize cancellation, each cross-section was divided into 16 regions (A1 to D4), and BM was computed for each region. There was little variation in initial phase within each of the 16 regions. Surface reflection has been removed from the Oct images.

Birefringence change was presumed to reflect altered collagen fiber orientation under load. In order to correlate opto-mechanical properties of sclera, birefringence modulus (BM) was defined as the rate of birefringence change with strain, which is analogous to the tensile modulus (TM), the rate of stress change with strain. We considered the absolute value of this rate, anticipating that its mean value would be systematically reduced by random inclusion of some initial phases with slope values near zero such as region α in Figure 2. Nevertheless, this situation would occur uniformly often for all test loadings, and so not bias the results. If BM is correlated with TM, birefringence signal can be used to infer stress. Generally, various different scleral regions exhibited different initial phases. Even though the absolute rate of change in phase with

strain might be identical in each region, a simple graph of phase retardation could exhibit a positive or negative slope depending upon initial phase, as seen in Figure 3.

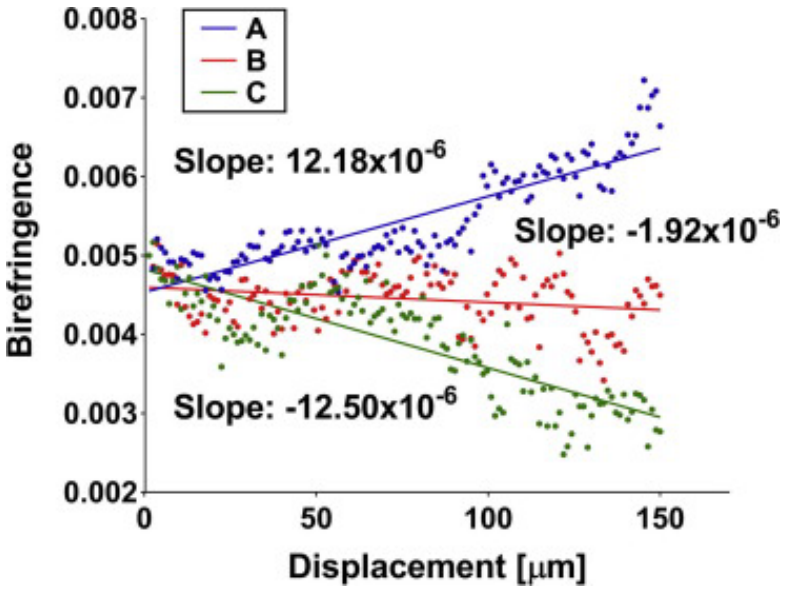

Figure 3. Different birefringence behavior of three local regions of the bovine sclera. Although regions A and C showed similar absolute birefringence changes, simple summation could result in the cancellation because of the opposite signed slopes. Each local birefringence series was shifted to start at 0.005 for comparison.

To calculate overall BM over the entire cross-sections, 16 small individual regions with uniform initial phase were analyzed first, then their absolute slope values were averaged in order to avoid cancellation by opposite-signed slopes as indicated below.

$$B = \frac{1}{16}\sum_{i=1}^{16}|b_i|, \qquad \text{Eq. 2}$$

where B, and b_i are BM of total, and local regions, respectively.

Modified stress-optic law with birefringence and tensile modulus. The stress-optic law [48] in photoelasticity characterizing the relation between optical phase retardation and mechanical stress is given by the equation:

$$\Gamma = \frac{2\pi t}{\lambda} C(\sigma_1 - \sigma_2), \qquad \text{Eq. 3}$$

where, Γ is induced retardation, t is specimen thickness, and λ is vacuum wavelength, C is stress-optic coefficient, and σ_1 & σ_2 are the first and second principal stresses, respectively. Recognizing that phase retardation can be expressed as birefringence term using Eq. 1, and uniaxial tensile stress was applied to sclera tissue, Eq.3 can be rearranged as shown in Eq. 4 for uniaxial tension:

$$\Delta n = C \cdot \sigma, \qquad \text{Eq. 4}$$

where Δn is birefringence, and C is stress-optic coefficient, and σ is uniaxial tensile stress, respectively. In the linear regime, Eq. 4 can be divided by strain (ε), and the stress-optic coefficient can be expressed in terms of BM and TM as shown in Eq. 5:

$$\mathrm{C} = \mathrm{BM} \,/\, TM \ , \qquad \text{Eq. 5,}$$

where, BM = $\delta\Delta n/_{\delta\varepsilon}$, and TM = $\delta\sigma/_{\delta\varepsilon}$.

Results

Correlated birefringence and tensile modulus. For cow and rabbit sclera, simultaneously measured BM and TM pairs were plotted for analysis (Figure 4), and the Pearson correlation was computed (GraphPad Software, Inc., La Jolla, CA). Both cow and rabbit scleras exhibited statistically significant positive correlation between BM and TM (Table 1). The mean (± SEM)

TM of bovine sclera was larger (19.0 ± 2.3 MPa) than for rabbit (13.0 ± 1.0 MPa), while bovine BM was also larger (83 ± 8x10^{-3} vs 56 ± 7x10^{-3}). Corresponding stress-optic coefficients of bovine and rabbit sclera were 4.69 ± 0.44 and 4.20 ± 0.43 GPa^{-1}, which do not significantly differ.

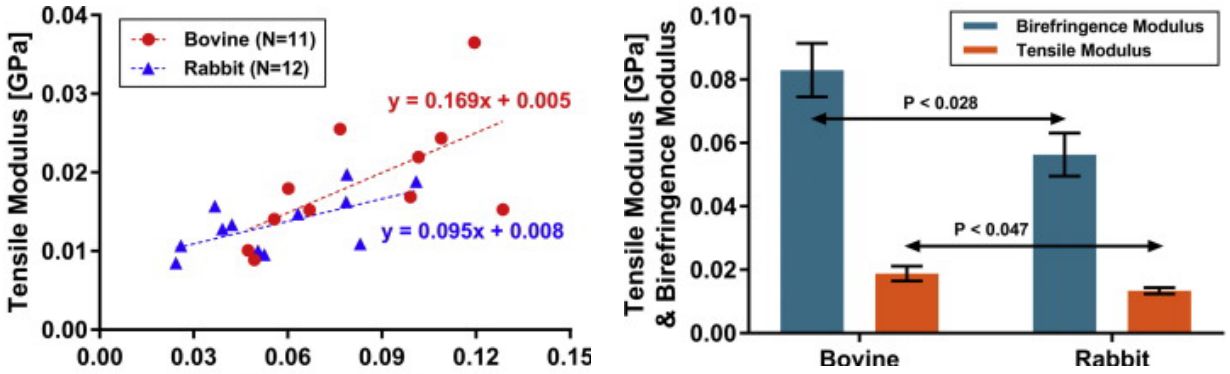

Figure 4. Correlation between birefringence and tensile modulus in bovine and rabbit sclera. Stress-optic coefficients were 4.69, and 4.20 GPa^{-1}, respectively.

The foregoing procedure was employed for human scleral specimens. For the three different human scleral regions, BM and TM demonstrated moderate to strong positive correlation (Table 2). Mean values of BM and TM were calculated in each region (Figure 5). In human, TM decreased from 26 ± 1 MPa in the limbal to 18±1 MPa in equatorial, and to 8.3 ± 0.8 MPa in the peripapillary region, as BM also decreased from 54 ± 3x10^{-3} to 39 ± 2x10^{-3}, and to 28 ± 2x10^{-3}, respectively. Corresponding stress-optic coefficients were 2.19 ± 0.11, 2.42 ± 0.14, and 4.59 ± 0.54 GPa^{-1}, respectively.

Table 1. Correlation between birefringence (BM) and tensile (TM) modulus in bovine and rabbit sclera. Both bovine and rabbit exhibited statically significant positive correlation.

	Bovine	Rabbit
Pearson r	0.6299	0.6346
P value	0.0378	0.0267

Table 2. Correlation between birefringence and tensile modulus in human sclera

	Limbal	Equatorial	Peripapillary
Pearson r	0.5117	0.5757	0.6943
P value	0.0002	<0.0001	<0.0001

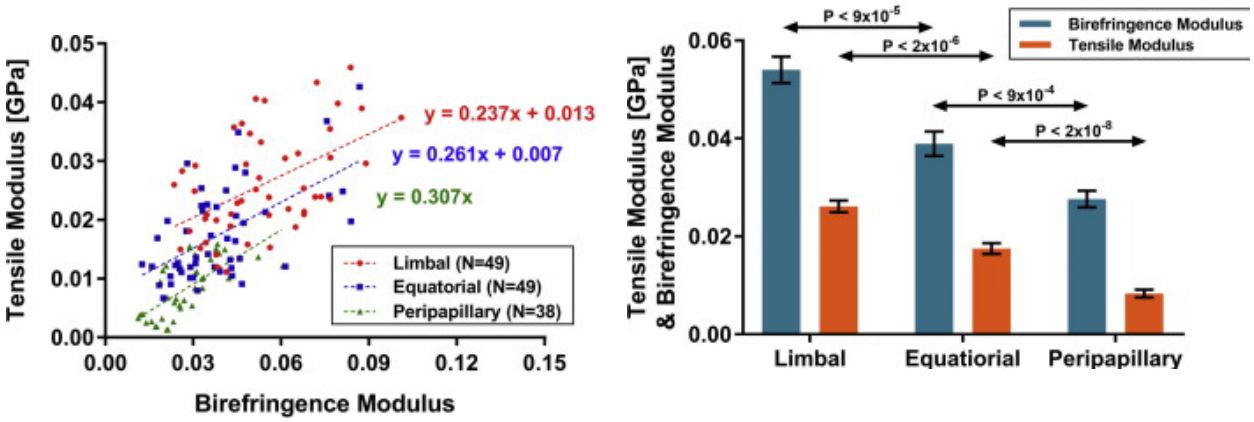

Figure 5. Correlation between birefringence and tensile modulus in human sclera. Linear regressions illustrate positive correlation in all three regions, as mean BM and TM progressively decreased from limbal to peripapillary region. Estimated stress-optic coefficients are 2.19, 2.42, and 4.59 GPa^{-1}, respectively.

Opto-mechanical behavior of human sclera. Optical birefringence and mechanical stress values were paired for specimens of human sclera at matching values of strain, and are plotted in Figure 6 to infer strain for three scleral regions. Figure 6 illustrates the opto-mechanical behavior of each

human scleral region with linear regression relating birefringence with stress. The peripapillary region (0.38 GPa) exhibited different opto-mechanical behavior from limbal and equatorial regions (0.48, and 0.45 GPa). These slopes may be considered as inverse stress-optic coefficients.

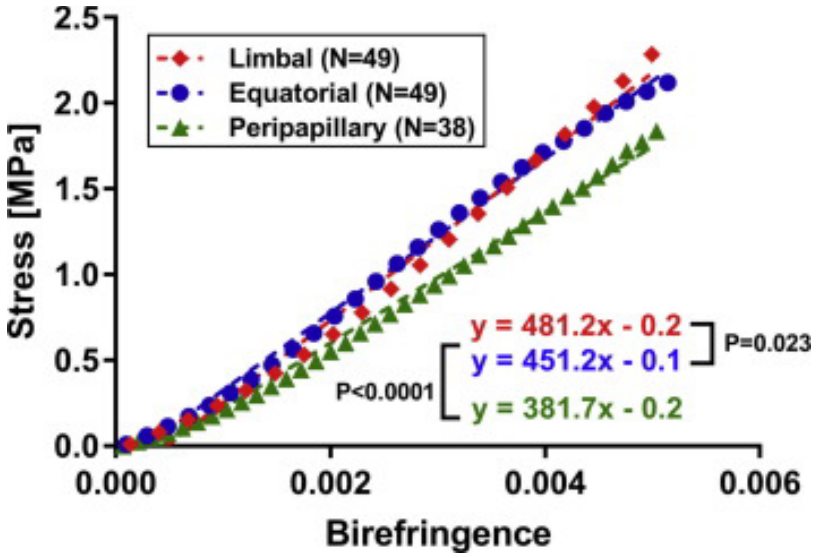

Figure 6. Correlation of birefringence and stress in human sclera. Nonlinear stress values were paired with corresponding birefringence values based on matching strain. The slope of the relationship in the peripapillary region (green triangles) is highly significantly different from other two regions ($P < 0.0001$), corresponding to differing inverse stress-optic coefficients. (For interpretation of the references to colour in this figure legend, the reader is referred to the web version of this article.)

Discussion

The current study demonstrates that the rate of birefringence change correlates with the tensile modulus of sclera in humans, cows, and rabbits within the 0 – 9% range of strain that is physiologic for this relatively rigid ocular tissue. Birefringence (BM) and tensile modulus (TM) are positively correlated, meaning that when the sclera is stiffer, the BM is greater. Moreover, regional variation in BM and TM in human limbal, equatorial, and peripapillary sclera is also correlated (Figure 5): as sclera stiffness decreases from anterior to posterior, BM decreases accordingly. Stress-optic coefficients calculated from these BM and TM values can be regarded as intrinsic opto-mechanical properties of each tissue. Although these values are computed under linear and isotropic assumptions, the stress-optic coefficients are similar for perilimbal and equatorial sclera at 2.19 GPa^{-1} and 2.42 GPa^{-1} having almost identical opto-mechanical properties that in turn differ significantly from peripapillary sclera at 4.59 GPa^{-1}. Unlike the other regions, the narrow peripapillary scleral ring immediately adjacent to the optic nerve has anisotropic circumferential collagen fiber direction as demonstrated by non-linear microscopy [49, 50], small-angle light scattering [51, 52], and wide-angle x-ray scattering [53, 54]. Peripheral to the circumferential scleral ring, scleral fibers have a wide range of criss-crossing orientations likely to result in grossly isotropic tensile properties. Since the current study did not include the peripapillary ring tissue, which is too small to be loaded outside the clamps in the current experiment, the current assumption of tissue isotropy remains initially reasonable. Since the current study performed uniaxial tensile testing in arbitrary directions that would not have detected possible tissue anisotropy, further study would be required to detect possible anisotropy relative to circumferential and radial directions. Elevation of IOP in whole or half globes might be performed to study

birefringence under loading conditions, although interpretation of such a study would probably require assumptions about uniformity and isotropy of scleral thickness and mechanical properties.

Recently, an MRI study demonstrated that the nerve and its sheath become taut during adduction eye movement [55]. An OCT study showed that significant deformation occurred in temporal optic nerve head region during adduction, but not abduction [56]. The current opto-mechanical correlation study could be applied to extend these *in vivo* studies by providing inferred peripapillary stress from OCT birefringence measurement, providing intrinsic mechanical characterization for individual tissues. Since the current study employed an industrial PSOCT scanner and not a clinically approved instrument, further development would be necessary for studies in living humans. Currently, OCT is extensively utilized in ophthalmology to diagnose glaucoma and retinal disorders by structural analysis [57, 58]. There already exist clinical OCT scanners that are polarization-sensitive and used to diagnose pathologic tissues from birefringence signal changes in the retinal nerve fiber layer (RNFL) [37], choroid [59], and posterior sclera [60]. Since the current study characterized the birefringence-stress relation in human peripapillary sclera, this correlation might be directly applied *in vivo* using clinical PSOCT to infer peripapillary stress both in normal and abnormal sclera tissues.

Once the stress-optic coefficient of tissue is established in normal subjects, it could be used as a reference for abnormality. Direct correlation between scleral birefringence and stress might be utilized for *in vivo* diagnosis of tissue abnormality, and local anatomic correlation. One possible application might be the longitudinal, *in vivo* study of peripapillary atrophy that frequently occurs on the temporal side [61] and that has been proposed to be due to local strain resulting from optic nerve sheath tethering during adduction eye rotation [55]. Peripapillary atrophy frequently occurs with glaucoma [62, 63], and is progressive with age [64], myopia [65], and glaucoma progression [66-69], yet

its causation and potential clinical significance remain obscure. If birefringence change were found to be spatially correlated with existing and especially progressing peripapillary atrophy on longitudinal study, this might suggest a causative relationship.

The current study is subject to some limitations. First, even analysis of 16 local regions of each OCT cross-section to minimize initial phase cancellation effects may nevertheless have permitted some since the local regions are still large relative to individual collagen fiber bundles. Even finer local analysis might further reduce phase cancellation effects. Additional factors besides mechanical loading might affect birefringence, including structural [70] or composition [71] changes in sclera tissue associated with aging. Those changes substantially alter scleral stiffness [72, 73], but might also differently affect birefringence. Specific studies of possible aging effects are probably warranted. The current technique avoided experimental artifact that might have arisen from variation in tissue hydration during testing. The 0 – 9% strain range employed here is low compared with physiologic strains experienced by, for example, skin or aortic wall; however, since ocular dimensions must remain highly precise to enable adequate visual performance, it is understandable that the ocular sclera does not experience substantially higher strains than about 10% under physiological conditions. A recent study with terahertz (THz) spectroscopy reported that differences in water content influence the accuracy of calculated optical properties since THz radiation is strongly absorbed by water [74]. To avoid the possibility that variations in scleral water content might similarly influence birefringence, we studied fresh tissue under physiological conditions with regulated tissue hydration and temperature throughout each loading, eliminating hydration variation a confounding factor.

References

1. Quaia C, Ying HS, Optican LM. The viscoelastic properties of passive eye muscle in primates. Ii: Testing the quasi-linear theory. *PLoS One* 2009;4:e6480.

2. Yoo L, Kim H, Gupta V, Demer JL. Quasilinear viscoelastic behavior of bovine extraocular muscle tissue. *Invest Ophthalmol Vis Sci* 2009;50:3721-3728.

3. Shin A, Yoo L, Demer JL. Independent active contraction of extraocular muscle compartments. *Invest Ophthalmol Vis Sci* 2015;56:199-206.

4. Schoemaker I, Hoefnagel PP, Mastenbroek TJ, et al. Elasticity, viscosity, and deformation of orbital fat. *Invest Ophthalmol Vis Sci* 2006;47:4819-4826.

5. Chen K, Weiland JD. Mechanical properties of orbital fat and its encapsulating connective tissue. *J Biomech Eng* 2011;133:064505.

6. Yoo L, Gupta V, Lee C, Kavehpore P, Demer JL. Viscoelastic properties of bovine orbital connective tissue and fat: Constitutive models. *Biomech Model Mechan* 2011;10:901-914.

7. Yoo L, Reed J, Gimzewski JK, Demer JL. Mechanical interferometry imaging for creep modeling of the cornea. *Invest Ophthalmol Vis Sci* 2011;52:8420-8424.

8. Yoo L, Reed J, Shin A, et al. Characterization of ocular tissues using micro-indentation and hertzian viscoelastic models. *Invest Ophthalmol Vis Sci* 2011;52:3475-3482.

9. McBrien NA, Gentle A. Role of the sclera in the development and pathological complications of myopia. *Prog Retin Eye Res* 2003;22:307-338.

10. Burgoyne CF, Crawford Downs J, Bellezza AJ, Francis Suh JK, Hart RT. The optic nerve head as a biomechanical structure: A new paradigm for understanding the role of iop-related stress and strain in the pathophysiology of glaucomatous optic nerve head damage. *Prog Retin Eye Res* 2005;24:39-73.

11. McBrien NA, Jobling AI, Gentle A. Biomechanics of the sclera in myopia: Extracellular and cellular factors. *Optom Vis Sci* 2009;86:E23-E30.

12. Phillips JR, Khalaj M, McBrien NA. Induced myopia associated with increased scleral creep in chick and tree shrew eyes. *Invest Ophthalmol Vis Sci* 2000;41:2028-2034.

13. Curtin BJ, Iwamoto T, Renaldo DP. Normal and staphylomatous sclera of high myopia: An electron microscopic study. *Arch Ophthalmol* 1979;97:912-915.

14. Summers Rada JA, Shelton S, Norton TT. The sclera and myopia. *Exp Eye Res* 2006;82:185-200.

15. Wang M, Zhang F, Qian X, Zhao X. Regional biomechanical properties of human sclera after cross-linking by riboflavin/ultraviolet a. *J Refract Surg* 2012;28:723-728.

16. Wollensak G, Spoerl E. Collagen crosslinking of human and porcine sclera. *Journal of Cataract & Refractive Surgery* 2004;30:689-695.

17. Downs JC, Suh JK, Thomas KA, Bellezza AJ, Burgoyne CF, Hart RT. Viscoelastic characterization of peripapillary sclera: Material properties by quadrant in rabbit and monkey eyes. *J Biomech Eng* 2003;125:124-131.

18. Downs JC, Suh JK, Thomas KA, Bellezza AJ, Hart RT, Burgoyne CF. Viscoelastic material properties of the peripapillary sclera in normal and early-glaucoma monkey eyes. *Invest Ophthalmol Vis Sci* 2005;46:540-546.

19. Girard MJA, Suh JKF, Bottlang M, Burgoyne CF, Downs JC. Scleral biomechanics in the aging monkey eye. *Invest Ophthalmol Vis Sci* 2009;50:5226-5237.

20. Nguyen TD, Ethier CR. Biomechanical assessment in models of glaucomatous optic neuropathy. *Exp Eye Res* 2015;141:125-138.

21. Fazio MA, Grytz R, Bruno L, et al. Regional variations in mechanical strain in the posterior human sclera. *Invest Ophthalmol Vis Sci* 2012;53:5326-5333.

22. Sigal IA, Flanagan JG, Tertinegg I, Ethier CR. Finite element modeling of optic nerve head biomechanics. *Invest Ophthalmol Vis Sci* 2004;45:4378-4387.

23. Sigal IA, Ethier CR. Biomechanics of the optic nerve head. *Exp Eye Res* 2009;88:799-807.

24. Ophir J, Céspedes I, Ponnekanti H, Yazdi Y, Li X. Elastography: A quantitative method for imaging the elasticity of biological tissues. *Ultrasonic Imaging* 1991;13:111-134.

25. Gambichler T, Moussa G, Sand M, Sand D, Altmeyer P, Hoffmann K. Applications of optical coherence tomography in dermatology. *J Dermatol Sci* 2005;40:85-94.

26. Sarvazyan A, Hall TJ, Urban MW, Fatemi M, Aglyamov SR, Garra BS. An overview of elastography - an emerging branch of medical imaging. *Curr Med Imaging Rev* 2011;7:255-282.

27. Foster FS, Pavlin CJ, Harasiewicz KA, Christopher DA, Turnbull DH. Advances in ultrasound biomicroscopy. *Ultrasound Med Biol* 2000;26:1-27.

28. Thali MJ, Dirnhofer R, Becker R, Oliver W, Potter K. Is 'virtual histology' the next step after the 'virtual autopsy'? Magnetic resonance microscopy in forensic medicine. *Magn Reson Imaging* 2004;22:1131-1138.

29. Li J, Han Z, Singh M, Twa MD, Larin KV. Differentiating untreated and cross-linked porcine corneas of the same measured stiffness with optical coherence elastography. *J Biomed Opt* 2014;19:110502.

30. Girard MJA, Beotra MR, Chin KS, et al. In vivo 3-dimensional strain mapping of the optic nerve head following intraocular pressure lowering by trabeculectomy. *Ophthalmology* 2016;123:1190-1200.

31. de Boer JF, Milner TE, van Gemert MJC, Nelson JS. Two-dimensional birefringence imaging in biological tissue by polarization-sensitive optical coherence tomography. *Opt Lett* 1997;22:934-936.

32. Hecht E. *Optics*. 4th ed: Addison-Wesley; 2001.

33. Cense B, Chen TC, Park BH, Pierce MC, de Boer JF. Thickness and birefringence of healthy retinal nerve fiber layer tissue measured with polarization-sensitive optical coherence tomography. *Invest Ophthalmol Vis Sci* 2004;45:2606-2612.

34. Sakai S, Nakagawa N, Yamanari M, Miyazawa A, Yasuno Y, Matsumoto M. Relationship between dermal birefringence and the skin surface roughness of photoaged human skin. *J Biomed Opt* 2009;14:044032-044032-044038.

35. Fan C, Yao G. Imaging myocardial fiber orientation using polarization sensitive optical coherence tomography. *Biomed Opt Express* 2013;4:460-465.

36. Kasaragod D, Fukuda S, Ueno Y, Hoshi S, Oshika T, Yasuno Y. Objective evaluation of functionality of filtering bleb based on polarization-sensitive optical coherence tomography. *Invest Ophthalmol Vis Sci* 2016;57:2305-2310.

37. Zotter S, Pircher M, Torzicky T, et al. Large-field high-speed polarization sensitive spectral domain oct and its applications in ophthalmology. *Biomed Opt Express* 2012;3:2720-2732.

38. Kemp NJ, Zaatari HN, Park J, Rylander Iii HG, Milner TE. Form-biattenuance in fibrous tissues measured with polarization-sensitive optical coherence tomography (ps-oct). *Opt Express* 2005;13:4611-4628.

39. Nadkarni SK, Pierce MC, Park BH, et al. Measurement of collagen and smooth muscle cell content in atherosclerotic plaques using polarization-sensitive optical coherence tomography. *J Am Coll Cardiol* 2007;49:1474-1481.

40. Kuo W-C, Chou N-K, Chou C, et al. Polarization-sensitive optical coherence tomography for imaging human atherosclerosis. *Appl Opt* 2007;46:2520-2527.

41. Wiesauer K, Dufau ADS, Götzinger E, Pircher M, Hitzenberger CK, Stifter D. Non-destructive quantification of internal stress in polymer materials by polarisation sensitive optical coherence tomography. *Acta Materialia* 2005;53:2785-2791.

42. Yamanari M, Ishii K, Fukuda S, et al. Optical rheology of porcine sclera by birefringence imaging. *PLoS One* 2012;7:e44026.

43. Nagase S, Yamanari M, Tanaka R, et al. Anisotropic alteration of scleral birefringence to uniaxial mechanical strain. *PLoS One* 2013;8:e58716.

44. Yamanari M, Nagase S, Fukuda S, et al. Scleral birefringence as measured by polarization-sensitive optical coherence tomography and ocular biometric parameters of human eyes in vivo. *Biomed Opt Express* 2014;5:1391-1402.

45. Carew EO, Patel J, Garg A, Houghtaling P, Blackstone E, Vesely I. Effect of specimen size and aspect ratio on the tensile properties of porcine aortic valve tissues. *Ann Biomed Eng* 2003;31:526-535.

46. Shin A, Yoo L, Demer JL. Biomechanics of superior oblique z-tenotomy. *J AAPOS* 2013;17:612-617.

47. Scarcelli G, Pineda R, Yun SH. Brillouin optical microscopy for corneal biomechanics. *Invest Ophthalmol Vis Sci* 2012;53:185-190.

48. Dally JW, Riley WF. *Experimental Stress Analysis, 3rd edition*: McGraw-Hill Inc. New York; 1991.

49. Winkler M, Jester B, Nien-Shy C, et al. High resolution three-dimensional reconstruction of the collagenous matrix of the human optic nerve head. *Brain research bulletin* 2010;81:339-348.

50. Pijanka JK, Coudrillier B, Ziegler K, et al. Quantitative mapping of collagen fiber orientation in non-glaucoma and glaucoma posterior human sclerae. *Invest Ophthalmol Vis Sci* 2012;53:5258-5270.

51. Girard MJ, Dahlmann-Noor A, Rayapureddi S, et al. Quantitative mapping of scleral fiber orientation in normal rat eyes. *Invest Ophthalmol Vis Sci* 2011;52:9684-9693.

52. Danford FL, Yan D, Dreier RA, Cahir TM, Girkin CA, Vande Geest JP. Differences in the region- and depth-dependent microstructural organization in normal versus glaucomatous human posterior sclerae. *Invest Ophthalmol Vis Sci* 2013;54:7922-7932.

53. Pijanka JK, Abass A, Sorensen T, Elsheikh A, Boote C. A wide-angle x-ray fibre diffraction method for quantifying collagen orientation across large tissue areas: Application to the human eyeball coat. *J Appl Crystallogr* 2013;46:1481-1489.

54. Pijanka JK, Spang MT, Sorensen T, et al. Depth-dependent changes in collagen organization in the human peripapillary sclera. *PLoS One* 2015;10:e0118648.

55. Demer JL. Optic nerve sheath as a novel mechanical load on the globe in ocular duction. *Invest Ophthalmol Vis Sci* 2016;57:1826-1838.

56. Chang MY, Shin A, Park J, et al. Deformation of optic nerve head and peripapillary tissues by horizontal duction. *Am J Ophthalmol* 2017;174:85-94.

57. Mwanza J-C, Oakley JD, Budenz DL, Anderson DR. Ability of cirrus hd-oct optic nerve head parameters to discriminate normal from glaucomatous eyes. *Ophthalmology* 2011;118:241-248.e241.

58. Sung KR, Wollstein G, Kim NR, et al. Macula assessment using optical coherence tomography for glaucoma diagnosis. *Br J Ophthalmol* 2012;96:1452-1455.

59. Pircher M, Hitzenberger CK, Schmidt-Erfurth U. Polarization sensitive optical coherence tomography in the human eye. *Prog Retin Eye Res* 2011;30:431-451.

60. Sugiyama S, Hong Y-J, Kasaragod D, et al. Birefringence imaging of posterior eye by multi-functional jones matrix optical coherence tomography. *Biomed Opt Express* 2015;6:4951-4974.

61. Jonas JB, Nguyen XN, Gusek GC, Naumann GO. Parapapillary chorioretinal atrophy in normal and glaucoma eyes. I. Morphometric data. *Invest Ophthalmol Vis Sci* 1989;30:908-918.

62. Jonas JB, Martus P, Horn FK, Junemann A, Korth M, Budde WM. Predictive factors of the optic nerve head for development or progression of glaucomatous visual field loss. *Invest Ophthalmol Vis Sci* 2004;45:2613-2618.

63. Xu L, Wang Y, Yang H, Jonas JB. Differences in parapapillary atrophy between glaucomatous and normal eyes: The beijing eye study. *Am J Ophthalmol* 2007;144:541-546.

64. Savatovsky E, Mwanza JC, Budenz DL, et al. Longitudinal changes in peripapillary atrophy in the ocular hypertension treatment study: A case-control assessment. *Ophthalmology* 2015;122:79-86.

65. Nakazawa M, Kurotaki J, Ruike H. Longterm findings in peripapillary crescent formation in eyes with mild or moderate myopia. *Acta ophthalmologica* 2008;86:626-629.

66. Uhm KB, Lee DY, Kim JT, Hong C. Peripapillary atrophy in normal and primary open-angle glaucoma. *Korean J Ophthalmol : KJO* 1998;12:37-50.

67. Rockwood EJ, Anderson DR. Acquired peripapillary changes and progression in glaucoma. *Graefes Arch Clin Exp Ophthalmol* 1988;226:510-515.

68. Budde WM, Jonas JB. Enlargement of parapapillary atrophy in follow-up of chronic open-angle glaucoma. *Am J Ophthalmol* 2004;137:646-654.

69. Uchida H, Ugurlu S, Caprioli J. Increasing peripapillary atrophy is associated with progressive glaucoma. *Ophthalmology* 1998;105:1541-1545.

70. Malik NS, Moss SJ, Ahmed N, Furth AJ, Wall RS, Meek KM. Ageing of the human corneal stroma: Structural and biochemical changes. *Biochim Biophys Acta, Mol Basis Dis* 1992;1138:222-228.

71. Rada JA, Achen VR, Penugonda S, Schmidt RW, Mount BA. Proteoglycan composition in the human sclera during growth and aging. *Invest Ophthalmol Vis Sci* 2000;41:1639-1648.

72. Geraghty B, Jones SW, Rama P, Akhtar R, Elsheikh A. Age-related variations in the biomechanical properties of human sclera. *J Mech Behav Biomed Mater* 2012;16:181-191.

73. Grytz R, Fazio MA, Libertiaux V, et al. Age- and race-related differences in human scleral material properties. *Invest Ophthalmol Vis Sci* 2014;55:8163-8172.

74. Png GM, Choi JW, Ng BW, Mickan SP, Abbott D, Zhang XC. The impact of hydration changes in fresh bio-tissue on thz spectroscopic measurements. *Phys Med Biol* 2008;53:3501-3517.

CHAPTER 4. OPTIC NERVE TETHERING

4.1. The Concept of Optic Nerve Tethering

The main concept of ON tethering can be understood from the anatomical characteristics of the eye in its socket. As described in chapter 2, the ON head is located 3.75 mm nasal to the straight-ahead visual axis, and the optic canal, the tunnel through which the ON exits the orbit, is located on the nasal side of the orbit. Abduction (rotating eye away from the midline of the head) requires the shortest, central gaze intermediate, and adduction (rotating eye towards the midline of the head) the longest distance from the optic canal to the ON head. Therefore, while the ON typically has considerable length redundancy during abduction, in most people this redundancy is exhausted during adduction when the ON is pulled taut and straight. Importantly, exhausted redundancy of ON length in adduction occurs in nearly all people, not just patients with ON disease[1], so this phenomenon is unlikely to be pathological in the absence of further contributing factors that we also investigate. We consider tethering to occur when ON redundancy is exhausted.

4.2. Repetitive Daily Eye Movements

If the eye rotation rarely occurs, applying traction to the ON head during adduction will not result in ON damage. However, humans rotate their eyes more intensively and more often than you might think. In general, average healthy adults rotate their eyes about 3 times per second[2]. Also, taking into account the eye movements that occur during sleep[3], the eye rotates about 183,000 times a day[4]. The maximum range of horizontal eye movement is approximately 45º in

adduction and 44º in abduction[5]. The vestibulo-ocular reflex, an automatically generated counter-eye rotation during head rotation, is coordinated with large saccades during head rotation, typically involving an average eye movement of about 30º [6-8] and around 400 º/sec[9]. We move our heads a great deal during natural activities.

4.3. Hypothesis Formulation

The hypothesis of ON tethering arose because of careful observation of high-resolution surface coil MRI of the orbits during eye rotation[6, 10, 11]. MRI investigations have shown that the ON becomes straightened when the eye adducts by a relatively large but not maximal angle, and usually slacken when the eye abducts[6, 10, 11]. By tracking the ON path and globe center using MRI, Demer *et al*. have demonstrated that the straightened ON is associated with posterior retraction of the globe during adduction in patients with NTG[6, 10].

4.4. Imaging Observations

The optical coherence tomography (OCT) scanner is an imaging device based on low coherence interferometry using relatively long-wavelength (infrared) light to capture high-resolution images. The scanner is widely used in ophthalmology to diagnose ocular disorders such as macular retinal disease and glaucoma. Chang *et al*. performed an OCT experiment in which subjects rotated their heads while looking straight into a clinical spectral-domain OCT scanner. This study demonstrated tilts of the optic disc during eye rotation by measuring anterior-posterior displacements of Bruch's membrane that supports the retinal pigment epithelium[12]. Chang *et al*.

found an optic disc tilt with respect to the nasal and temporal edges of Bruch's membrane which appears as a bright layer in OCT. However, the experiment did not account for the 17° offset of the internal target fixation of the OCT scanner. In the following OCT study, Suh *et al*. considered the offset of the target inside the machine to accurately reference gaze direction relative to the cranial straight-ahead direction as they conducted an experiment using an OCT mounted on a yaw gimbal [1]. Deformation of the optic disc during adduction was significantly larger than during the abduction, particularly for adduction beyond a 26° gaze angle threshold[1] at which the ON tethering was inferred to begin. Suh *et al*. showed through MRI measurements that ON tethering occurs in patients with esotropia (eye misaligned inward) and hypetropia (vertically misaligned), but not in exotropia (eye misaligned outward)[13]. Beyond the OCT studies, scanning laser ophthalmoscopy (SLO) was also employed to explore ON tethering. Unlike the transverse images of OCT, SLO acquires frontal images of the ON head. By tracking the vascular landmarks on and around the ON head, Le *et al.* have shown that adduction deforms the ON head and peripapillary sclera more than abduction, and more so in younger than older people[14].

4.5. Finite Element Analysis

Finite element analysis (FEA) is a numerical method that calculates how individual parts of an object react to physical effects such as force, vibration, and heat. It is a popular contemporary method for evaluating engineering problems such as car crash tests, bridge column endurance tests, airplane fatigue tests, and so on. In a mathematical way, the complex physical problem can be expressed as partial differential equations or integral equations. Rather than solving the problem as a whole system, FEA subdivides a large object into small parts called finite elements and forms

a mesh that is made up of a combination of finite elements containing nodes that are constrained to contact conditions. Subdivision of the problem provides a detailed depiction of complex models, versatility in material properties, and easy representation of total solution[15]. After solving the behavior of each of many elements, FEA adds all the individual behaviors so that the computer can predict the behavior of the object.

After performing optical measurements, we next used FEA to evaluate the ON tethering hypothesis. Optical measurements represent a valuable way to provide quality data, but imaging only displays a phenomenon, not its cause. To investigate possible causes of ON tethering, FEM was employed. As of the first FEA study of the Demer group, Shin *et al*. designed an adduction eye model having a straightened ON, and simulated the effect of ON tethering by incremental rotation in the same direction[16]. Although the model was simple, adducted an incremental 6°, and specified bovine (from cow) material properties for the tissues, the simulations showed significant stress and strain at the temporal globe-ON junction propagating through the inner surface of the sclera.

References

1. Suh SY, Le A, Shin A, Park J, Demer JL. Progressive deformation of the optic nerve head and peripapillary structures by graded horizontal duction. *Invest Ophthalmol Vis Sci* 2017;58:5015-21.
2. Wu CC, Kowler E. Timing of saccadic eye movements during visual search for multiple targets. *J Vis* 2013;13.
3. Leclair-Visonneau L, Oudiette D, Gaymard B, Leu-Semenescu S, Arnulf I. Do the eyes scan dream images during rapid eye movement sleep? Evidence from the rapid eye movement sleep behaviour disorder model. *Brain* 2010;133:1737-46.

4. Robinson DA. Control of eye movements. In: Terjung R (ed), *Compr Physiol* Wiley Online Library; 2011:1275-1320.
5. Lee WJ, Kim JH, Shin YU, Hwang S, Lim HW. Differences in eye movement range based on age and gaze direction. *Eye (Lond)* 2019;33:1145-51.
6. Demer JL, Clark RA, Suh SY, et al. Magnetic resonance imaging of optic nerve traction during adduction in primary open-angle glaucoma with normal intraocular pressure. *Invest Ophthalmol Vis Sci* 2017;58:4114-25.
7. Tomlinson RD, Bahra PS. Combined eye-head gaze shifts in the primate. Ii. Interactions between saccades and the vestibuloocular reflex. *J Neurophysiol* 1986;56:1558-70.
8. Tomlinson RD, Bahra PS. Combined eye-head gaze shifts in the primate. I. Metrics. *J Neurophysiol* 1986;56:1542-57.
9. Raab EL. Normal saccadic velocities. *J Pediatr Ophthalmol Strabismus* 1985;22:20-22.
10. Demer JL. Optic nerve sheath as a novel mechanical load on the globe in ocular duction. *Invest Ophthalmol Vis Sci* 2016;57:1826-38.
11. Demer JL, Clark RA, Suh SY, et al. Optic nerve traction during adduction in open angle glaucoma with normal versus elevated intraocular pressure. *Curr Eye Res* 2020;45:199-210.
12. Chang MY, Shin A, Park J, et al. Deformation of optic nerve head and peripapillary tissues by horizontal duction. *Am J Ophthalmol* 2017;174:85-94.
13. Suh SY, Clark RA, Demer JL. Optic nerve sheath tethering in adduction occurs in esotropia and hypertropia, but not in exotropia. *Invest Ophthalmol Vis Sci* 2018;59:2899-2904.
14. Le A, Chen J, Lesgart M, Gawargious BA, Suh SY, Demer JL. Age-dependent deformation of the optic nerve head and peripapillary retina by horizontal duction. *Am J Ophthalmol* 2020;209:107-116.
15. Reddy JN. On the numerical-solution of differential-equations by the finite-element method .1. An introduction to the finite-element method - the Ritz models. *Indian J Pure Ap Mat* 1985;16:1341-1376.
16. Shin A, Yoo L, Park J, Demer JL. Finite element biomechanics of optic nerve sheath traction in adduction. *J Biomech Eng* 2017;139.

Similarly, the following study designed an improved eye model of the average healthy adult eye, simulated adduction using human hyperelastic tissue material properties, analyzed deformations caused by the ON tethering, and explained a possible cause of optic neuropathy relevant to NTG. This manuscript will be submitted to the *Scientific Reports*.

The manuscript included in this chapter:

4.5.1. **Park J**, Shin A, Demer JL. Finite element analysis of adduction tethering of the human optic nerve: effects of tissue property variation. (*in preparation*), 2022.

Contributions to the study: Joseph Park contributed to designing an eye model using Solidworks, and ran an extensive series of FEA simulations using ABAQUS. He also analyzed the data, drew graphs and drawings, and wrote manuscripts for publication.

4.5.1. Finite Element Analysis of Adduction Tethering of the Human Optic Nerve: Effects of Tissue Property Variation

Joseph Park[1, 2], Andrew Shin[6], and Joseph L. Demer[1-5]

[1] Department of Ophthalmology, Jules Stein Eye Institute, Los Angeles, CA, USA.
[2] Department of Bioengineering, University of California, Los Angeles, CA, USA.
[3] Neuroscience Interdepartmental Program, University of California, Los Angeles, CA, USA.
[4] Department of Neurology, University of California, Los Angeles, USA.
[5] Biomedical Engineering Interdepartmental Program, University of California, Los Angeles, CA, USA.
[6] Intelon Optics Inc., Lexington, MA, USA.

Abstract

Traction by the optic nerve (ON) exerted on the eye as it rotates towards the midline (adduction) has been implicated as a possible cause of ON damage induced by repetitive mechanical loading. We designed a computational model, based on realistic anatomy, simulating 6° incremental adduction beyond the initial state of 26° adduction that is the observed average threshold angle for tethering. This model permitted finite element analysis (FEA) of biomechanical effects of observed variations in measured hyper-elastic characterizations of material properties of the anterior, equatorial, posterior, and peripapillary sclera; and the ON and its sheath. The fixed rotational center of the globe, and ON at the orbital apex, were taken as boundary conditions. Intraocular pressure (IOP) and intracranial pressure (ICP) were set to informative levels. For all combinations of local tissue properties, FEA showed that adduction beyond the initiation of ON tethering concentrates stress and strain on the temporal side of the optic disc and peripapillary sclera, the ON sheath junction with the sclera, and retrolaminar ON neural tissue. However, some combinations of tissue properties within the published ranges imposed much higher stresses in these regions than was the case for average tissue properties. With the least favorable combinations of tissue properties, adduction tethering was predicted to stress the ON junction and peripapillary sclera much more than extreme conditions of IOP and ICP. These data support the concept that ON tethering in adduction may in unfavorable cases induce mechanical stresses that contribute to ON damage associated with glaucoma.

Introduction

Damage to the optic nerve (ON), characteristic of glaucoma, is the world's leading cause of incurable blindness [1]. Elevated intraocular pressure (IOP) was formerly considered a defining feature of glaucoma and its major cause [2], yet many patients with primary open-angle glaucoma (POAG) do not have abnormally elevated IOP [3-7]. It has recently been suggested that traction on the ON during numerous accumulated cycles of adduction (rotation towards the midline) may damage the ON and peripapillary tissues, because the ON is so short and geometrically configured that it tethers the globe in large angle adduction [8, 9]. Such ON tethering concentrates the reaction force of the adducting muscle, the medial rectus (MR), against the ON and peripapillary tissues at the site where the ON joins the eyeball [8, 9]. Tethering of the ON in adduction could not by itself explain optic neuropathy, because the tethering phenomenon occurs in nearly everybody when normal adduction exceeds about 26° [8, 10]. However, magnetic resonance imaging (MRI) has shown that the healthy ON stretches during adduction tethering [11], while failure of the glaucomatous ON to stretch much in adduction is associated with globe retraction that does not occur in healthy people in whom the ON typically stretches about 0.8 mm [8]. Esotropia, a convergent binocular misalignment associated with a large bias to excessive adduction, is associated with greater frequency of glaucoma, and in a Korean population conferred a much greater risk of glaucoma that did elevated IOP [12].

Early investigations of the mechanical effects of eye movements have been performed using finite element analysis (FEA). Shin *et al.* [13] and Wang *et al.* [14, 15] developed FEA models that explore ocular deformations during horizontal eye rotations, yet these models were limited in important ways. Wang *et al.* modeled a slack, sinuous ON that would not be informative about

tethering in adduction, and assumed tissue properties from a wide variety of sources and even species [14, 15]. Shin *et al.* incorporated tethering of the ON in its straight configuration at onset of tethering, but employed measured bovine, rather than human, tissue material properties [13]. Both prior FEA studies investigated average or assumed typical issue material properties, without considering sensitivity to outlying values that might contribute to disease such as POAG.

We recently reported hyperelastic tensile characterization of four different regions of the human sclera, ON, and ON sheath, and presented the range, distribution, and inter-correlations of these local biomechanical properties [16]. We also reported that properties in local regions of individual eyes can vary substantially, such that the material properties of one ocular region do not strongly determine properties in another region of the same eye [16]. The current study now employs these characterizations in FEA of the effects of ON tethering in adduction, with particular emphasis on the junction of the ON with the eye.

The current study hypothesized that various combinations of local biomechanical properties of the individual human eye alter distributions and magnitudes of stress and strain around the ON head during adduction tethering. To examine the hypothesis, we aimed to investigate by FEA of adduction tethering the likely range of variation in stress and strain resulting from the interaction of inter-individual tissue variability, in order to gain insight into realistic combinations of tissue parameters that might result in more severe, and potentially pathological, loading during ocular adduction. This analysis considered the ranges of observed hyperelastic properties of ocular tissues, recognizing that their nonlinearity implies that merely considering average behavior of each tissue does not necessarily inform about average mechanical behavior of the overall anatomical system [17]. However, since averages represent obvious intuitive measures of central tendencies, we considered as the reference case a model whose local tissue material

properties are average. From among the numerous combinations of continuously variable hyperelastic properties of individual tissues, we explored combinations of extreme cases actually observed in individual eyes in order to gain insight into potentially pathological situations. In the interest of clarity, we chose average anatomical dimensions for the eyeball and eye socket for the current report, since simultaneous variation of both anatomy and material properties would prohibitively increase the complexity of simulated results in this report.

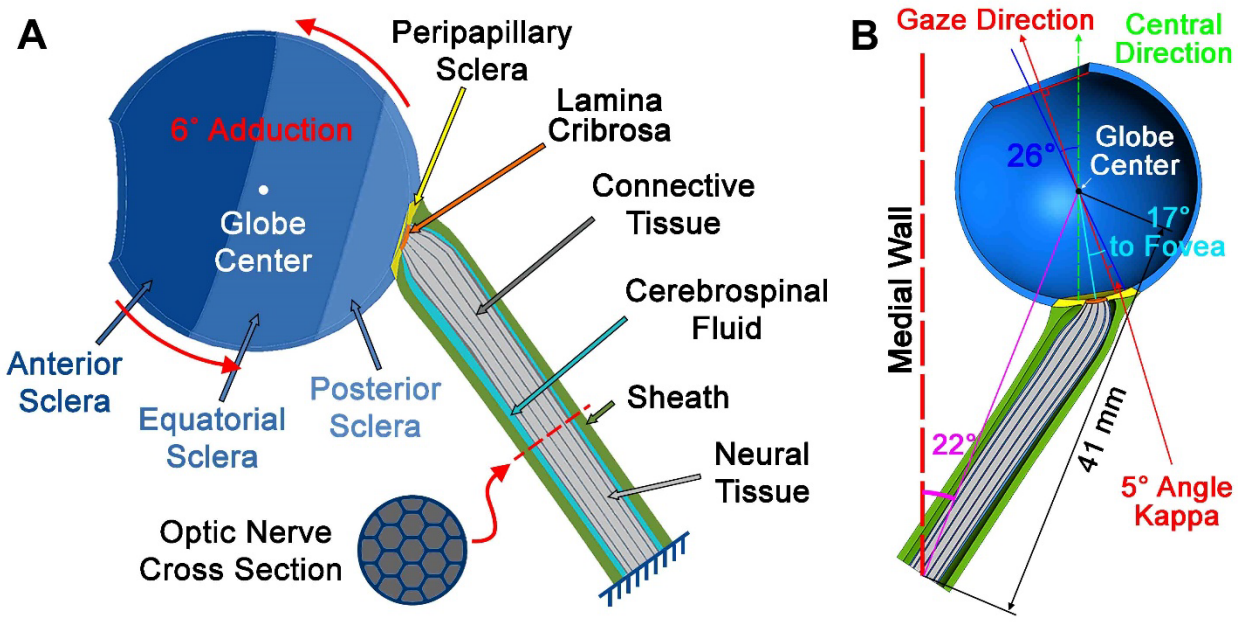

Figure 1. Model geometry. (A) Sclera is parsed into anterior, equatorial, posterior (blue) and peripapillary regions (yellow). The lamina cribrosa (orange) abuts the peripapillary sclera. The posterior lamina cribrosa is joined to the ON (gray), and the ON sheath (green) is joined to the peripapillary sclera anteriorly, and to the orbital apex posteriorly as boundary conditions. CSF is shown in light blue (B) Dimensions of the model.

Methods

Model Geometry. A three-dimensional, hemi-symmetric model was designed using the software package SOLIDWORKS 2017 (Dassault Systèmes, Waltham, MA). Recent optical coherence tomography (OCT) and MRI studies have suggested 26° as the average threshold of ON straightening, beyond which ON tethering occurs and its path remains straight rather than sinuous [8, 10]. Therefore, we defined 26° adduction as the initial configuration for the FEA.

The globe was assumed to be a 24 mm diameter sphere [18], with variable scleral thickness based on measurements ranging from 0.4mm at the equator, increasing to 1mm at the posterior pole, but thinner around the scleral canal [19, 20]. Sclera was modeled with material properties experimentally characterized in in four local regions: peripapillary up to 4 mm radially from the optic disc center [21, 22], and the remaining sclera equally divided into anterior, equatorial, and posterior regions [16]. The model incorporated a 5° angle kappa [23] (the angle between the visual perceptual direction and structural direction of ocular symmetry) and 17° angle between fovea and optic disc center (Figure 1). Lamina cribrosa (LC) thickness was taken to be 0.3 mm with 1.9 mm diameter [24, 25]. We employed dimensions measured from axial MRI of 22 healthy subjects showing 41 mm mean distance between globe center and orbital apex, and a 22° mean angle between a line connecting those points and the medial orbital wall. Although Wang *et al.* [14, 15] modeled the ON as consisting of separate, coaxial layers of pial connective tissue and neural tissue, serial section microscopy with special staining in our laboratory of more than 12 human ONs demonstrates that the pia on the external surface is tightly coupled to a dense network of connective tissue intimately embedded as a matrix throughout the entire human ON cross-section (one example micrograph illustrated in Figure 2) [26]. Therefore, we modeled the connective tissue in the ON as a hexagonal honeycomb structure in which the intrinsic connective and neural tissue are intermixed in

histologically observed 9:16 proportions (Figure 2). The honeycomb was chosen because it is the radially symmetrical structure minimizing total wall length. Also incorporated was the histologically-observed gradual reduction in ON diameter from 4 mm anteriorly to 3.5 mm posteriorly [26]. Average thicknesses of the ON sheath and cerebrospinal fluid (CSF) layer were set to 0.74 mm and 0.59 mm, respectively, based on our human MRI data [8]. The CSF layer was subjected to radially-directed intracranial pressure (ICP). Moreover, nasal shift of the CSF in adduction was incorporated immediately posterior to the globe as observed in MRI [8] making the CSF layer thicker on the nasal than the temporal side.

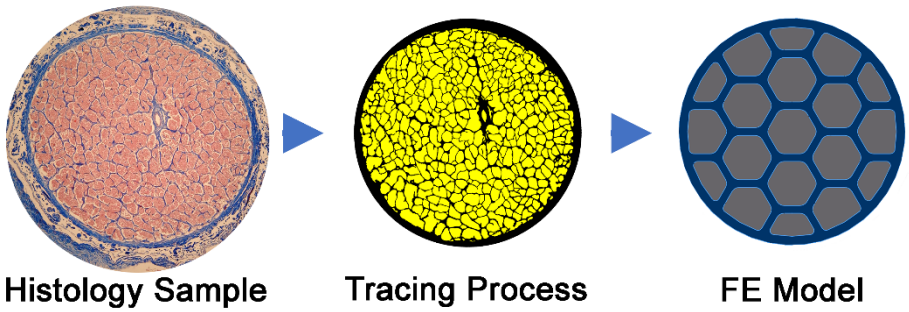

Figure 2. Model simplification of human ON. Transverse histological section of 57 year old human ON illustrates the connective admixed with neural tissue. In this 10 micron thick histological section stained with Mason trichrome at left, neural tissue (pink) was segmented from connective tissue (blue) as outlined as in the middle tracing. Based on the previously published [26] and newly measured area ratio of connective to neural tissue in this study, 9:16 was taken, and the ON was simplified into the honeycomb structure at right for computational tractability.

Implementing Material Properties. After construction of the geometry using SOLIDWORKS 2019, the model was simulated using ABAQUS 2020 (Dassault Systèmes, Waltham, MA). We employed nonlinear elastic tissue properties for each tissue where available [16]. During adduction tethering, FEA indicated wide variation in local stresses and strains associated with variations in tissue material properties. For comparative purposes, we considered hyperelastic stress-strain curves at the 5th percentile to represent "compliant" behavior, and the 95% percentile to represent

"stiff" behavior; this terminology is only informal shorthand for numerically defined hyperelastic functions that we have published [16], and individual tissue properties of stiff, average, compliant are explicitly listed in a supporting information. Combinations of 5th and 95th percentile observed hyper-elastic functions [16] for each tissue were implemented systematically as extremes. This approach provides a tractable sense of sensitivity of stress and strain to extremes of material properties, although of course it hardly encompasses all possible combinations.

Since we did not measure tissue properties of ON neural tissue and LC, we employed the published linear properties for brain neural tissue (1195 Pa, Poisson's ratio = 0.49) [27] for ON neural tissue [27], and averaged nonlinear properties of peripapillary sclera and ON for the LC. The LC is known to be more compliant than that of peripapillary sclera, while the LC is stiffer than the ON.

The ON is effectively a composite material in which soft axon bundles are intermixed with a matrix of stiff connective tissue at a scale prohibiting direct measurement of tensile properties of each component individually. The elastic modulus $E_{Connective}$ for intrinsic ON connective tissue was therefore considered to result from the general rule of mixtures for composite material in the measured portions.

$$E_{ON} = fE_{Connective} + (1 - f)E_{Neural} \qquad (1)$$

where $f = \frac{V_{Connective}}{V_{Connective} + V_{Neural}}$ is the volume fraction of connective tissue, $E_{Connective}$ is the ON connective tissue elastic modulus and E_{Neural} is the neural tissue modulus. We employed the tensile elastic modulus (E_{ON}) of the entire human ON [16], and that of neural tissue taken as published for brain [27], allowing computation of $E_{Connective}$ from Eqn. 1. The von Mises criterion, a common yield criterion for ductile materials, was employed [28].

Boundary Conditions. Electron microscopy has shown that the posterior arachnoid trabeculae that couple the ON to the inner surface of its sheath in the subarachnoid space are several fold thicker near the orbital apex (25 μm ~ 500 μm) than anteriorly near the globe (5 μm ~ 7 μm) [29]. We dissected unfixed human orbits (obtained in conformity with legal requirements from anatomical donations) and found that both the ON and its sheath both appear rigidly fixed in the orbital apex. The apical end of the ON and sheath was therefore taken to be a fixed boundary for both tissues.

For computational efficiency, the eye model assumed hemi-symmetry about a horizontal plane, since only horizontal eye rotation was simulated. The ocular rotational axis was assumed fixed at the geometrical globe center. The anterior sclera, which is the stiffest scleral region, was assumed to undergo uniform rotation by a forcing function that implemented the adduction.

Input Loading. The model was designed to incorporate a straight ON at 26° initial adducted gaze angle, and from this position was perturbed by a further 6° adduction. Unless otherwise stated, normal IOP (15 mmHg) and normal ICP (10 mmHg) were applied to the vitreous body and CSF layer, respectively.

Mesh. The model was non-uniformly meshed using 386,983 10-node quadratic tetrahedral elements. Mesh size was variably assigned depending on the tissue of interest (Figure 3A). The mesh in and around the ON head was relatively fine because of its relevance to optic neuropathy. The mesh quality was confirmed by a convergence test shown in Figure 3B. Since the globe-ON junction was considered as the region of interest, the middle portion of the mesh was incrementally

checked from coarse to fine tetrahedral elements. Other regions, including anterior and posterior portion sclera, were coarsely meshed regardless of the mesh size elsewhere.

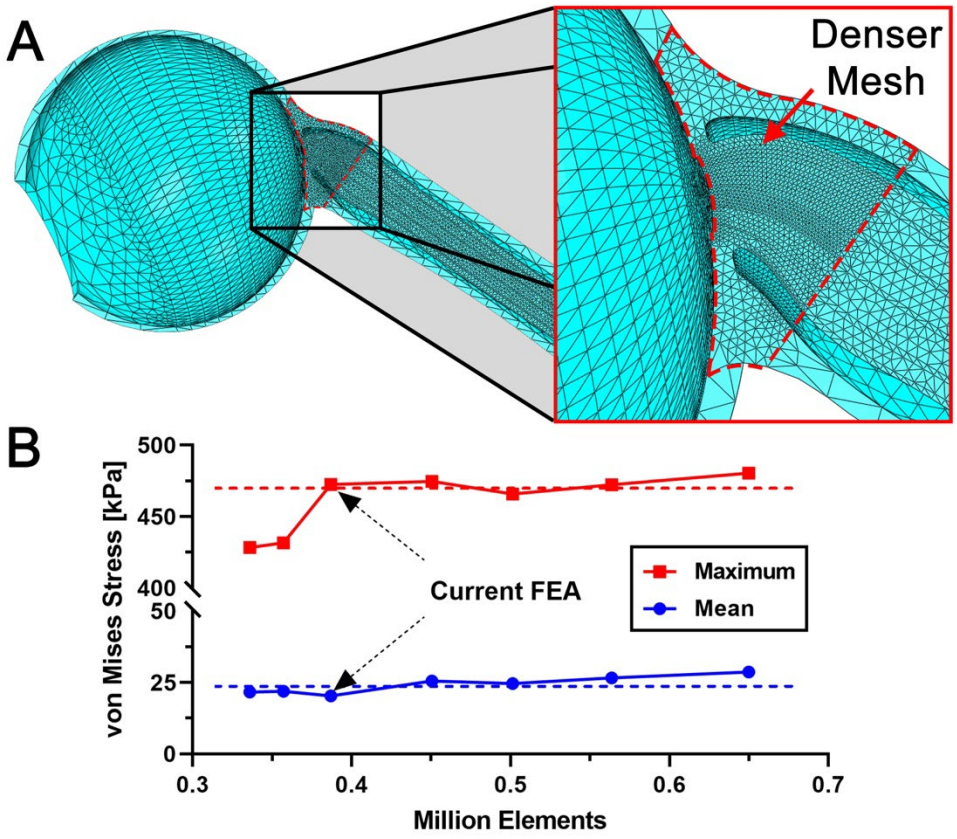

Figure 3. (A) Local mesh size was adjusted according to the relevance of the region, being finest around the optic nerve head. (B) Mean and maximum values of von Mises stresses of the all elements in the model were stable throughout all element numbers evaluated. Dotted-lines indicate mean of each point.

Stress and Strain Measurements. For the comparison among individual cases, 12 ~ 16 tetrahedral elements in corresponding regions of interest were averaged to quantify local representative stress and strain. Regions of interest were selected at relevant concentrations of stress and strain.

Results

Model Implementing Average Tissue Properties. Continued ocular adduction beyond the angle at which the ON had exhausted its sinuosity resulted in tractional loading by the ON. Ocular stress and strain distributions during this adduction beginning at 26° and continuing an additional 6° to a 32° final angle are illustrated in Figure 4 for the case of average tissue properties, implemented by average experimentally-characterized reduced polynomial functions [16] measured for human anterior sclera, equatorial sclera, posterior sclera peripapillary sclera, the ON, and the ON sheath. At the conclusion of this 6° incremental adduction, tractional loading propagated from the temporal ON junction to the inner peripapillary sclera, which experienced around 141 kPa stress and 5% strain, with lesser deformations widely distributed throughout sclera and ON sheath, as shown in Figure 4. The model indicated 4% strain in the ON internal connective tissue adjacent to the temporal border of the LC.

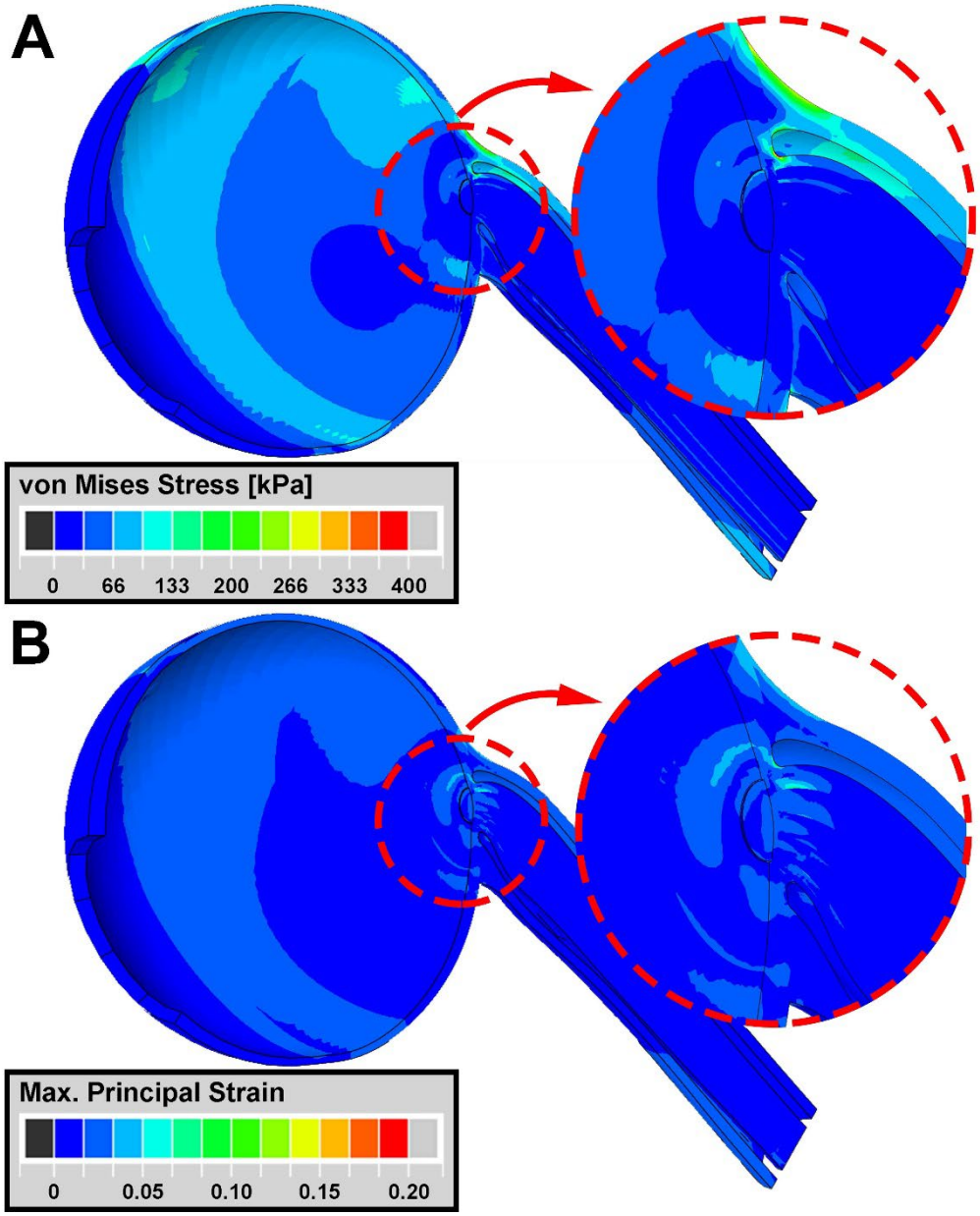

Figure 4. Simulation of adduction to 32° from initial tethering at 26°, employing average measured tissue hyper-elastic functions. Contour maps of (A) von Mises stress and (B) principal strain. Stress-strain effects mainly occur in and around the ON head in the region enclosed by red dotted circles.

Sensitivity Analysis. Sensitivity to extreme variations was analyzed by systematically modeling stiff versus compliant material properties in local ocular regions. These models indicated large stress and strain variations during adduction tethering, with informative combinations illustrated in Figure 5. Cases such as A, C, D, E, G, and H had less than average case stresses on the temporal ON junction, while cases B and F exhibited greater than average case stress. All except cases A and E exhibited higher strains than for the average case in the temporal ON junction. Selection of paired extremes of ON sheath properties (Cases A-B, C-D, E-F, G-H) indicated that when ON the sheath was relatively compliant, stresses in posterior sclera and ON sheath were smaller, and stresses in peripapillary sclera and ON were larger. Strains during adduction tethering in the retrolaminar ON neural tissue, peripapillary sclera and ON were greater with a compliant ON sheath. Comparison of paired extremes of peripapillary scleral properties (Cases A-C, B-D, E-G, F-H) demonstrated that stiff peripapillary sclera resulted in less stress on the ON sheath, but at the same time more stress on the peripapillary sclera, and ON junction. Stiff peripapillary sclera resulted in smaller strains within it but larger strains on the retrolaminar neural tissue. Comparisons among cases selecting paired extreme properties of only the posterior sclera (Cases A-E, B-F, C-G, D-H) showed that stiff posterior sclera was associated with greater stresses on the ON sheath, and posterior sclera and strains on the globe-ON junction.

Local stresses and strains in the anterior ON and peripapillary region for particularly informative cases chosen from Figure 5 are illustrated in greater detail in Figure 6. Cases B, C, and D are informative because they exhibited the highest and lowest stresses and strains. The peripapillary sclera is known to stiffen in normal aging [22] and also in POAG [30]. Among all cases shown in Figure 5, Case B exhibited the greatest stress in the temporal ON junction at 291 kPa, peripapillary scleral stress at 95 kPa, and retrolaminar ON strain at 6%. Case B features the stiff

posterior and peripapillary sclera believed to occur in POAG; the simulation suggests that when these tissues are stiff, a simultaneously compliant ON sheath would shift loading to the temporal optic disc region, which is a common site of damage in POAG.

Simulation of Case C indicated extreme stress (3.91 MPa) on the scleral junction with the ON sheath that extended temporally into the posterior pole. This case employed stiff posterior sclera, compliant peripapillary sclera, and stiff ON sheath. It has been suggested that stress due to ON traction may contribute to formation of temporal optic disc tilting and staphylomatous ectasia commonly observed in axial high myopia [31]; the stress concentration closely matches the typical pathological distribution [32].

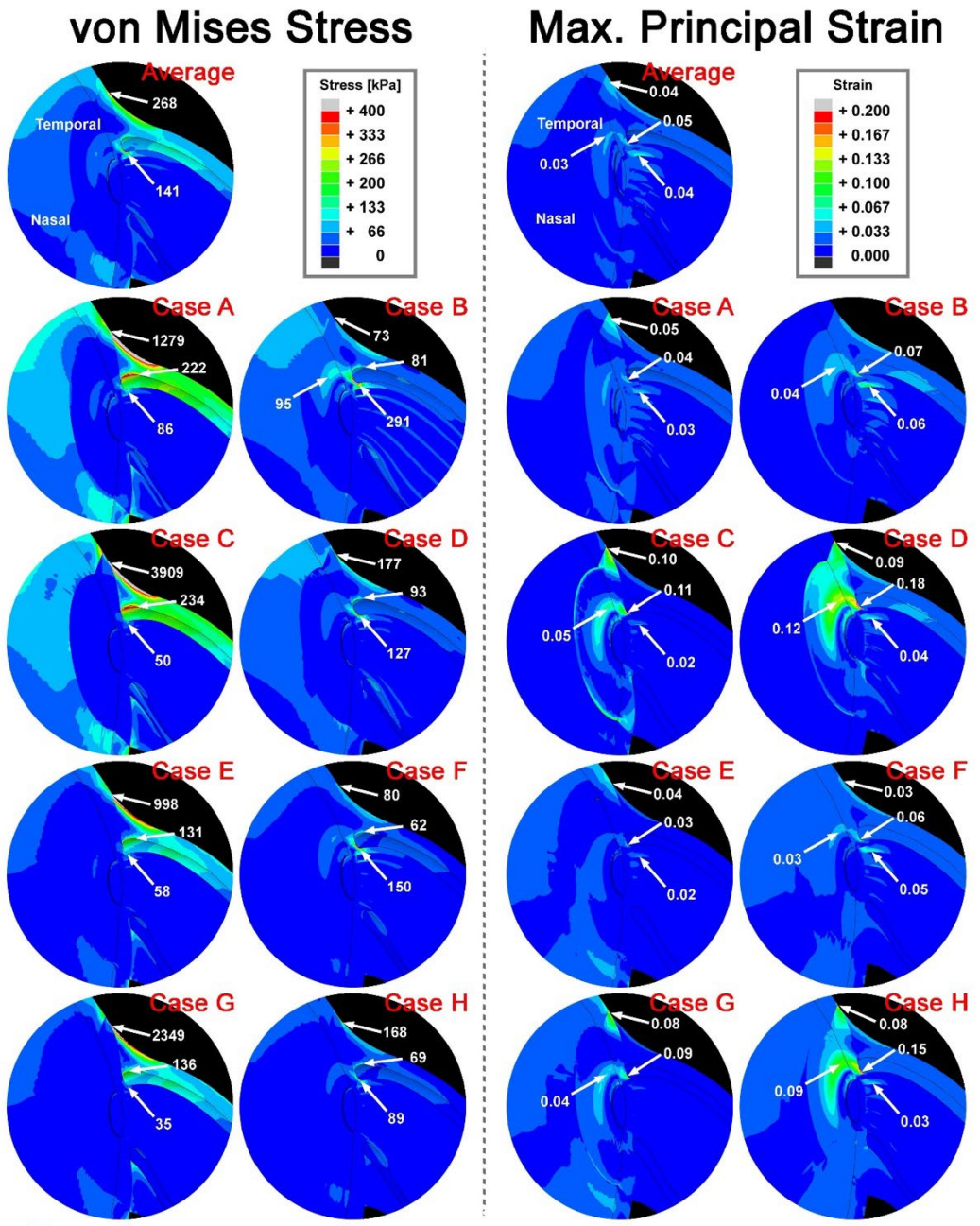

Stiffness Combination

	Case A	Case B	Case C	Case D	Case E	Case F	Case G	Case H
Posterior Sclera	Stiff	Stiff	Stiff	Stiff	Compliant	Compliant	Compliant	Compliant
Peripapillary Sclera	Stiff	Stiff	Compliant	Compliant	Stiff	Stiff	Compliant	Compliant
Optic Nerve Sheath	Stiff	Compliant	Stiff	Compliant	Stiff	Compliant	Stiff	Compliant

Figure 5. Sensitivity to variations in regional ocular material properties, as implemented by reduced polynomial functions for which the indicated qualities are shorthand, during adduction 6° beyond tethering at 26°. Stiff and compliant material properties were set to 95% and 5% percentile values, respectively, of preconditioned stress-strain functions [16]. Material properties for regions not noted were set to average observed reduced polynomial functions.

The simulation in Case H exhibited the most extreme strain, in and around the temporal peripapillary sclera at 9 to 15%, but only low stress throughout. Case H therefore might hypothetically reflect the situation in children, whose highly compliant posterior ocular tissues deform harmlessly under relatively low stress.

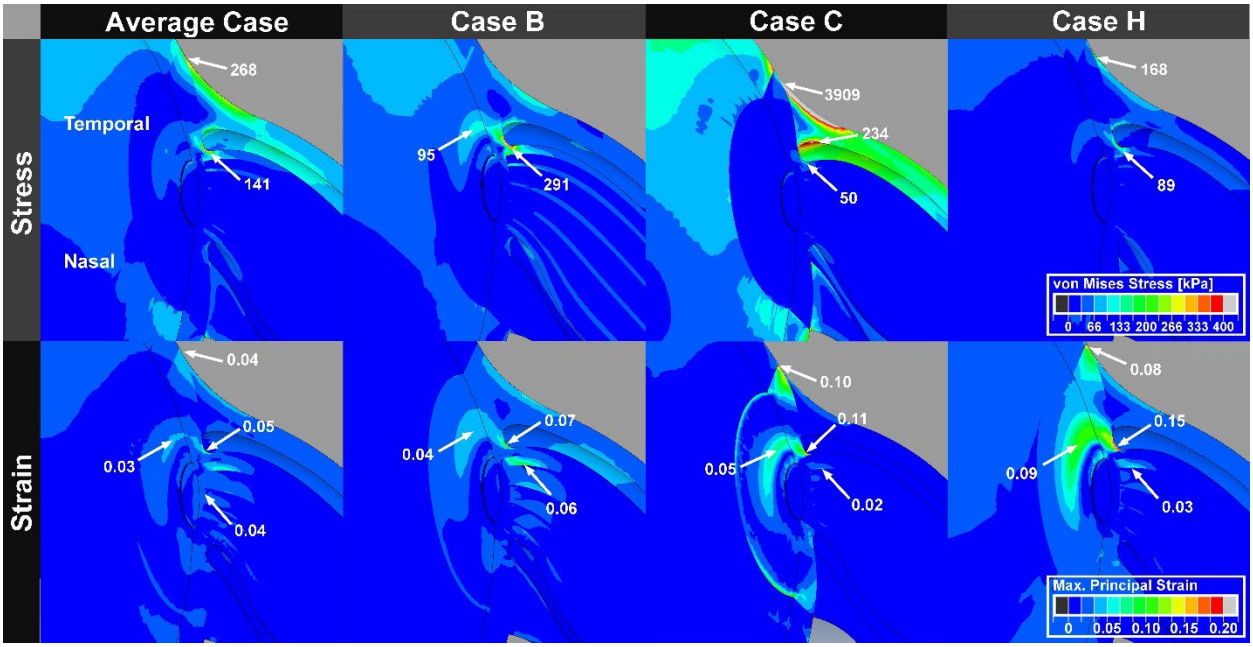

Figure 6. Finite element analyses implementing extreme combinations of observed tissue properties, during adduction 6° beyond tethering at 26°. Left column, average case employing mean values for all tissues. Second column, Case B employing stiff posterior and peripapillary sclera and compliant ON sheath; this might hypothetically represent primary open-angle glaucoma. Third column, Case C employing stiff posterior sclera, compliant peripapillary sclera and stiff ON sheath; this hypothetically represent axial high myopia. Right column, Case H employing universally complaint posterior sclera, peripapillary sclera and ON sheath. Conventions otherwise as in Figure 5.

Scleral Displacement. Scleral displacement during adduction tethering was demonstrated by superimposing the model's rigid anterior sclera in the initial and 6° adducted positions (Figure 7). In the simulation employing average tissue properties, the temporal edge of LC shifted 458 μm nasally and 604 μm posteriorly during adduction tethering. Extreme case B had smaller LC displacement in both nasal-temporal (x_B, 300 μm nasal) and anterior-posterior (y_B, 563 μm posterior) directions than did the average case where the LC shifted 458 μm nasally and 604 μm posteriorly (Figure 7). On the other hand, extreme cases C and D showed more LC shift nasally and posteriorly than the average case: there was 542 μm nasal shift and 658 μm posterior shift in case C, and 333 μm and 679 μm shift in case D, respectively.

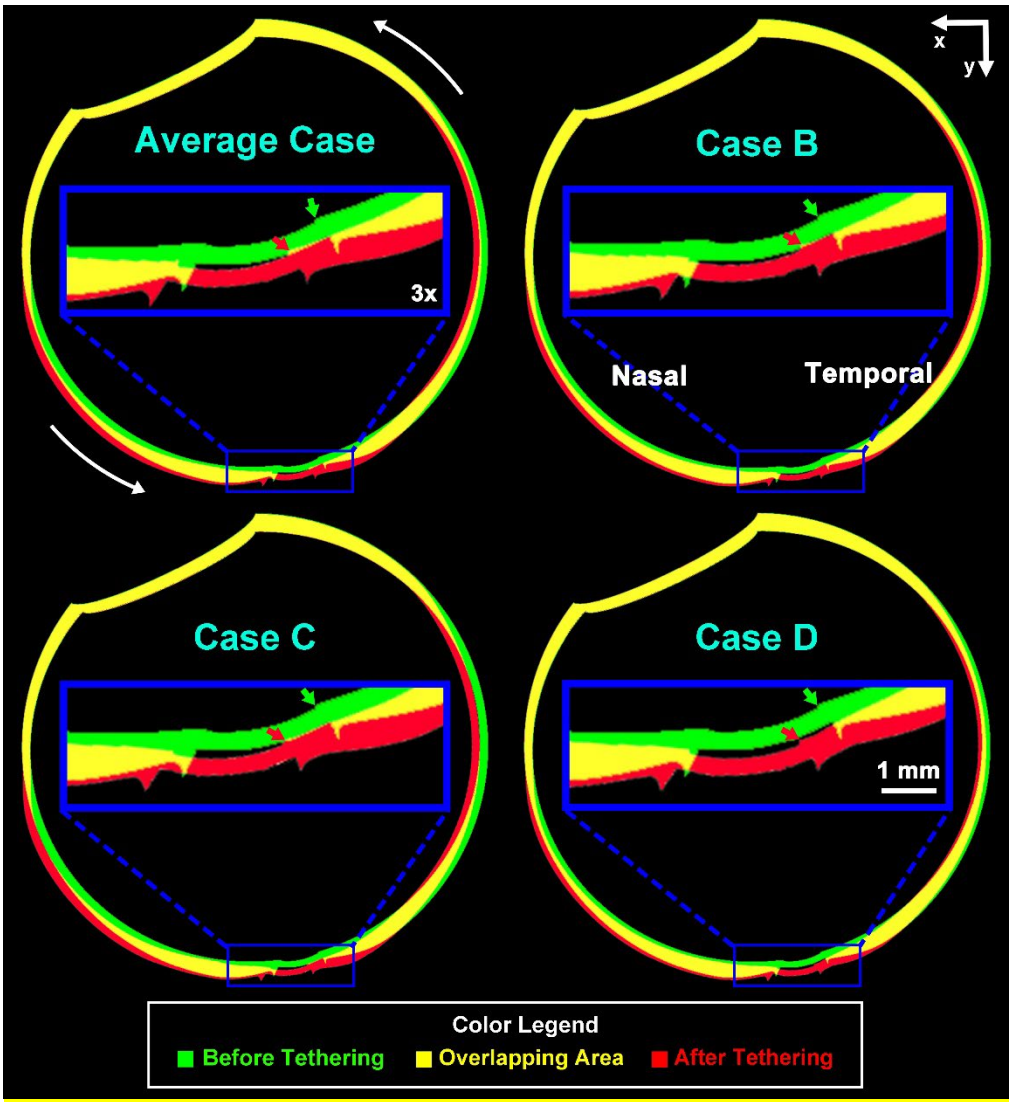

Figure 7. Horizontal cross sections of finite element model superimposing initial configuration of 26° adduction (green) with final configuration of 32° adduction (red) for various combinations of observed tissue properties as defined in Fig 2. Yellow colored region represents overlap of 26° and 32° adduction. Blue box shows 3X magnified view of the optic disc region where arrows indicate locations of temporal edge of the LC before (green) and after (red) tethering.

Pressure Effects. The translaminar pressure differential between IOP and ICP has been proposed as a cause of ON damage in glaucoma [33-35]. To evaluate the importance this translaminar pressure gradient relative to ON traction, we simulated 6° adduction beyond ON straightening in the presence of an extreme 36 mmHg pressure gradient caused by high (40 mmHg) IOP and low ICP (4 mmHg), comparing this situation without adduction tethering but subject to identical pressures. As shown in Figure 8, for the case of average tissue properties, stress in the temporal ON junction with the extreme translaminar gradient during adduction tethering was larger (174 kPa) than stress observed during tethering at normal pressures (141 kPa); the difference of 33 kPa (174 - 141 kPa) is two folds larger than the modest 17 kPa (25 – 8 kPa) stress due to the pressure gradient alone without adduction tethering. However, these values are still less than for adduction tethering assuming the extreme material properties of case B but normal IOP and ICP levels. During adduction in case B with normal IOP, there was 95 kPa stress at the temporal border of the peripapillary sclera, which is the site where peripapillary atrophy most frequently occurs [36]. This stress concentration was smaller during simulation of the average case during adduction tethering (51 kPa), while 76 kPa was simulated in this region under extreme conditions of high IOP and low ICP. Taken together, these simulations indicate that the disc and temporal peripapillary region of an eye with average material properties and subject to normal IOP and ICP undergoes greater stress during adduction tethering than does an eye subject to markedly elevated translaminar pressure gradient in the absence of adduction tethering. However, when adduction tethering occurs in the presence of elevated translaminar pressure gradient, stress in these regions is only very modestly increased, roughly summing the large effect of tethering with the smaller pressure effect. Stress is even greater when adduction tethering occurs with a "stiff" ON (Figure 9 lower left) even with normal pressures.

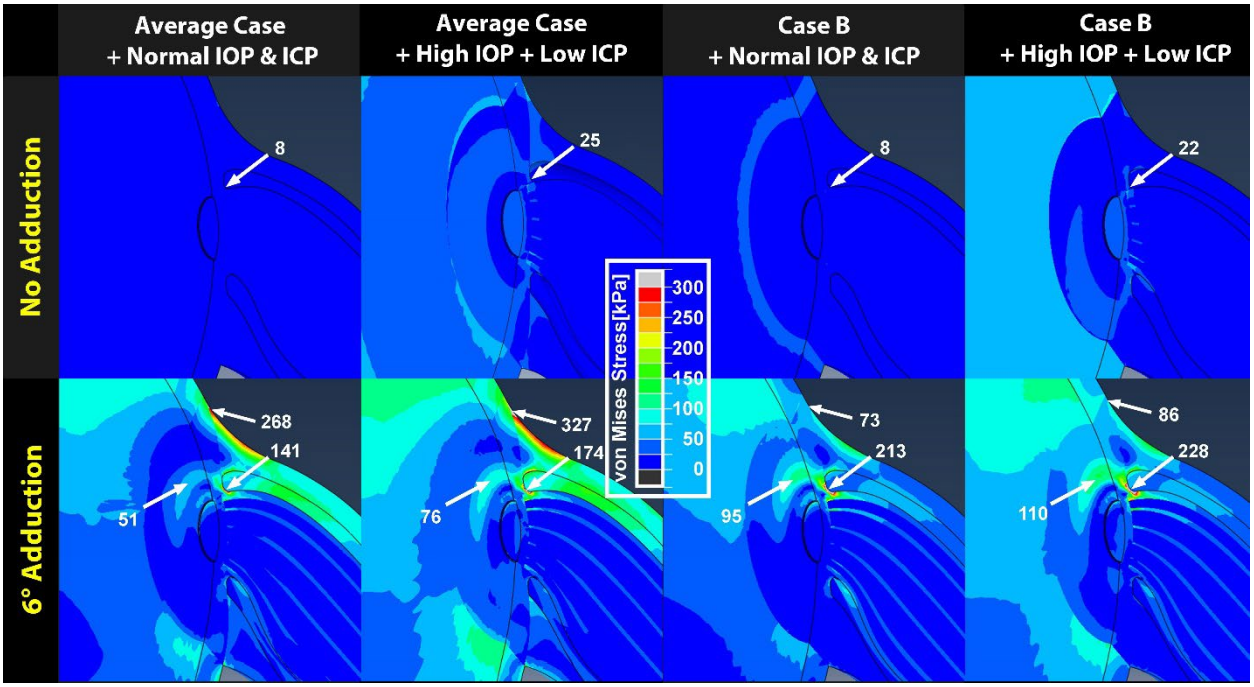

Figure 8. Finite element model of 6° adduction past first ON tethering demonstrating additional influence of IOP and ICP on stress distributions in the peripapillary and ON region. Material property cases are defined in Figure 5. In upper panels without adduction tethering, note small stress due to 40 mmHg IOP (high) and 4 mmHg ICP (low), in comparison with lower panels showing larger effect of adduction. Comparison of lower right two panels for Case B demonstrates that during adduction, stress in the temporal peripapillary sclera and ON junction is 15 kPa higher when IOP is high and ICP is low, than when pressures are normal.

Stiff Optic Nerve Concentrates Stress. The sensitivity of the model to variation in ON tissue properties was simulated assuming the stiff posterior and peripapillary tissue properties of Case B (Figure 9). This case may be informative about the effect of ON stiffening that is an observed feature of POAG. Assuming constant neural tissue properties [27] along with observed variations in measured whole ON tensile properties were employed to calculate the variation of intrinsic connective tissue properties using the rule of mixture (Eqn. 1). Simulation that assumed normal IOP and ICP indicated greater stress in and around the temporal ON junction when the ON was stiffer (Figure 9 lower left) than for an average ON stiffness (Figure 9 upper left), but less stress when the ON was less stiff (Figure 9 upper right) than average (Figure 9 upper left). Stress on

the ON junction in case B with a stiffer ON (226 kPa) was about 54% greater than for the average case, but about 63% less when the ON was relatively compliant (54 kPa). These simulations thus suggest that mechanical properties of the ON itself have substantial influence on the mechanics of the optic disc during adduction tethering. In addition to the simulation with stiff ON, an extreme pressure gradient was added to the simulation to estimate the effect of extreme pressure (Figure 9 lower right). Comparing to the case with normal IOP, stresses on the temporal peripapillary sclera (173 kPa), intrinsic connective tissue inside the ON (289 kPa), and ON junction (482 kPa) increased more than 15%.

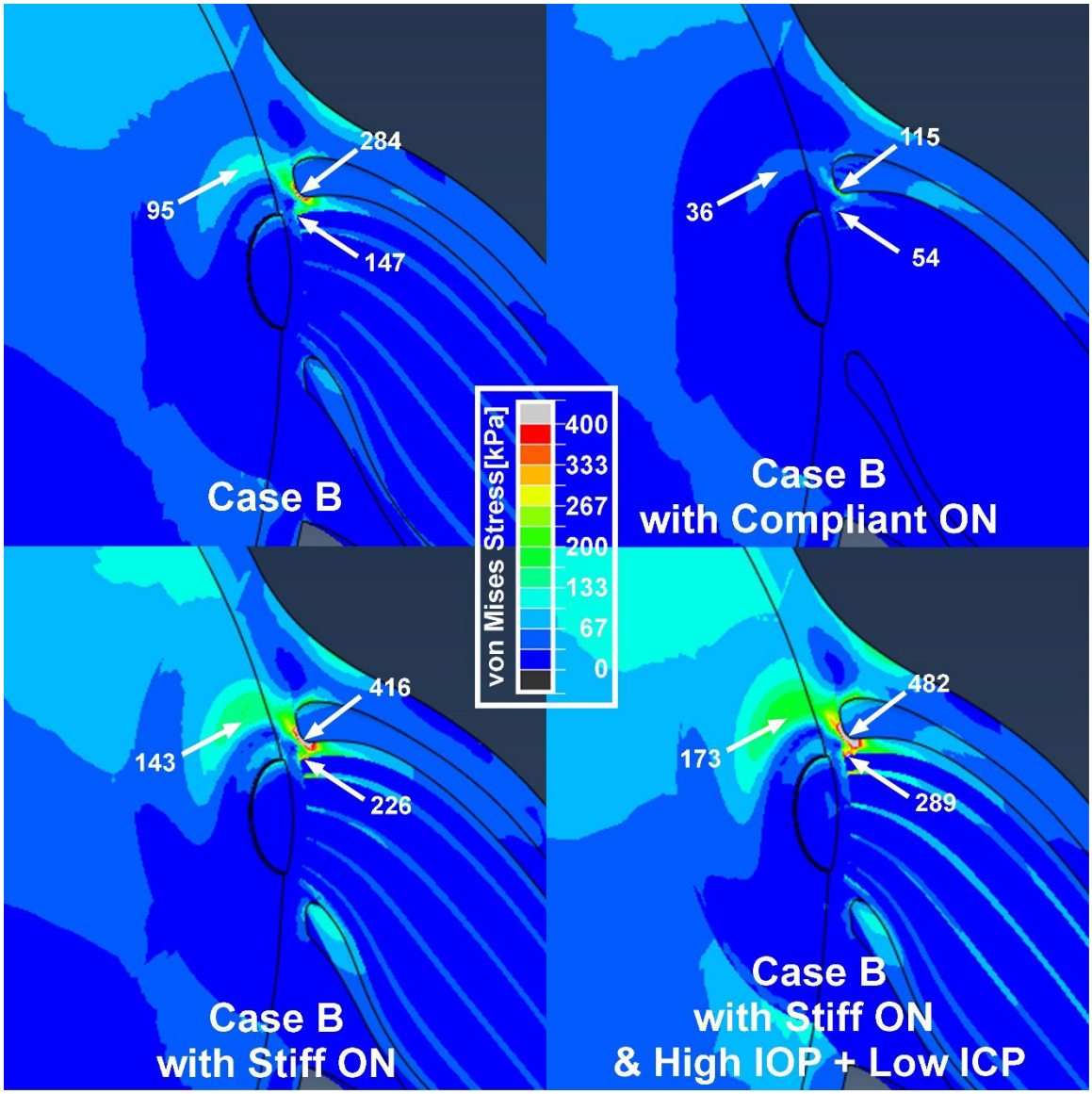

Figure 9. Sensitivity to ON stiffness more or less than average, assuming the least favorable combination of other tissue properties (case B) with normal IOP and ICP. The right bottom panel assumes an extreme translaminar pressure gradient (40 mmHg IOP and 4 mmHg ICP).

Discussion

The present modeling study extends the quantitative analysis of the effects of ocular adduction tethering from bovine [13] parameterization to more relevant, nonlinear tissue material properties measured in humans [16]. The most significant insight from the current human FEA is that

variations within the observed range of measured tissue properties markedly influence the magnitudes and distributions of resulting stress and strain during adduction tethering of the ON. In extremes such as cases B, C, and D, adduction tethering caused large stress concentrations in peripapillary sclera and the optic disc region, focally concentrated where peripapillary atrophy typically develops [36-40], and where optic neuropathy typically occurs in POAG [33, 41, 42]. These findings are therefore consistent with the proposal that both peripapillary atrophy and glaucomatous optic neuropathy might result from repetitive mechanical injury during numerous cycles of adduction tethering during the life span [8-10, 13]. The model predicts that stress and strain in the optic disc and peripapillary region are markedly greater when the ON itself is relatively stiff, a characteristic recently reported in patients with POAG [11]. Finally, while suggesting that adduction tethering imposes markedly greater stress on the optic disc and peripapillary region than does translaminar pressure alone, translaminar pressure elevation contributes modest but roughly additive additional stress when combined with tethering. It is important to bear in mind that this hemisymmetric model ignored possible vertical asymmetries in ON path in the orbit that might result in vertically asymmetrical loading during adduction tethering; an FEA including vertical asymmetries would be possible, but would require at least twice the current (considerable) computational burden.

Stress vs. Strain. In this study, FEA suggests that both stress and strain are induced by ON tethering during adduction tethering in humans. While it is likely that extreme transient neural strain, such as in traumatic optic neuropathy, might acutely damage the neural tissue of the ON [43, 44], the eye is, of course, built to rotate a great deal during its normal function. The normal ON stretches harmlessly even during adduction tethering [11]. The peripapillary sclera of children is

more compliant than that of adults [22]. Infrared fundus imaging shows that the optic disc and peripapillary region deform more during horizontal eye rotation in young adults than older healthy subjects [45], and our own data indicate that horizontal eye movements create even greater deformations in healthy children (Moon *et al.*, unpublished data, 2021). Therefore, strain in these tissues should be regarded as within physiologic limits and not pathological. In fact, strain in this region is probably a good thing. ON strain in the posterior eye is subnormal in POAG, where the ON fails to stretch normally during adduction tethering [11]. Therefore, it seems more likely that adduction-related stress rather than strain is a pathologic factor in ocular disease. Specific down-stream mechanobiological mechanisms that might mediate stress effects surpass scope of this paper, yet are implicit or explicit in most theories of glaucoma and other optic neuropathies [46-50]. This proposal of repetitive stress injury to the ON caused by eye movement presumes inciting mechanics of down-stream phenomena.

Initial Optic Nerve Configuration. Wang *et al.* [14, 15] modeled the effect of horizontal eye rotation using FEA, but the initial configuration of the ON in their model was sinuous. Even in central gaze, the degree and shape of ON sinuosity varies widely among individual people, and of course changes with gaze direction unless the ON is tethered. It has been reported that ON sinuosity significantly greater than normal in POAG [11]. The anatomical and mechanical factors contributing to this sinuosity are currently unknown, but the sinuosity makes biomechanical simulations more complex than for a straight ON. In the laboratory, we find that a sinuous human ON specimen from an eye bank donation is deflected or partially straightened with minimal applied force, but stress increases markedly when the same ON is stretched after being pulled straight under tensile loading. In performing mechanical testing of scores of fresh human ONs in our laboratory, we

have not observed a natural tendency towards sinuosity. Clearly, Wang *et al.* [14, 15] are correct that the ON is loaded by forces during abduction and adduction to angles less than the 26° tethering threshold, because in vivo imaging demonstrates optic disc and peripapillary deformations under these conditions where the ON is typically still sinuous [10, 11, 45]. However, the large shape change from a sinuous and tethered ON is not only suboptimal for consideration of tensile strain [51], but also problematic to implement in FEA, as this transition amounts to a fundamental change in model geometry. The current FEA was therefore limited to the situation of the empirically-verified straight ON for which we have adequate tensile data and needed no assumptions about shape or its anatomic determinants.

Behavior with Average Tissue Properties. The FEA with average tissue properties (Figure 4) demonstrated representative ON tethering effect during 6° further adduction beyond the 26° adducted starting position. Stress and strain were concentrated at moderate levels in and around the optic disc, and the ON and its sheath. Both the temporal and nasal sides of the peripapillary sclera and LC were significantly displaced nasally and posteriorly during adduction tethering (Figure 7). Stress and strain concentrations were larger in the temporal than nasal ON head (Figure 4), associated with nasal and posterior movements of the LC.

Justification of Independent Variations in Tissue Properties. Modest cross-correlation among mechanical properties of various regions of the globe, ON, and sheath has been demonstrated [16]. For example, the strongest regional correlation demonstrated that only 59% of the variation in ON sheath tangent modulus is predictable from variation in anterior scleral modulus, and the lowest regional correlation showed that as little as 1% of the variation in ON modulus is predictable from

its sheath modulus. This finding justifies the possibility of considering independently varying stiffnesses of each ocular region in the current sensitivity analysis (Figure 5).

Sensitivity to Variation in Tissue Properties. Modeling consistently showed loading effects during adduction tethering to be greater on the temporal than the nasal side of the optic disc, and mainly in and around the globe-ON junction (Figure 5). Comparisons of FEA cases in Figure 5 suggested that stiff posterior sclera induces both greater stress and strain on the peripapillary sclera, ON, and ON sheath by delivering rotational force to the posterior region rather than absorbing from by deformation of the posterior sclera. In this way, posterior sclera normally functions as a buffer that reduces stress and strain in the ON head [52].

Modeling here suggests that stiff peripapillary sclera lowers ON sheath stress and limits its overall strain, while this stiffness increases stress in and around the temporal peripapillary sclera and its junction with the ON. Interestingly, a highly compliant peripapillary sclera relieves ON stress by deformation near the temporal ON junction (high strain case D in Figure 6). Case H might hypothetically represent the case of a healthy child's eye: all tissues are compliant enough that total amount of stress is low, but with high strain in and around the optic disc. Children's tissues, including the eye, are known to be more compliant than in the old adult, enabling the child to absorb mechanical energy without damage [22, 53, 54].

Low ON sheath stiffness is associated with greater stress near the ON junction and greater strain on the retrolaminar neural tissue during adduction tethering, effects that might plausibly induce optic neuropathy when repeated sufficiently often [33, 42]. Focal stress is widely presumed or demonstrated to induce ocular tissue remodeling [32, 42, 47-50, 55-57] On the other hand, in the case of C in Figure 6, FEA suggested that adduction tethering with a stiff ON sheath induces nearly 4 MPa

stress at the scleral junction of the ON sheath. Stress concentration that the temporal border of the optic disc in Case C has the same distribution of typical peripapillary changes in axial myopia, perhaps providing an explanation for progressive temporal tilt of the optic disc and elongation of axial length [8, 13, 58].

Modeling suggests the most favorable combination (Case G) of material properties to minimize temporal ON junction stress during adduction tethering may be when compliant posterior and peripapillary sclera absorb the force of adduction tethering, but a stiff ON sheath protects the compliant ON from appreciable loading. The least favorable combination (Case B) of material properties heavily stressing the temporal ON junction may be when stiff posterior and peripapillary sclera transfer globe adduction force to an ON junction that is not well protected by the ON sheath. Most parts of the human eye, including the ON, stiffen during aging [22, 53, 54]. If we presume case A (all stiff tissues) as representative of a healthy older adult, and case H (all compliant tissues) as representative of a healthy young person, pathological Case B might progressively emerge over a lifetime if the ON sheath stiffens more slowly than the sclera. Since we have experimentally confirmed the low cross correlation between ON sheath and scleral material properties (Pearson's $r = 0.34$) [16], different amounts of tissue stiffening are likely to occur in some individual eyes.

Scleral Deformation in Adduction. Comparisons of scleral deformation induced by ON tethering demonstrated horizontal and vertical displacements of the temporal edge of LC in the average and extreme cases (Figure 7). There were nasal and posterior LC shifts in all cases. Recent investigations [59-61] have observed dragging of the central vascular trunk and LC during axial elongation of the healthy myopic child's eye. Nasal dragging of the LC was prominent, but the authors did not speculate on its cause [59-61]. As shown in Figure 7, the LC would be dragged nasally and posteriorly if the ON is tethered during adduction. The displacement of the LC observed in OCT images corresponds to the temporal peripapillary strain predicted by the current FEA [59-61].

Adduction Tethering and Pressures. Although scleral and optic disc deformations induced by IOP have been studied extensively [21, 25, 49, 62-66], and severely elevated IOP can rapidly inflict severe ON damage. It is now acknowledged that elevated IOP does not cause most cases of POAG, but IOP is merely the only modifiable risk factor. Many patients with POAG, especially Asians [4, 6, 67-69] lack abnormally elevated IOP [70] and suffer ON damage at normal (<22mmHg) IOP [71]. In patients with POAG, IOP is normal in 30-39% of whites [72-74], 57% of blacks [75], 70% of Chinese [69], and 92% of Japanese [76]. Meta-analysis of tens of thousands of patients found no statistical relationship of IOP to POAG [69]. The term "normal tension glaucoma" (NTG) has been employed to describe these patients with POAG without elevated IOP. The absence of effect of IOP in NTG is evident in multiple populations. For example, in Korea, no measure of IOP correlates with development of glaucomatous visual field defects [77], or their progression [78, 79]. In North America, baseline IOP in the Ocular Hypertension Treatment Study was only minimally predictive of development of NTG [80]. Progression of glaucomatous ON damage is not predicted by higher IOP [81], but actually predicted by lower IOP [81]. Even when therapeutically reduced, IOP level does not statistically

predict progressive ON damage[82], and about 20% of patients suffer it 5 yrs after 30% IOP reduction from levels normal to begin with[71]. While therapeutic IOP reduction hwas shown in a large study to reduce progression of visual damage in NTG, the beneficial effect was only evident when combined with cataract extraction [83], and in another large study, the amount of therapeutic IOP reduction did not correlate with less progression of glaucomatous damage [84]. Aggressive IOP reduction of at least 20% in NTG reduces progression of ON damage only slightly [82]. While the translaminar IOP gradient against ICP has also been proposed to cause POAG [34, 85-87], this is dubious, since Pircher *et al.* have demonstrated no relationship between translaminar pressure and glaucoma [88], even when posture was systematically altered relative to gravity [47].

The current FEA may help clarify these seemingly paradoxical findings. Prior FEAs have predicted strains in the optic disc and peripapillary sclera due to IOP elevation [49, 62, 89]. However, the current FEA employing human tissue properties indicates that ON tethering in adduction imposes much higher stresses on the optic disc, retrolaminar ON, and peripapillary sclera – the main sites of glaucomatous damage – than does markedly increased translaminar pressure (IOP – ICP). The mechanical effect of translaminar pressures approximately adds to the effect of adduction tethering, but only marginally because the pressure effect is relatively small. But when adduction tethering occurs in the setting of a "stiff" ON with "compliant" ON sheath (these casual terms are but shorthand for the hyperelastic functions actually employed), the stresses in visually critical ocular regions are greater still, and increase relatively little more in the presence of IOP or translaminar pressure elevation (Figure 9 lower right). It is thus plausible that IOP elevation plays a minor but supplementary role to eye movement in the pathogenesis of NTG [49, 62, 89, 90]. Voorhees *et al.* [90] explained deformation of the LC by hoop-stress induced by elevated IOP. In the same manner, Figure 9 lower right demonstrates the highest stress concentration among all cases on the

temporal ON head and peripapillary region with the worst material property combination (Case B with stiff ON) under high translaminar pressure by adding the IOP induced hoop-stress.

With the least favorable combination of tissue material properties modeled (case B) under normal IOP, stress due to adduction tethering was larger than with average tissue material properties, even under highly elevated IOP (40 mmHg) and low ICP (4 mmHg, Figure 8). Clinical data indicate that high translaminar pressure is not typical of NTG [86, 88], but adduction is incessant. Even sleep does not stop saccades [91]. Adduction to 32° as employed in this FEA encompasses little more than half the 55° human oculomotor range [92]. Larger conjugate horizontal eye movements are physiologic, and around three horizontal saccades occur per second [93], cumulatively 183,000 each day [94]. The biggest saccades are reflexive in association with ambulation and head movements. When the head and body are free to move, 25-45° saccades happen often [95], along with automatic slow phase counter-rotations generated by the vestibulo-ocular reflex [96]. People make horizontal saccades exceed 40° occur during commonplace activities such as walking, catching a ball, searching for objects, and preparing a drink [97].

Effect of Optic Nerve Stiffness. Clark *et al.* [11] have demonstrated stiffening of the ON in POAG by examining ON elongation during adduction tethering [11]. The current FEA suggests that ON stiffness is a key determinant of optic disc stress. Figure 9 demonstrates that the level of stress on the ON junction significantly depends on ON stiffness. Case B with a stiff ON exhibited much higher stress at the ON junction than the most extreme case in Figure 5, while stress there was much less with a compliant ON, than that of average case.

Comparison of Model with Optical Imaging. Temporal shifts of nasal peripapillary tissues have been demonstrated by optical imaging during adduction [45], where OCT has also demonstrated a see-saw posterior shift of the temporal edge, and anterior shift of the nasal edge of Bruch's membrane [10]. This observation [45] represents relative motion consistent with the current FEA, since OCT interpretation of peripapillary deformation requires superimposition of reference regions of a limited optical imaging field. In contrast, superimposition of the current FEA reflects deformations throughout the entire globe.

Limitations. The material characterization employed in this FEA was based on slow, uniaxial tensile loading. Further characterization of viscoelastic properties [46] would be necessary to understand adduction tethering during dynamic eye movements such as saccades. The FEA assumed a fixed ocular rotational center, although in actuality the globe is supported by deformable connective tissue [98] and orbital fat so that there is some globe translation during rotation [99-101]. Simulated stress and strain distributions might differ were the globe to be more realistically supported by a distributed anatomical structure constraining its motion. The current FEA assumed a distributed rotational force exerted on the anterior sclera, while in actuality the balance of more focally-applied medial and lateral rectus muscle forces rotate the real eye. Therefore, addition of a complete representation of the complex orbital tissue supporting system would ultimately be valuable.

References

1. Quigley HA. Number of people with glaucoma worldwide. *Br J Ophthalmol* 1996;80:389-393.
2. Nakazawa T, Fukuchi T. What is glaucomatous optic neuropathy? *Jpn J Ophthalmol* 2020;64:243-249.
3. Shiose Y, Kitazawa Y, Tsukahara S, et al. Epidemiology of glaucoma in japan--a nationwide glaucoma survey. *Jpn J Ophthalmol* 1991;35:133-155.
4. Iwase A, Suzuki Y, Araie M, et al. The prevalence of primary open-angle glaucoma in japanese: The tajimi study. *Ophthalmology* 2004;111:1641-1648.
5. Kim JH, Kang SY, Kim NR, et al. Prevalence and characteristics of glaucoma among korean adults. *Korean J Ophthalmol* 2011;25:110-115.
6. Kim CS, Seong GJ, Lee NH, Song KC, Namil Study Group KGS. Prevalence of primary open-angle glaucoma in central south korea the namil study. *Ophthalmology* 2011;118:1024-1030.
7. Cho HK, Kee C. Population-based glaucoma prevalence studies in asians. *Surv Ophthalmol* 2014;59:434-447.
8. Demer JL. Optic nerve sheath as a novel mechanical load on the globe in ocular duction. *Invest Ophthalmol Vis Sci* 2016;57:1826-1838.
9. Demer JL, Clark RA, Suh SY, et al. Magnetic resonance imaging of optic nerve traction during adduction in primary open-angle glaucoma with normal intraocular pressure. *Invest Ophthalmol Vis Sci* 2017;58:4114-4125.
10. Suh SY, Le A, Shin A, Park J, Demer JL. Progressive deformation of the optic nerve head and peripapillary structures by graded horizontal duction. *Invest Ophthalmol Vis Sci* 2017;58:5015-5021.
11. Clark RA, Suh SY, Caprioli J, et al. Adduction-induced strain on the optic nerve in primary open-angle glaucoma at normal intraocular pressure. *Curr Eye Res* 2020;1-11.
12. Kim JS, Kim YK, Kim YW, et al. Association between esodeviation and primary open-angle glaucoma: The 2010-2011 korea national health and nutrition examination survey. *Br J Ophthalmol* 2020.

13. Shin A, Yoo L, Park J, Demer JL. Finite element biomechanics of optic nerve sheath traction in adduction. *J Biomech Eng* 2017;139.
14. Wang X, Rumpel H, Lim WE, et al. Finite element analysis predicts large optic nerve head strains during horizontal eye movements. *Invest Ophthalmol Vis Sci* 2016;57:2452-2462.
15. Wang X, Fisher LK, Milea D, Jonas JB, Girard MJ. Predictions of optic nerve traction forces and peripapillary tissue stresses following horizontal eye movements. *Invest Ophthalmol Vis Sci* 2017;58:2044-2053.
16. Park J, Shin A, Jafari S, Demer JL. Material properties and effect of preconditioning of human sclera, optic nerve, and optic nerve sheath. *Biomech Model Mechanobiol* 2021.
17. Cook DD, Robertson DJ. The generic modeling fallacy: Average biomechanical models often produce non-average results! *J Biomech* 2016;49:3609-3615.
18. Bekerman I, Gottlieb P, Vaiman M. Variations in eyeball diameters of the healthy adults. *J Ophthalmol* 2014;2014:503645.
19. Olsen TW, Aaberg SY, Geroski DH, Edelhauser HF. Human sclera: Thickness and surface area. *Am J Ophthalmol* 1998;125:237-241.
20. Vurgese S, Panda-Jonas S, Jonas JB. Scleral thickness in human eyes. *PLoS One* 2012;7:e29692.
21. Boote C, Sigal IA, Grytz R, Hua Y, Nguyen TD, Girard MJA. Scleral structure and biomechanics. *Prog Retin Eye Res* 2020;74:100773.
22. Fazio MA, Grytz R, Morris JS, et al. Age-related changes in human peripapillary scleral strain. *Biomech Model Mechanobiol* 2014;13:551-563.
23. Basmak H, Sahin A, Yildirim N, Papakostas TD, Kanellopoulos AJ. Measurement of angle kappa with synoptophore and orbscan ii in a normal population. *J Refract Surg* 2007;23:456-460.
24. Jonas JB, Berenshtein E, Holbach L. Lamina cribrosa thickness and spatial relationships between intraocular space and cerebrospinal fluid space in highly myopic eyes. *Invest Ophthalmol Vis Sci* 2004;45:2660-2665.
25. Sigal IA, Flanagan JG, Ethier CR. Factors influencing optic nerve head biomechanics. *Invest Ophthalmol Vis Sci* 2005;46:4189-4199.

26. Karim S, Clark RA, Poukens V, Demer JL. Demonstration of systematic variation in human intraorbital optic nerve size by quantitative magnetic resonance imaging and histology. *Invest Ophthalmol Vis Sci* 2004;45:1047-1051.
27. Miller K. Constitutive model of brain tissue suitable for finite element analysis of surgical procedures. *J Biomech* 1999;32:531-537.
28. Beer FP, Johnston ER, DeWolf JT, Mazurek DF. *Mechanics of materials*. 7 ed. 2 Penn Plaza, New York, NY 10121: McGraw-Hill Education; 2011.
29. Killer HE, Laeng HR, Flammer J, Groscurth P. Architecture of arachnoid trabeculae, pillars, and septa in the subarachnoid space of the human optic nerve: Anatomy and clinical considerations. *Br J Ophthalmol* 2003;87:777-781.
30. Liu B, McNally S, Kilpatrick JI, Jarvis SP, O'Brien CJ. Aging and ocular tissue stiffness in glaucoma. *Surv Ophthalmol* 2018;63:56-74.
31. Jonas JB, Wang YX, Dong L, Guo Y, Panda-Jonas S. Advances in myopia research anatomical findings in highly myopic eyes. *Eye Vis (Lond)* 2020;7:45.
32. Ohno-Matsui K, Jonas JB. Posterior staphyloma in pathologic myopia. *Prog Retin Eye Res* 2019;70:99-109.
33. Sigal IA, Ethier CR. Biomechanics of the optic nerve head. *Exp Eye Res* 2009;88:799-807.
34. Siaudvytyte L, Januleviciene I, Ragauskas A, Bartusis L, Siesky B, Harris A. Update in intracranial pressure evaluation methods and translaminar pressure gradient role in glaucoma. *Acta Ophthalmol* 2015;93:9-15.
35. Wang YX, Jiang R, Wang NL, Xu L, Jonas JB. Acute peripapillary retinal pigment epithelium changes associated with acute intraocular pressure elevation. *Ophthalmology* 2015;122:2022-2028.
36. Wang Y, Xu L, Zhang L, Yang H, Ma Y, Jonas JB. Peripapillary atrophy in elderly chinese in rural and urban beijing. *Eye (Lond)* 2008;22:261-266.
37. Jonas JB, Fernandez MC, Naumann GO. Glaucomatous parapapillary atrophy. Occurrence and correlations. *Arch Ophthalmol* 1992;110:214-222.
38. Sugiyama K, Tomita G, Kitazawa Y, Onda E, Shinohara H, Park KH. The associations of optic disc hemorrhage with retinal nerve fiber layer defect and peripapillary atrophy in normal-tension glaucoma. *Ophthalmology* 1997;104:1926-1933.

39. Uchida H, Ugurlu S, Caprioli J. Increasing peripapillary atrophy is associated with progressive glaucoma. *Ophthalmology* 1998;105:1541-1545.
40. Manjunath V, Shah H, Fujimoto JG, Duker JS. Analysis of peripapillary atrophy using spectral domain optical coherence tomography. *Ophthalmology* 2011;118:531-536.
41. Park KH, Tomita G, Liou SY, Kitazawa Y. Correlation between peripapillary atrophy and optic nerve damage in normal-tension glaucoma. *Ophthalmology* 1996;103:1899-1906.
42. Burgoyne CF, Downs JC, Bellezza AJ, Suh JK, Hart RT. The optic nerve head as a biomechanical structure: A new paradigm for understanding the role of iop-related stress and strain in the pathophysiology of glaucomatous optic nerve head damage. *Prog Retin Eye Res* 2005;24:39-73.
43. Wright RM, Ramesh KT. An axonal strain injury criterion for traumatic brain injury. *Biomech Model Mechanobiol* 2012;11:245-260.
44. Cambre I, Gaublomme D, Burssens A, et al. Mechanical strain determines the site-specific localization of inflammation and tissue damage in arthritis. *Nat Commun* 2018;9:4613.
45. Le A, Chen J, Lesgart M, Gawargious BA, Suh SY, Demer JL. Age-dependent deformation of the optic nerve head and peripapillary retina by horizontal duction. *Am J Ophthalmol* 2020;209:107-116.
46. Downs JC, Suh JK, Thomas KA, Bellezza AJ, Hart RT, Burgoyne CF. Viscoelastic material properties of the peripapillary sclera in normal and early-glaucoma monkey eyes. *Invest Ophthalmol Vis Sci* 2005;46:540-546.
47. Linden C, Qvarlander S, Johannesson G, et al. Normal-tension glaucoma has normal intracranial pressure: A prospective study of intracranial pressure and intraocular pressure in different body positions. *Ophthalmology* 2018;125:361-368.
48. Fortune B. Pulling and tugging on the retina: Mechanical impact of glaucoma beyond the optic nerve head. *Invest Ophthalmol Vis Sci* 2019;60:26-35.
49. Norman RE, Flanagan JG, Sigal IA, Rausch SM, Tertinegg I, Ethier CR. Finite element modeling of the human sclera: Influence on optic nerve head biomechanics and connections with glaucoma. *Exp Eye Res* 2011;93:4-12.
50. Quigley HA. Use of animal models and techniques in glaucoma research: Introduction. *Methods Mol Biol* 2018;1695:1-10.

51. Fazio MA, Grytz R, Morris JS, Bruno L, Girkin CA, Downs JC. Human scleral structural stiffness increases more rapidly with age in donors of african descent compared to donors of european descent. *Invest Ophthalmol Vis Sci* 2014;55:7189-7198.
52. Curtin BJ. Physiopathologic aspects of scleral stress-strain. *Trans Am Ophthalmol Soc* 1969;67:417-461.
53. Gogola A, Jan NJ, Brazile B, et al. Spatial patterns and age-related changes of the collagen crimp in the human cornea and sclera. *Invest Ophthalmol Vis Sci* 2018;59:2987-2998.
54. Albon J, Purslow PP, Karwatowski WS, Easty DL. Age related compliance of the lamina cribrosa in human eyes. *Br J Ophthalmol* 2000;84:318-323.
55. Sibony PA, Wei J, Sigal IA. Gaze-evoked deformations in optic nerve head drusen: Repetitive shearing as a potential factor in the visual and vascular complications. *Ophthalmology* 2018;125:929-937.
56. Shinohara K, Shimada N, Moriyama M, et al. Posterior staphylomas in pathologic myopia imaged by widefield optical coherence tomography. *Invest Ophthalmol Vis Sci* 2017;58:3750-3758.
57. Markov PP, Eliasy A, Pijanka JK, et al. Bulk changes in posterior scleral collagen microstructure in human high myopia. *Mol Vis* 2018;24:818-833.
58. Samarawickrama C, Mitchell P, Tong L, et al. Myopia-related optic disc and retinal changes in adolescent children from singapore. *Ophthalmology* 2011;118:2050-2057.
59. Lee KM, Choung HK, Kim M, Oh S, Kim SH. Positional change of optic nerve head vasculature during axial elongation as evidence of lamina cribrosa shifting: Boramae myopia cohort study report 2. *Ophthalmology* 2018;125:1224-1233.
60. Kim M, Choung HK, Lee KM, Oh S, Kim SH. Longitudinal changes of optic nerve head and peripapillary structure during childhood myopia progression on oct: Boramae myopia cohort study report 1. *Ophthalmology* 2018;125:1215-1223.
61. Jeoung JW, Yang H, Gardiner S, et al. Optical coherence tomography optic nerve head morphology in myopia i: Implications of anterior scleral canal opening versus bruch membrane opening offset. *Am J Ophthalmol* 2020;218:105-119.
62. Sigal IA, Flanagan JG, Tertinegg I, Ethier CR. Finite element modeling of optic nerve head biomechanics. *Invest Ophthalmol Vis Sci* 2004;45:4378-4387.

63. Zhang L, Albon J, Jones H, et al. Collagen microstructural factors influencing optic nerve head biomechanics. *Invest Ophthalmol Vis Sci* 2015;56:2031-2042.
64. Sigal IA, Flanagan JG, Tertinegg I, Ethier CR. Modeling individual-specific human optic nerve head biomechanics. Part i: Iop-induced deformations and influence of geometry. *Biomech Model Mechanobiol* 2009;8:85-98.
65. Sigal IA, Flanagan JG, Tertinegg I, Ethier CR. Modeling individual-specific human optic nerve head biomechanics. Part ii: Influence of material properties. *Biomech Model Mechanobiol* 2009;8:99-109.
66. Strouthidis NG, Fortune B, Yang H, Sigal IA, Burgoyne CF. Effect of acute intraocular pressure elevation on the monkey optic nerve head as detected by spectral domain optical coherence tomography. *Invest Ophthalmol Vis Sci* 2011;52:9431-9437.
67. Shi D, Funayama T, Mashima Y, et al. Association of hk2 and nck2 with normal tension glaucoma in the japanese population. *PLoS One* 2013;8:e54115.
68. Ha A, Kim YK, Jeoung JW, Kim DM, Park KH. Association of angle width with progression of normal-tension glaucoma: A minimum 7-year follow-up study. *JAMA Ophthalmol* 2019;137:13-20.
69. Zhao J, Solano MM, Oldenburg CE, et al. Prevalence of normal-tension glaucoma in the chinese population: A systematic review and meta-analysis. *Am J Ophthalmol* 2019;199:101-110.
70. Kim JA, Kim TW, Lee EJ, Girard MJA, Mari JM. Lamina cribrosa morphology in glaucomatous eyes with hemifield defect in a korean population. *Ophthalmology* 2019;126:692-701.
71. Killer HE, Pircher A. Normal tension glaucoma: Review of current understanding and mechanisms of the pathogenesis. *Eye (Lond)* 2018;32:924-930.
72. Sommer A, Tielsch JM, Katz J, et al. Racial differences in the cause-specific prevalence of blindness in east baltimore. *N Engl J Med* 1991;325:1412-1417.
73. Bonomi L, Marchini G, Marraffa M, et al. Prevalence of glaucoma and intraocular pressure distribution in a defined population. The egna-neumarkt study. *Ophthalmology* 1998;105:209-215.
74. Klein BE, Klein R, Sponsel WE, et al. Prevalence of glaucoma. The beaver dam eye study. *Ophthalmology* 1992;99:1499-1504.

75. Rotchford AP, Johnson GJ. Glaucoma in zulus: A population-based cross-sectional survey in a rural district in south africa. *Arch Ophthalmol* 2002;120:471-478.
76. Iwase A, Araie M, Tomidokoro A, et al. Prevalence and causes of low vision and blindness in a japanese adult population: The tajimi study. *Ophthalmology* 2006;113:1354-1362.
77. Shin JW, Sung KR, Song MK. Ganglion cell-inner plexiform layer and retinal nerve fiber layer changes in glaucoma suspects enable prediction of glaucoma development. *Am J Ophthalmol* 2020;210:26-34.
78. Han JC, Han SH, Park DY, Lee EJ, Kee C. Clinical course and risk factors for visual field progression in normal-tension glaucoma with myopia without glaucoma medications. *Am J Ophthalmol* 2020;209:77-87.
79. Lee J, Kim YK, Jeoung JW, Ha A, Kim YW, Park KH. Machine learning classifiers-based prediction of normal-tension glaucoma progression in young myopic patients. *Jpn J Ophthalmol* 2020;64:68-76.
80. Gordon MO, Beiser JA, Brandt JD, et al. The ocular hypertension treatment study: Baseline factors that predict the onset of primary open-angle glaucoma. *Arch Ophthalmol* 2002;120:714-720; discussion 829-730.
81. Zhang X, Dastiridou A, Francis BA, et al. Baseline fourier-domain optical coherence tomography structural risk factors for visual field progression in the advanced imaging for glaucoma study. *Am J Ophthalmol* 2016;172:94-103.
82. Seol BR, Kim S, Kim DM, Park KH, Jeoung JW, Kim SH. Influence of intraocular pressure reduction on progression of normal-tension glaucoma with myopic tilted disc and associated risk factors. *Jpn J Ophthalmol* 2017;61:230-236.
83. Group CN-TGS. The effectiveness of intraocular pressure reduction in the treatment of normal-tension glaucoma. Collaborative normal-tension glaucoma study group. *Am J Ophthalmol* 1998;126:498-505.
84. Group CN-TGS. Comparison of glaucomatous progression between untreated patients with normal-tension glaucoma and patients with therapeutically reduced intraocular pressures. Collaborative normal-tension glaucoma study group. *Am J Ophthalmol* 1998;126:487-497.
85. Berdahl JP, Allingham RR. Intracranial pressure and glaucoma. *Curr Opin Ophthalmol* 2010;21:106-111.

86. Berdahl JP, Fautsch MP, Stinnett SS, Allingham RR. Intracranial pressure in primary open-angle glaucoma, normal tension glaucoma, and ocular hypertension: A case-control study. *Invest Ophthalmol Vis Sci* 2008;49:5412-5418.
87. Jonas JB, Yang D, Wang N. Intracranial pressure and glaucoma. *J Glaucoma* 2013;22 Suppl 5:S13-14.
88. Pircher A, Remonda L, Weinreb RN, Killer HE. Translaminar pressure in caucasian normal tension glaucoma patients. *Acta Ophthalmol* 2017;95:e524-e531.
89. Nguyen C, Midgett D, Kimball EC, et al. Measuring deformation in the mouse optic nerve head and peripapillary sclera. *Invest Ophthalmol Vis Sci* 2017;58:721-733.
90. Voorhees AP, Jan NJ, Austin ME, et al. Lamina cribrosa pore shape and size as predictors of neural tissue mechanical insult. *Invest Ophthalmol Vis Sci* 2017;58:5336-5346.
91. Leclair-Visonneau L, Oudiette D, Gaymard B, Leu-Semenescu S, Arnulf I. Do the eyes scan dream images during rapid eye movement sleep? Evidence from the rapid eye movement sleep behaviour disorder model. *Brain* 2010;133:1737-1746.
92. Guitton D, Volle M. Gaze control in humans: Eye-head coordination during orienting movements to targets within and beyond the oculomotor range. *J Neurophysiol* 1987;58:427-459.
93. Wu CC, Kowler E. Timing of saccadic eye movements during visual search for multiple targets. *J Vis* 2013;13.
94. Robinson DA. Control of eye movements. In: Terjung R (ed), *Comprehensive physiology*: Wiley Online Library; 2011:1275-1320.
95. Anastasopoulos D, Ziavra N, Hollands M, Bronstein A. Gaze displacement and inter-segmental coordination during large whole body voluntary rotations. *Exp Brain Res* 2009;193:323-336.
96. Anastasopoulos D, Naushahi J, Sklavos S, Bronstein AM. Fast gaze reorientations by combined movements of the eye, head, trunk and lower extremities. *Exp Brain Res* 2015;233:1639-1650.
97. Kothari R, Yang Z, Kanan C, Bailey R, Pelz JB, Diaz GJ. Gaze-in-wild: A dataset for studying eye and head coordination in everyday activities. *Sci Rep* 2020;10:2539.
98. Kakizaki H, Takahashi Y, Nakano T, et al. Anatomy of tenons capsule. *Clin Exp Ophthalmol* 2012;40:611-616.

99. Demer JL. Mechanics of the orbita. *Dev Ophthalmol* 2007;40:13 2-157.
100. Miller JM, Demer JL, Poukens V, Pavlovski DS, Nguyen HN, Rossi EA. Extraocular connective tissue architecture. *J Vis* 2003;3:240-251.
101. Demer JL, Miller JM, Poukens V, Vinters HV, Glasgow BJ. Evidence for fibromuscular pulleys of the recti extraocular muscles. *Invest Ophthalmol Vis Sci* 1995;36:1125-1136.

4.6. Cumulative Optic Nerve Head Deformations

Through FEA study, we quantitatively predicted the stress and strain occurring in the ON head due to the ON traction during ocular adduction. The healthy average case shown in the FEA study predicted 141kPa stress and 4% strain, while the most extreme case predicted 291 kPa stress and 6% strain on the temporal ON head. Considering the published physiologic 1 MPa stress and 18% strain threshold for ON injury[1], neither stress nor strain for even the extreme cases in the FEA study exceeded the threshold, so eye rotation does not acutely break the ON. However, it should be noted that the results obtained from this study were the result of a single quasi-static eye rotation. Due to numerous voluntary and reflexive eye rotations, cycles of cumulative deformation must occur. Furthermore, saccades that create 400 °/sec of fast eye rotation[2] might be expected to cause much greater deformation due to the viscous forces applied during rotation than the static deformation predicted in the FEA study.

Cumulative ON head deformation due to repetitive eye rotation may cause the progressive optic neuropathy but deformations at the relevant level do not break the tissue as in metal fatigue failure. When a biological tissue is subjected to a mechanical load, cellular deformations typically occur that trigger intracellular mechanotransduction pathways[3]. Although the driving pathology of mechanical load-induced cellular deformation has not yet been clearly elucidated, it is known that the response of biological cells to load results in growth, differentiation, adaptation, or cell

destruction[3]. When repeated ON traction is applied during adduction, the connective tissue surrounding the neural tissue may gradually stiffen by crosslinking of the collagen[4, 5], which is an adaptation to the mechanical stimulus[6]. However, this type of adaptation may make the ON even more vulnerable to traction in the subsequent eye rotation cycles.

4.7. Pathological Explanations Associated with Normal Tension Glaucoma

The imaging and FEA studies of ON tethering during eye rotation confirmed that deformation of the optic disc was greater in adduction than in abduction, and in temporal than nasal parts of the optic disc for healthy and glaucomatous people. The studies showed the occurrence of ON tethering in various approaches but did not explain why ON head deformation may lead to the NTG. The location of the largest deformation during adduction in these studies closely matched the location of peripapillary atrophy of the retinal pigment epithelium and choroid. Sibony *et a*l. have suggested that ocular motor force may cause peripapillary subretinal hemorrhage[7]. The peripapillary atrophy is associated with chorioretinal thinning and disruption of retinal pigment epithelium in the area surrounding the optic disc but the cause of the disease is still unknown. Based on the evidence described above, the ON tethering hypothesis in adduction may explain the cause of peripapillary atrophy. The following explanation that links to NTG is a group of patients prone to peripapillary atrophy. Previous literature has shown that peripapillary atrophy tends to be frequent in the NTG[8-10] and high myopia[11]. Furthermore, Demer *et al.* demonstrated through an MRI study that, due to ON tethering in adduction, NTG patients exhibited abnormally large globe retraction while the healthy normal group had no significant globe retraction[12]. Clark *et al.* measured the path length of the ON using quasi-coronal MRI images, showing that patients

with POAG had little or no ON elongation in adduction which induces larger globe posterior retraction than the normal group in whom the ON stretched significantly[13].

There is one cautionary consideration about development of the ON tethering hypothesis of NTG. ON tethering happens to everyone, but just because this occurs does not mean everyone gets NTG. This hypothesis is based on the properties and mechanical environment of the ON. If the ON is sufficiently long, tethering itself will not occur during either adduction or abduction, and the deformation in the ON head caused by eye rotation will be very small. Also, even though the ON length is insufficient and tethering occurs, if the material properties of the ocular tissues are sufficiently compliant, the energy generated by ON tethering can be absorbed throughout the sclera and along the length of the ON without being concentrated at the ON head. Finally, ON damage may not occur if the tissue damage threshold or response to external stimuli is very high.

4.8. High intraocular Pressure vs. Optic Nerve Tethering

Previous glaucoma studies have suggested that high IOP and low intracranial pressure (ICP) greatly deforms the ON head, likely resulting in glaucomatous ON damage[14-16]. Depending on the studies, test setups of high IOP varied but most studies employed IOP within the range of 30 to 50 mmHg[14, 17, 18]. As of verification of the model, our FEA study also included simulation with high IOP (40 mmHg) comparable to other publications. Establishing validity, our study predicted a similar amount of deformation around the ON head as did the other studies that simulated high IOP. We also demonstrate that the effect of ON tethering during 32º adduction, which occurred mostly on the temporal side of the ON head at 141 kPa, was much greater than that of extreme hydrostatic pressure which resulted in relatively smaller ring shape deformations at 25 kPa around

the optic disc. Many high IOP-related literatures suggest that deformation due to extreme hydrostatic pressure that applies inside the globe affects the health of ON. Since the amount of deformation shown by ON tethering FEM is much larger than that in the case of extreme static pressure, it plausibly may have a significant role in causing optic neuropathy.

References

1. Bain AC, Meaney DF. Tissue-level thresholds for axonal damage in an experimental model of central nervous system white matter injury. *J Biomech Eng* 2000;122:615-22.
2. Raab EL. Normal saccadic velocities. *J Pediatr Ophthalmol Strabismus* 1985;22:20-2.
3. Bader DL, Knight MM. Biomechanical analysis of structural deformation in living cells. *Med Biol Eng Comput* 2008;46:951-63.
4. Solan A, Dahl SL, Niklason LE. Effects of mechanical stretch on collagen and cross-linking in engineered blood vessels. *Cell Transplant* 2009;18:915-21.
5. Sarrigiannidis SO, Rey JM, Dobre O, Gonzalez-Garcia C, Dalby MJ, Salmeron-Sanchez M. A tough act to follow: Collagen hydrogel modifications to improve mechanical and growth factor loading capabilities. *Mater Today Bio* 2021;10:100098.
6. Icard-Arcizet D, Cardoso O, Richert A, Henon S. Cell stiffening in response to external stress is correlated to actin recruitment. *Biophys J* 2008;94:2906-13.
7. Sibony P, Fourman S, Honkanen R, El Baba F. Asymptomatic peripapillary subretinal hemorrhage: A study of 10 cases. *J Neuroophthalmol* 2008;28:114-9.
8. Jonas JB, Martus P, Horn FK, Junemann A, Korth M, Budde WM. Predictive factors of the optic nerve head for development or progression of glaucomatous visual field loss. *Invest Ophthalmol Vis Sci* 2004;45:2613-8.
9. Xu L, Wang Y, Yang H, Jonas JB. Differences in parapapillary atrophy between glaucomatous and normal eyes: The beijing eye study. *Am J Ophthalmol* 2007;144:541-6.

10. Jonas JB, Nguyen XN, Gusek GC, Naumann GO. Parapapillary chorioretinal atrophy in normal and glaucoma eyes. I. Morphometric data. *Invest Ophthalmol Vis Sci* 1989;30:908-18.
11. Nakazawa M, Kurotaki J, Ruike H. Longterm findings in peripapillary crescent formation in eyes with mild or moderate myopia. *Acta Ophthalmol* 2008;86:626-9.
12. Demer JL, Clark RA, Suh SY, et al. Magnetic resonance imaging of optic nerve traction during adduction in primary open-angle glaucoma with normal intraocular pressure. *Invest Ophthalmol Vis Sci* 2017;58:4114-25.
13. Clark RA, Suh SY, Caprioli J, et al. Adduction-induced strain on the optic nerve in primary open angle glaucoma at normal intraocular pressure. *Curr Eye Res* 2021;46:568-78.
14. Coudrillier B, Tian J, Alexander S, Myers KM, Quigley HA, Nguyen TD. Biomechanics of the human posterior sclera: Age- and glaucoma-related changes measured using inflation testing. *Invest Ophthalmol Vis Sci* 2012;53:1714-28.
15. Quigley HA. Neuronal death in glaucoma. *Prog Retin Eye Res* 1999;18:39-57.
16. Morrison JC, Johnson EC, Cepurna W, Jia L. Understanding mechanisms of pressure-induced optic nerve damage. *Prog Retin Eye Res* 2005;24:217-40.
17. Norman RE, Flanagan JG, Sigal IA, Rausch SM, Tertinegg I, Ethier CR. Finite element modeling of the human sclera: Influence on optic nerve head biomechanics and connections with glaucoma. *Exp Eye Res* 2011;93:4-12.
18. Sigal IA, Flanagan JG, Tertinegg I, Ethier CR. Finite element modeling of optic nerve head biomechanics. *Invest Ophthalmol Vis Sci* 2004;45:4378-87.

CHAPTER 5. CONCLUSIONS

5.1. Conclusions

The thesis explored anatomical and mechanical characteristics of human ocular tissues determining biomechanical behaviors of the human eye, in the context of a hypothesis of ON tethering in adduction. The novel hyperelastic property of human ON and bilayer structure of the human ON sheath were discovered using uniaxial tensile loading. Furthermore, deformation of the ON head caused by ON traction was observed using imaging techniques such as OCT and SLO. Beyond imaging observations, FEM incorporating our characterization of tensile properties of ocular tissue suggested a possible mechanism of tethering that might damage the ON and peripapillary retina. This thesis concludes that frequently-occurring ocular adduction deforms the optic disc and peripapillary retina due to shortness of the ON, and proposes that numerous cycles of this mechanical loading may cause optic neuropathy in NTG.

5.2. Possible Treatments

If the hypothesis of the pathogenic nature of ON tethering during adduction is confirmed, research on possible treatments would be possible. To minimize the effect of ON tethering during eye rotation, it might be therapeutic to reduce volume in the posterior orbit behind the eye in the tissues that surround the ON. When a surgeon reduces the amount of orbital fat, the entire globe translates posteriorly so that the required ON path length from the apex to the eyeball is shortened, mitigating tethering by simple geometry. Orbital fat decompression surgery is standard practice

for some indications such as thyroid ophthalmopathy[1], although not currently performed for NTG. Another possible treatment might be to perform surgery on the extraocular muscles to weaken active tension in adduction and thus reduce the force of adduction tethering. Yet another treatment might be chemical tissue crosslinking to locally alter the mechanical behavior of the scleral and ON sheath. Gawargious *et al*. have investigated the regional stiffening effect of scleral tissue by collagen crosslinking using ultraviolet activation of riboflavin that increased stiffness in all scleral regions[2]. As discussed in the FEA study, the deformation around the ON head due to tethering can vary depending on the combinations of material properties of nearby ocular tissue. Based on this fact, selective riboflavin perfusion with local UV activation to induce local scleral or ON sheath stiffening might favorably shift stresses and strains to reduce deformation of the ON head during adduction tethering.

5.3. Current Status of Hypothesis

Since Demer first proposed the ON tethering hypothesis in 2016, many observational studies, experiments, and simulations using various equipment have been conducted. However, this novel hypothesis remains particularly controversial due to profound historical emphasis on the role of IOP in the pathogenesis, and certainly the medical and surgical treatment, of glaucoma. This includes a commitment to IOP reduction by nearly all ophthalmic practitioners, as well as large university and industrial research operations, pharmaceutical and medical device producers, and high-volume surgical practices, as well as the army of patients who understandably fear blindness and have been educated only about the role of IOP in glaucoma. Most other biomechanics laboratories studying glaucoma investigate only the effects of IOP. While clinical

glaucoma specialists now admit that IOP is not the cause of primary open-angle glaucoma, their vigorous insistence that IOP reduction is the only known treatment for this disease appears to discourage consideration of alternative hypotheses about the actual cause of NTG. Of course, the two concepts are not mutually exclusive: while repetitive cycles of repetitive stress to the ON during eye movements might be the major cause of NTG, IOP could have a supplemental role, as suggested by the FEM performed here.

Consider the field of astronomy when Galileo proposed the heliocentric theory of the solar system, only to be ridiculed and suppressed. Even if the ON adduction tethering hypothesis is ultimately shown to be incorrect, we seek to have it objectively considered. Philosopher of science Thomas S. Kuhn, the author of "The Structure of Scientific Revolutions", wisely wrote that "Normal science often suppresses fundamental novelties because they are necessarily subversive of its basic commitments." (p5) He further wrote, "When the profession can no longer evade anomalies that subvert the existing tradition of scientific practice – then begin the extraordinary investigations that lead the profession at last to a new set of commitments, a new basis for the practice of science." (p6)[3] Fortunately, many clinical studies in East Asia supporting the ON tethering hypothesis are emerging[4-8]. It seems likely that the hypothesis of ON makes at least some contribution to NTG. Through this hypothesis, I hope that "the profession" soon starts accepting and replicating experiments in "the extraordinary investigation" that finds the cause of diseases such as NTG.

References

1. Ramesh S, Nobori A, Wang Y, Rootman D, Goldberg RA. Orbital expansion in cranial vault after minimally invasive extradural transorbital decompression for thyroid orbitopathy. *Ophthalmic Plast Reconstr Surg* 2019;35:17-21.
2. Gawargious BA, Le A, Lesgart M, Ugradar S, Demer JL. Differential regional stiffening of sclera by collagen cross-linking. *Curr Eye Res* 2020;45:718-25.
3. Kuhn TS. *The structure of scientific revolutions*. Second ed. Chicago: The university of chicago; 1962.
4. Kim M, Choung HK, Lee KM, Oh S, Kim SH. Longitudinal changes of optic nerve head and peripapillary structure during childhood myopia progression on oct: Boramae myopia cohort study report 1. *Ophthalmology* 2018;125:1215-23.
5. Lee KM, Choung HK, Kim M, Oh S, Kim SH. Positional change of optic nerve head vasculature during axial elongation as evidence of lamina cribrosa shifting: Boramae myopia cohort study report 2. *Ophthalmology* 2018;125:1224-33.
6. Wang X, Fisher LK, Milea D, Jonas JB, Girard MJ. Predictions of optic nerve traction forces and peripapillary tissue stresses following horizontal eye movements. *Invest Ophthalmol Vis Sci* 2017;58:2044-53.
7. Wang X, Rumpel H, Lim WE, et al. Finite element analysis predicts large optic nerve head strains during horizontal eye movements. *Invest Ophthalmol Vis Sci* 2016;57:2452-62.
8. Park HY, Lee K, Park CK. Optic disc torsion direction predicts the location of glaucomatous damage in normal-tension glaucoma patients with myopia. *Ophthalmology* 2012;119:1844-51.